A 3D view of environmental quenching across cosmic time

Nicholas James Amos

Physics

Department of Physics

Lancaster University

January 2024

A thesis submitted to Lancaster University for the degree of

Doctor of Philosophy in the Faculty of Science and Technology

Supervised by Dr John P. Stott

Abstract

The study of galaxy evolution is crucial to our understanding of the Universe. It determines how galaxies got from where they started and what their likely end will be. Also crucial is our understanding of how galaxies in denser environments evolve compared to those that are more isolated. A large proportion of the galaxies in the Universe are found in galaxy clusters and so they form a significant population. Significantly, we see at the so called cosmic noon that these galaxies begin to change from largely star-forming to more quiescent systems. This is true both in the field and cluster environment but the significance of the latter on quenching must be understood.

In this thesis we investigate star-forming galaxies in clusters at cosmic noon using spatially resolved spectroscopy of the gas content in these galaxies alongside near-infrared photometry. Using these complimentary data we demonstrate that while the cluster environment does not appear to impact these galaxies significantly in some ways compared to their field counterparts, it may be changing their morphology, which in turn may impact their star-formation-rate. We also find that the metallicities of these cluster galaxies deviate from relationships derived from samples of field galaxies, which may indicate the environmental impact of gas exchange between the galaxies and their host cluster but more data is needed to determine if these conclusions are statistically significant.

Finally, we report on the serendipitous discovery of a likely Brightest Cluster Galaxy caught in the act of formation. Analysis of the kinematics of two of the four potential merger components indicates that these are likely to merge. Alongside this assessing various combinations of the final

galaxy stellar masses using these four components demonstrate the final BCG would be well within the mass ranges expected for a BCG at $z \sim 1.4$.

This thesis is dedicated to my family, both chosen and born to.

Acknowledgements

I would like to begin this thesis by thanking my stalwart supervisor, Dr John P. Stott, who has always encouraged my tangents along this journey and never been one to deny an opportunity. Taking this journey would not have been possible without his guidance and knowledge. I would also like to thank the entire Observational Astrophysics group at Lancaster University for being a welcoming and encouraging place to newcomers, I cannot imagine carrying out my PhD anywhere else.

My family have always been there for me whenever I have needed them and this has been no exception, from my initial terrifying decision to study for my BSc, I think we have all learnt things along the way. As for my fiancée Emily, there aren't enough words to express my thanks. From that first night moving together to Lancaster, through the late nights, and periods of absence you have always been there to support me along the way and I will never forget that as we embark on the next exciting stage of our lives together.

The time I spent working with the technicians and researchers at the ING and my fellow SAs at the INT were amongst the most exciting of my academic life. They showed me astrophysics beyond my research and really taught me the value of quality observations, alongside a healthy dose of patience. In particular I would like to thank Ovidiu for providing me the opportunity and particularly Cecilia for her rock solid support and dedication to her role. I would like to specifically thank my fellow SAs for being so inclusive and always being there to talk; Tom, Jake, Vikki, Macarena, and of course Rebeca whom I hope has found peace.

Thank you to my friends who have always provided a healthy distraction when needed. Particularly; Matthew, Ryan and Alex for a combination of parties, computer gaming sessions, and cricket when I need bringing back down to Earth. Also thanks to the Archers of Dolphinholme who also provided a welcome escape from my academic work.

Lastly, I would like to thank Lancaster University for the opportunity to carry out this work and also providing the funding and equipment needed to complete this PhD and pursue my interests.

Declaration

Section 2.5 of this thesis was performed and written by my supervisor Dr John Stott. The remainder is my own work and no portion of the work referred to in this thesis has been submitted in support of an application for another degree or qualification at this or any other institute of learning.

“As much as we need a prosperous economy, we also need a prosperity of kindness and decency.”

–Caroline Herschel

Contents

List of Figures

List of Tables

Relevant Publications by the Author

- "The kinematics of cluster galaxies at $z \sim 1.4$"; **Amos, N. J.**; Stott, J. P.; **in prep**
- "The metal-content of cluster galaxies at $z \sim 1.4$"; **Amos, N. J.**; Stott, J. P.; **in prep**

Chapter 1

Introduction

The Universe is a collection of groups. Gas groups together to form nebulae, if clumps of gas are in the right conditions they will collapse to form stars, stars group together to form globular clusters and galaxies, galaxies group together to form groups and clusters of galaxies. These galaxy clusters are the largest gravitationally bound structures in the Universe but even these group and structure themselves into what we call the cosmic web. Understanding how these phenomena interact with each other in these groupings is therefore essential to our understanding of the Universe. In particular the evolution of galaxies with formed of gas, stars and dark matter give us an insight into how our Universe has developed in the past and where it might be heading in the future. In modern astronomy we can learn much about these components by using methods ranging from pure theoretical proof to direct observation and even complex computational simulation.

1.1 A brief history of observation

Observational astronomy has been referred to as the oldest of the sciences in both study and utility. In its most basic forms observations have informed our concept of time throughout a day and across the period of a year. This has been essential to humanity from prehistory to present as it enables us to reliably produce food and know when the seasons will change and therefore any associated weather with those seasons.

There has also been an impact on the cultural development of many civilisations of humans from ritualism of daily routine to more modern religious beliefs. In a scientific context observational astronomy has been used since the time of the Babylonians in order to understand our place in the Universe. These investigations continued through to Aristotle, Hipparchus and Ptolomney until a major step change in astronomical investigation occurred via the invention of the telescope during the 17th and 18th centuries. Subsequent refinements and grinding of finer and more uniform lenses made the telescope the tool of choice and although the telescope theory is largely attributed to Kepler (Kepler, Galilei & Pena 1611), the actual inventor of the telescope remains largely unknown.

It was around this time that Saturn became a focus of intense study between Cassini, Galileo, Huygens and others. Major discoveries about our solar system and beyond, including observations of four moons of Jupiter and confirming that the Milky Way is comprised of many individual stars. Kepler made observations of the motions of the planets and made a major contribution to a paradigm change from circular to elliptical orbits of the planets in his 'Laws of orbital motion'. While Isaac Newton was not first to postulate the concept of attraction between bodies, he made many key mathematical contributions to the field including those of orbital motion, vortices and of course gravitational attraction. These contributions went on to define astronomy all the way until Einstein's Theory of General Relativity (Einstein 1916).

1.2 Galaxies

Spectroscopy is an important tool in astronomy and has been in use since the early 17th century. Initially, observational spectroscopy used prisms to refract the light coming from the Sun onto a projecting surface. It was this simple experiment that led to the discovery of spectroscopic lines and chemical abundances. This initial discovery pushed observers to refine their refraction methods and ultimately led to the first diffraction grating. Following these discoveries, modern astronomy really developed from the start of the 20th century, where a similar step change occurred as with the invention of the telescope. The application of refined spectroscopy to observational astronomy and advanced industrial processes allowed us to both widen and deepen our

investigations of the Universe. Technology developed to the point where we started to understand more of the structure and investigate the history of the Universe.

The study of extra-galactic astronomy first began with catalogues of *nebulae* which were not point-like bright sources like stars but were unable to be defined further due to optical and technological limits. This cataloguing occurred as far back as the 1700s when hundreds of these *nebulae* were studied by Charles Messier (Messier 1781). Moving forwards to the 1920s some of these *nebulae* were found to contain variable stars that were already located in our own Galaxy. This discovery was made by Edwin Hubble with a new telescope on Mount Wilson making observations of what we now know as the Andromeda Galaxy (Hubble 1929). This discovery was made possible by studying the brightness peaks and troughs of variable stars, most notably Cepheids. Henrietta Swan Leavitt observed these stars in the Small and Large Magellanic Clouds that these variations were regular and that the brightest variables also had the longest periods of variation (Leavitt 1908). As these stars were all approximately the same distance away it was possible to determine the period of variation is related to the stars luminosity. There was an offset in absolute to apparent magnitudes of these stars solely due to their distance from Earth. With these standard relations, and the offset determined soon after by Ejnar Hertzsprung (Hertzsprung 1913), it became possible to determine the distances to any variable star provided the correct relation was used. With these known luminosities Hubble was able to estimate the relative distances from our Galaxy ($> 300k\,pc$) using the luminosity equation 1.1

$$F = \frac{L}{4\pi d^2}, \tag{1.1}$$

where F is flux, L is luminosity, and d is the distance to the target. More and more observations began to be made and it was found that these external *nebulae* were not structurally the same. This ultimately led to the need to classify these galaxies and the development of the 'tuning fork' diagram by Hubble, an example of which can be seen in figure 1.1. This diagram shows how galaxies can be divided into two main groups; ellipticals (E) and spirals (S). Aside from these main groups there are others that do not fit either. One of these are the S0 or Lenticular galaxies. These galaxies show a bulge but no features in the disk. The formation mechanism for these galaxies are not well defined with two main proposed pathways. One of these suggests a spiral galaxy

progenitor that fades due to gas content reduction (Gunn & Gott, J. Richard 1972; Larson, Tinsley & Caldwell 1980; Quilis, Moore & Bower 2000). The other main theory is that these galaxies form through a series of galaxy interactions or mergers (Bekki 1998; Icke 1985; Querejeta et al. 2015), unfortunately neither of these proposals is able to adequately explain the observed properties of this grouping of galaxies and perhaps parts of these theories are more likely (Zhou et al. 2023). A grouping, absent from the diagram, that does not appear to fit into these categories are denoted irregular galaxies (Irr). The number classification of the ellipticals denotes how elliptical the galaxy is deemed to be with E7 being more elliptical than E5. For the spiral group these can be further sub-divided into those with bars and without, and again classified in therms of increasing winding of spiral. As is often the case with observational astronomy this classification scheme was soon found to be insufficient as an increasing number of galaxies were found that could not be classified using the scheme. It has also since been determined that this scheme does not represent the evolution of galaxies and is purely applicable to separation of samples based on morphology. One of the galaxy types that cannot be classified within this scheme are cD galaxies. So named from the Yerkes galaxy classification scheme where 'c' denotes these galaxies are very large and the 'D' refers to the fact they are also diffuse. It has since been discovered that a large proportion of this class of galaxy reside centrally in rich galaxy clusters. More on these galaxies and brightest cluster galaxies (BCGs) in general can be found in chapter 5 where we discuss a potentially forming BCG in our sample.

More general populations of galaxies can be seen when assessing the colours and absolute magnitudes of individual galaxies within a colour magnitude diagram (CMD). These diagnostics were first developed for use in the study of stellar populations by Hertzsprung in 1908 (Hertzsprung 1908) but these were expanded on to study the integrated light of galaxies in clusters (Chester & Roberts 1964; Visvanathan & Sandage 1977). Using these diagrams we broadly see two main populations arising, namely the 'red sequence' and 'blue cloud' (Bell et al. 2004; de Vaucouleurs 1961; Visvanathan & Sandage 1977). There is a third proposed region as a transition zone between these called the 'green valley' that arose from data gathered by the Galaxy Evolution Explorer (GALEX, Martin et al. 2005) although the interpretation of this zone is a matter of open debate (Schawinski et al. 2014). An example galaxy CMD can be seen in figure 1.2 from Gavazzi et al. (2010). This separation in populations can be seen in terms of

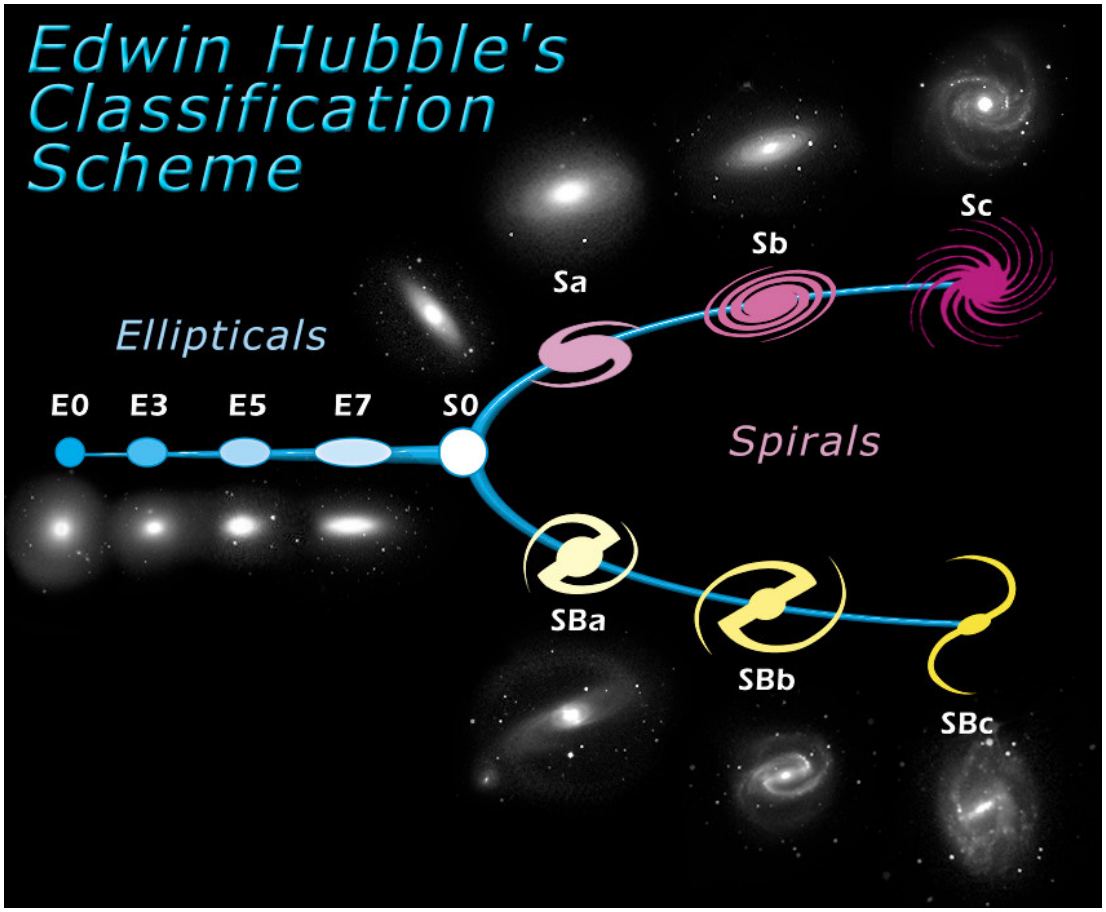

Figure 1.1: Edwin Hubble's 'Tuning Fork' classification scheme for galaxy morphology, (from ESA).

star-formation. Those red sequence are quenched with older stellar populations which tend to be more elliptical or lenticular in morphology, whereas those within the blue cloud are more star-forming and disky.

1.3 Galaxy clusters

Continuing the theme of grouping prevalent throughout this work, we arrive at galaxy clusters. These are dense collections of gravitationally bound galaxies and are amongst the most massive bound structures in the Universe. These clusters are not the only a collection of galaxies but also a collection of hot gas of comparable, but greater, mass

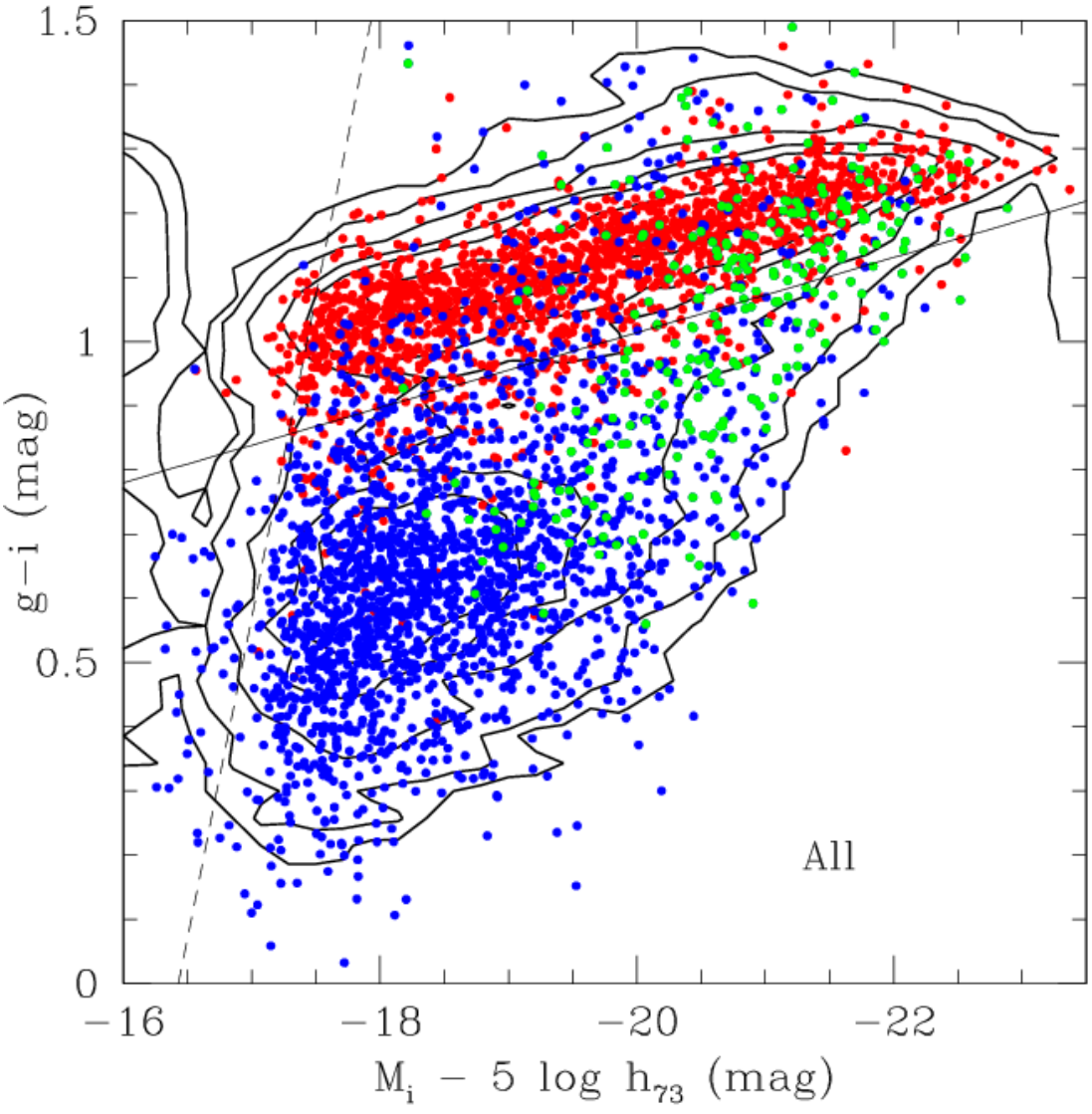

Figure 1.2: Colour magnitude diagram for galaxies within the Coma Supercluster from Gavazzi et al. (2010). Red points are galaxies designated as being early-type galaxies (Elliptical to Lenticular), the blue points indicate galaxies designated as late-type galaxies (disk galaxies), and the green points are galaxies seen as transition bulge galaxies (Sa - Sb). Contours denote lines of equal number density. The dashed black line indicates the limiting magnitude of the spectroscopic SDSS database ($r = 17.77$). The solid straight black line shows the separation of the red sequence from the rest of the population (blue cloud and green valley.

to that of the total galaxy population. These galaxy component of galaxy clusters have been shown to evolve in a hierarchical way, forming larger and larger structures (De Lucia & Blaizot 2007; Lauer et al. 2014; Stott et al. 2010).

The final dominant mass component is dark matter making up $\sim 80\%$ of the cluster mass. This mass component is considered a necessary part of galaxy clusters due to the difference in stellar mass calculations and dynamical mass estimates based on the velocities of galaxies within clusters. This work was first performed by Fritz Zwicky in 1933 (published in 1937 Zwicky 1937). In addition to this, observations of gravitational lensing (expanded on in section 1.3.1) indicate the presence of large concentrations of mass not backed up by observations across observable wavelengths.

There are primarily two general criteria used to classify a structure as a galaxy cluster. One way is to observe the structure and assess if a sufficiently large number of galaxies lie within it. Another is reaching a pre-defined density threshold such that the region can be deemed as 'overdense' compared with its surroundings and compared with a pre-defined threshold. These classifications are not defined as hard cut-off values and can be a matter of debate. These general criteria were refined by Abell into richness and compactness criteria (Abell 1958) where the rich galaxy clusters are those defined as having more than 50 galaxies that reach a magnitude limit defined by $m_3 + 2$ where m_3 is the magnitude of the third brightest member of the cluster. The compactness criteria is defined so that only galaxies within a certain radius of the cluster centre are considered to be part of the cluster.

References to clusters and groups of galaxies goes all the way back to Messier but today the most synonymous name associated with galaxy clusters is that of George Abell. During Abell's time as PhD student in $1956 - 57$ he catalogued $1{,}682$ clusters which now carry his name (Abell 1958). Similar work was also carried out by Zwicky & Humason (1961) to produce large catalogues of galaxies defined as residing within clusters. These cluster identifications have since been improved upon and expanded using more modern multi-wavelength detection techniques and dedicated wide area surveys such as the Sloan Digital Sky Survey (SDSS; York et al. 2000).

1.3.1 Cluster detection

There are a range of characteristics of galaxy clusters that enable their detection. One of these is through the large proportion of mass that is made up of gas within the cluster. This gas is heated through the transfer of gravitational potential energy in the massive gravitational potential well of a galaxy cluster to kinetic energy and thermal bremsstrahlung (slowing of the plasma and electrons in the intra-cluster medium). This plasma is extremely hot and can reach temperatures of the order 10^8K. These temperatures are enough for this medium to emit in the X-rays when cooling and so can be detected with X-ray sensitive instruments such as *Chandra* and *XMM-Newton*. This extended intra-cluster medium (ICM) can be used as an identification of a cluster and the centroid of this gas is often used as the centre of the cluster as carried out by the ROSAT deep cluster survey (Rosati et al. 1998), the XMM Cluster Survey (XCS, Mehrtens et al. 2012), and others. This gas can be used another way to identify a galaxy cluster through the use of the Sunyaev-Zeldovich (SZ; Sunyaev & Zeldovich 1972) effect. This is where the cosmic microwave background (CMB) interacts with the high energy electrons in the ICM through inverse Compton scattering. This leaves a detectable imprint of the CMB on the galaxy cluster via the energy transfer of the photons in question and has been used in surveys such as the South Pole Telescope SZ survey (SPT-SZ, Bleem et al. 2015).

In the absence of hot gas detection we must rely on the properties and number density of the galaxies within the host cluster. This can be performed relatively quickly using imaging data and identifying populations of passive 'red' galaxies in colour-magnitude diagrams which can be used to identify galaxy clusters through application of the morphology density relation (Dressler 1980) in that red elliptical galaxies are more commonly located within a cluster environment. The application of the morphology density relation is dependent on the age-metallicity degeneracy in galaxies i.e, how a galaxies disk evolves. Although similar to how those initial catalogues of Abell galaxy clusters were formed, this technique does not rely on a human eye looking at images of potential clusters. Rather it utilises catalogues of galaxies from these images and their photometric properties to fit slopes to the red-sequence. While this method is efficient and can be carried out without lengthy observations it can be prone to interlopers. This technique has been used on large unique surveys such as the Red-Sequence Cluster

Survey (RCS, Gladders & Yee 2005) but also applied to large catalogues of existing data such as with redMaPPer (Rykoff et al. 2014) as large amounts of galaxy photometry already exists.

Gravitational lensing may also be used to detect these clusters through the raw property of their mass. Weak gravitational lensing can cause aberrations and deformities in an image much like a fish-eye lens with a high curvature. Techniques can be applied to identify these abnormalities and confirm the presence of a high mass system (Schneider 1996).

We can see how these detection methods would work in the composite image of Abell 370, shown in figure 1.3. We see the false colour image of the stellar light of the galaxies present in this cluster. Via this optical emission we can also observe some gravitational lensing taking place just below the central point of the image. Finally the blue overlay on the image highlights the hot intra-cluster gas in the X-ray, taken by the *Chandra* telescope. A large amount of work has been carried out both in terms of cluster detection and attempting to assess how the environments of these galaxies are impacting their development through the *nature* vs *nurture* argument. This is explored throughout this work and more details of the background can be found in sections 1.4 and 1.6 of this introduction.

1.4 Star-formation across cosmic time

Investigations focusing on the evolution of galaxies across cosmic time have been carried out for decades. These are important to understand the processes governing our Universe and how it might meet its ultimate end. Much work has been carried out in the evolution and star-formation histories (SFH) of local galaxies ($z < 0.1$). Investigations are also performed on field galaxies at higher redshifts but to yet there are not the volumes of comparable data sets in field galaxies at the peak of the star formation rate density of the Universe, the so called 'Cosmic noon'. This peak in SFH of the Universe can be seen clearly in the now synonymous plot from Madau & Dickinson (2014), shown in figure 1.4. Details of this peak have been refined over the years with ever increasing samples of galaxies across the redshift range. The clear peak at $z \sim 2$ is driven by field galaxy samples. These galaxies are largely isolated or in very

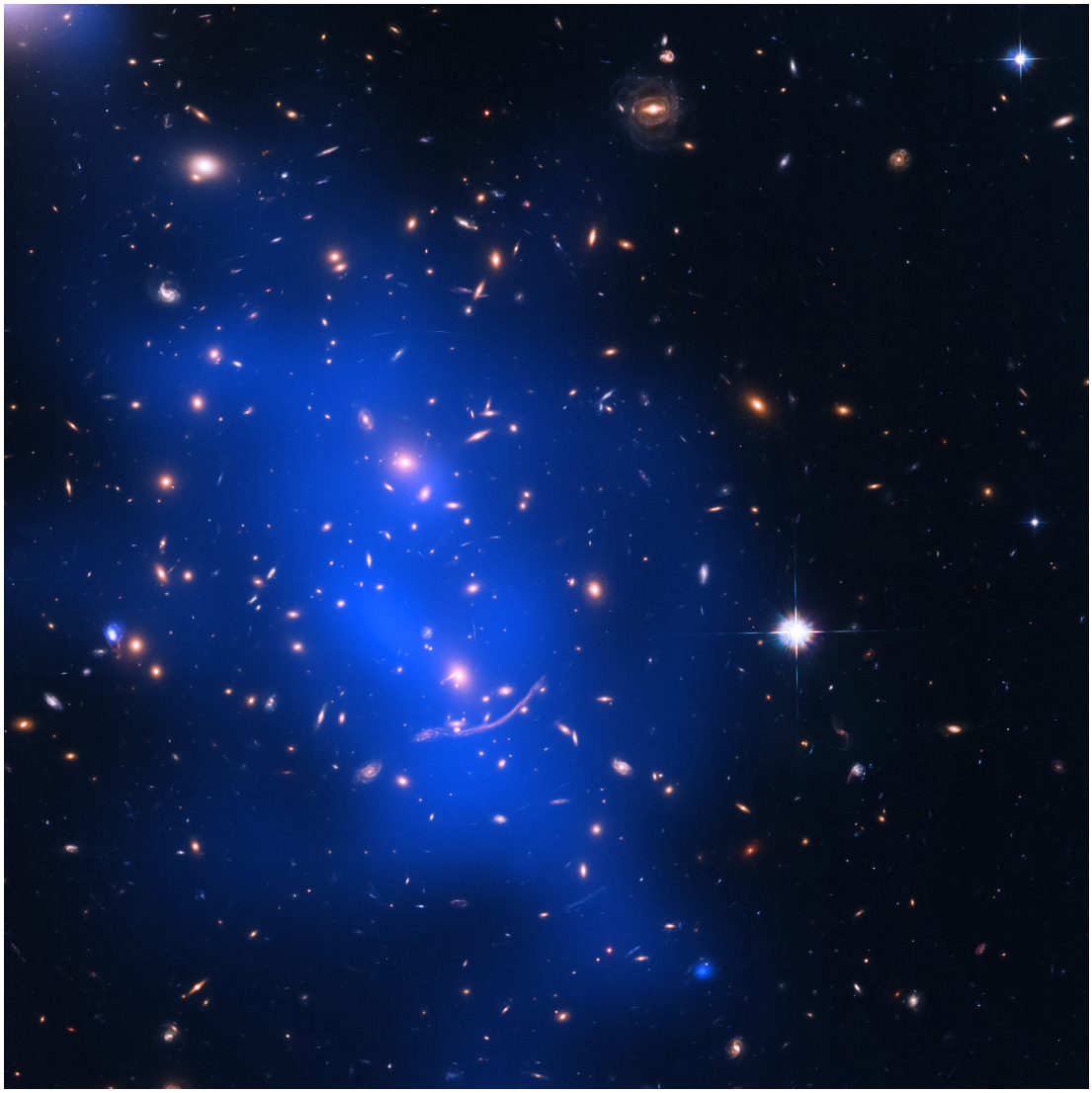

Figure 1.3: False colour optical image of the galaxy cluster, Abell 370, by *HST*. The blue extended shaded region identifies the hot X-ray intra-cluster gas of the cluster with data taken from the *Chandra* X-ray space telescope (from NASA).

small groups and with little environmental interactions to speak of. The question must be then do we see similar evolutions in SFH in galaxies in clusters across a range of redshifts. These galaxies are in a more complex dense environment, bathed in the hot gas of the ICM medium. They are far closer to their nearest neighbours on average and are within the largest gravitationally bound structures at the nodes of the cosmic web. Work carried out by Peng et al. (2010b) demonstrates this environmental dependence of star formation using a sample of SDSS galaxies, shown in figure 1.5 where we see for greater galaxy cluster density there is a larger quenched fraction for a given galaxy mass. This dependence has continued to be investigated and work carried out by Medling et al. (2018) reiterates this link comparing galaxies from different cluster overdensities highlighting that cluster environment is indeed impacting their galaxy sample from the SAMI galaxy survey with quenched fraction increasing with strength of overdensity. This link is well demonstrated in figure 1.6.

1.5 Instrumentation

We have seen so far how instrumentation and techniques throughout the ages have evolved and improved in order to widen our understanding of the processes that govern the Universe. This section aims to bring these developments together and briefly collate the historical and modern day methods in observational astronomy relevant to this work.

1.5.1 Imaging

In terms of visual astronomy, a wide range of observational techniques have been used in order to observe, and critically to measure, the phenomena we see in the Universe. For many centuries the only instrument we had to make and catalogue these observations was the naked eye. Unfortunately the magnification, sensitivity and integrating power of this instrument is extremely limited and adapted to terrestrial observation. The invention and refinement of the telescope made it a required piece of equipment for astronomical investigation and began to find use as far back as the early 17th century. Telescopes continued to get larger, use more refined optics, and combined lenses and mirrors to correct optical distortion. Even the field of metallurgy was required to keep

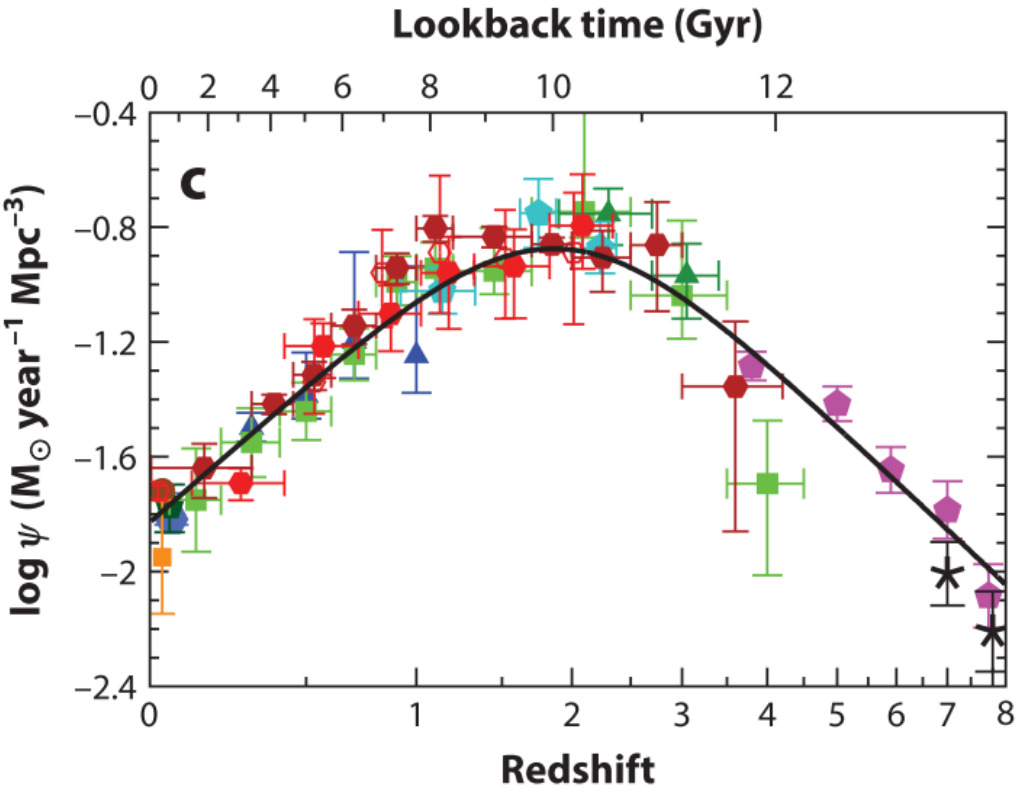

Figure 1.4: Star-formation-history of the Universe for field galaxies, (from Madau & Dickinson 2014). On the y-axis we see a volume averaged SFR, the lower x-axis shows redshift and the upper x-axis converts this to lookback time. The black curve is the fit to the combined data across cosmic time.

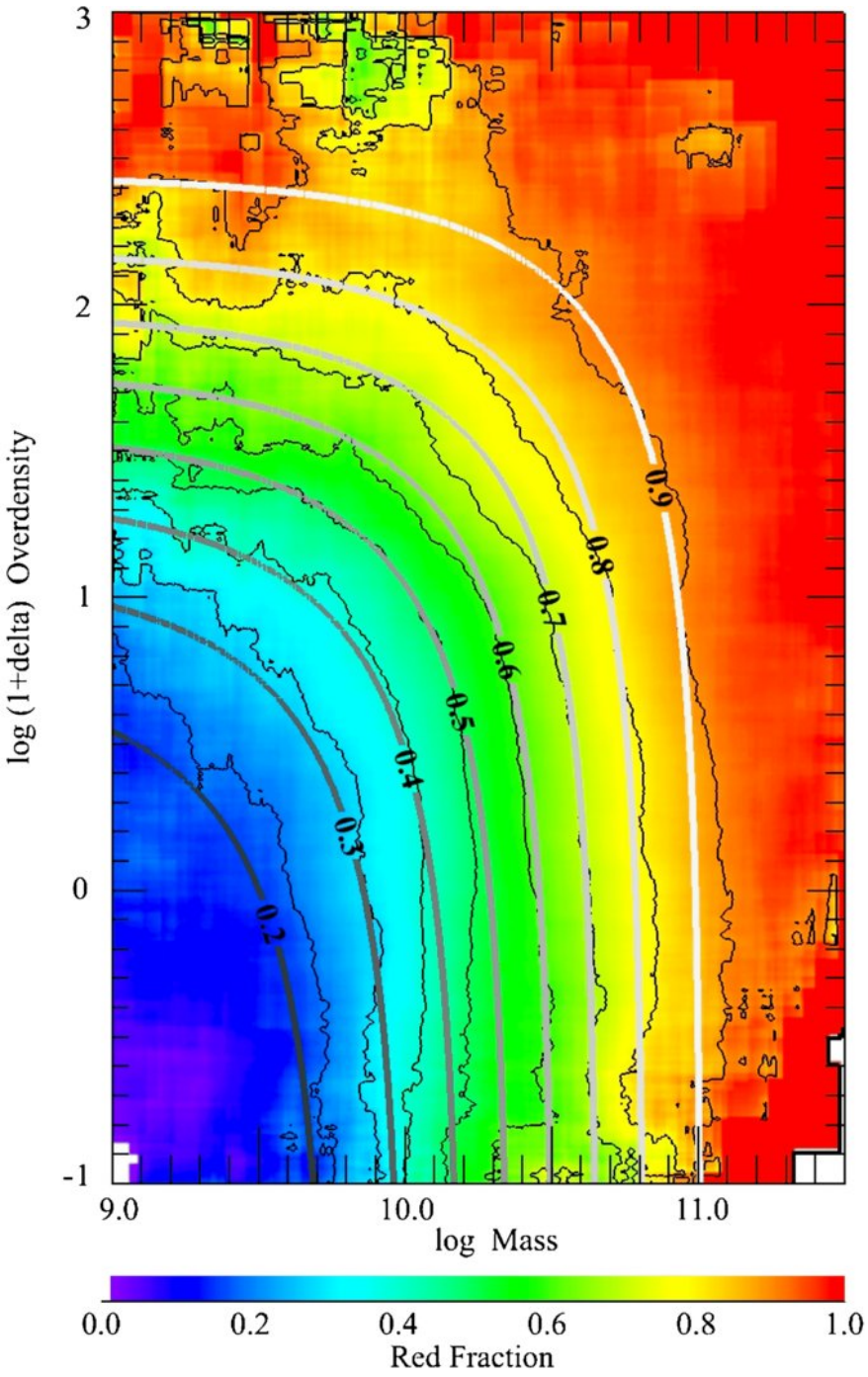

Figure 1.5: Quenched fraction of galaxies with stellar mass and galaxy overdensity, (from Peng et al. 2010b). Both are found to drive galaxy quenching. The solid curves are lines of equal redshift.

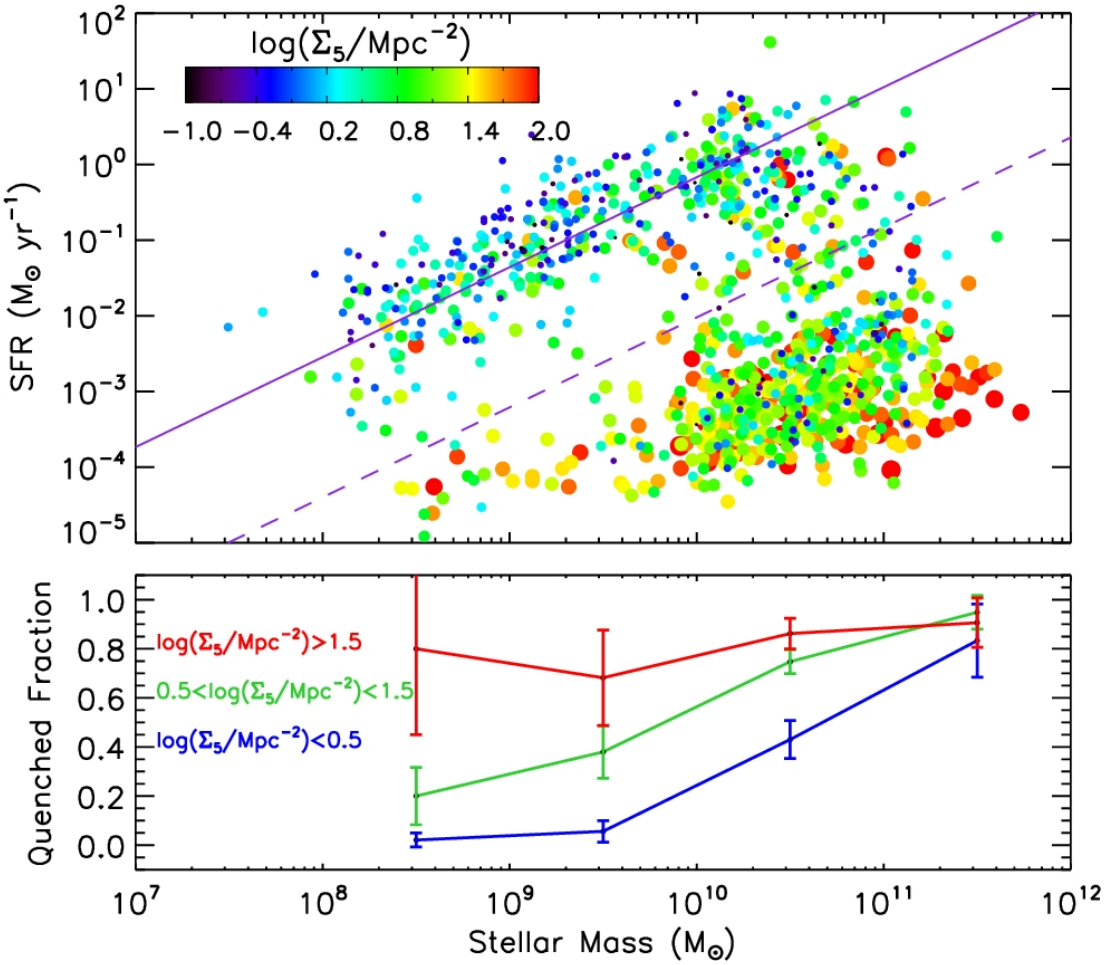

Figure 1.6: Star-formation properties of galaxies in the SAMI galaxy survey. The upper panel shows the star-forming main sequence, with the solid purple line showing a fit to the late-type spiral galaxies. Larger circles indicate higher density environments, conversely smaller circles indicate lower density environments. The purple dashed line separates the galaxies that are 3σ below the fit to late-type spirals. Lower panel indicates the sample quenched fraction with stellar mass for different environmental densities, (from Medling et al. 2018). This lower panel demonstrates that quenched fraction is constant across a range of stellar masses for denser environments, indicating environment becomes a dominant quenching factor at higher densities.

up to correct issues with mirror tarnishing and producing polished mirrors of greater size as with John Hadley in 1721 and Léon Foucault in 1857. We eventually were able to photographically image with telescopes in order to retain and further study these phenomena in greater detail. The first image of a star was taken at the Harvard College Observatory by William Cranch Bond and John Adams Whipple in 1850 as a collaboration between an astronomer and photographer. This helped to remove one of the final constraints inherent in visual observation, light integration time. However, due to a lack of linearity in many of these earlier attempts of photographic astronomy, they had limited use in scientific analysis beyond recording and visual comparison.

More sophisticated techniques have been developed and used in modern astronomy such as the charge-coupled devices (CCDs), which help to reduce a range of complications inherent in electric measurement. These devices essentially release electrons which are counted for each incident photon on the detector. These detectors have been preferred by astronomers because of their very high quantum efficiency (QE), that is the high likelihood that an electron will be released for incident photon where 100% QE would be defined by each photon releasing an electron. These have been used in astronomy since 1976 (Lesser 2015; Smith 1976). While these devices are extremely useful across many observational modes in astronomy, they are not without their drawbacks. They can be impacted by cosmic ray events, requiring data reduction pipelines to apply a variety of algorithms to remove potential incidents or that an average of several frames must be taken in order to screen for what often appear as streaks on the image. This averaging of frames also helps to reduce the CCD readout-noise which by its nature is random but is difficult to eradicate as it occurs during the transfer of the signal from the detector to voltage that can be read. We can reduce this noise by reducing the steps required to reach final storage of the data and by reducing the inherent noise of each step in the chain as much as possible.

This in itself does pose another difficulty, with the advent of imaging we are able to calculate photometric properties of the targets. We cannot, however, directly calculate the magnitude as we merely indirectly count photons. We are able to use these counts to estimate target flux and calculate instrument magnitude as in equation 1.2

$$m_{inst} = -2.5 \log_{10} \frac{F}{t_{exp}}, \tag{1.2}$$

where F here is the flux detected by the instrument, counts in this case, and t_{exp} is the exposure time of the image. In order to to generate a useful magnitude we must calibrate m_{inst} for consistency, to correct for atmospheric extinction and for comparison consistency by equation 1.3

$$m_{obs} = m_{inst} - Z + \kappa X, \tag{1.3}$$

where Z is the photometric zero point, κ is the atmospheric extinction coefficient for the observed photometric band, and X is the air mass the observations were taken at. However, determining the magnitude is not as straightforward as equations 1.2 and 1.3 would suggest as we must also determine what region of observations to count photons. For a star it might be simple to place a circular aperture around it and determine magnitude this way but for more extended objects like galaxies this is not the best solution as each galaxy has a different surface brightness profile. Profiles such as Petrosian, de Vaucouleurs, and Sérsic attempt to correct for these differences so that galaxy magnitudes can be comparable between observations and galaxies. These profiles attempt to produce a 'total' magnitude by integrating over the surface profile of the whole galaxy. This in turn presents further difficulties as the edge of a galaxy is also difficult determine due to their diffuse nature and so a defined 'effective' radius must be defined based on a proportion of the expected total emission.

When we observe a target with photometry we are measuring the integrated flux in a specific wavelength range. We can learn much about the composition of these targets by observing multiple wavelength ranges and bandwidths, also called photometric bands. We can combine observations in these bands to build a spectral energy distribution (SED), this can be fitted with model SEDs in order to obtain the properties of the galaxies such as redshift, stellar mass, SFR or age. While usually not as robust as a 'true' spectral observation an SED allows us to more rapidly build data sets and learn about the global properties of populations.

1.5.2 Spectroscopy

Counter-intuitively, spectroscopy was first used in astronomy several decades before the first images were taken. These first observations made us realise that the sun has

a distinct composition, using a prism, by noting dark lines in the projected spectrum. Due to the flaws and limitations of the prism Frauenhofer built upon previous work to develop a transmission diffraction grating for astronomical observation. Theoretically the idealised diffraction grating is governed by equation 1.4

$$d \sin \theta_m = m\lambda, \tag{1.4}$$

where d is the grating spacing, θ_m is the angle between the normal and the diffracted ray, λ is the wavelength of the ray and m is the diffraction order. Following the theme of observational astronomy these techniques were improved and refined for a wide range of astronomical investigations, and are still in use to the present day.

One of the most common types of spectrograph is the long slit, where a slit is placed before the spectrum dispersion medium in the optical path. This has the effect of controlling the resolution of the spectrograph and producing coherent spectra. However, this traditionally could only observe 1 source at a time. With more recent advancements this has changed and we are now able to use multi-slit spectrographs to observe multiple objects simultaneously within a constrained field-of-view (FOV).

Another popular method in use is that of slit-less grism spectroscopy that does not use a slit to reduce the light entering the dispersion grism. The grism itself is a medium that combines a prism and grating so that only specific wavelengths will pass through and disperse, generating the spectrum. Without a slit all of the light in the field of view passes through the grism, this has the benefit of taking a spectrum of each object within the image and also enables an astronomical imager to be quickly converted to a spectrograph. Clearly a grism based spectrograph would not be useful for a crowded field as the spectral lines would overlap and object spectra would blend and they also tend to have a lower spectral resolution.

While their uses are numerous we can use spectra to determine distances of objects based on the redshifting of distinct spectral lines when compared to their rest frame central wavelengths, as shown in equation 1.5

$$1 + z = \frac{\lambda_{observed}}{\lambda_{rest}}, \tag{1.5}$$

where z is redshift, $\lambda_{observed}$ is the observed wavelength, and λ_{rest} is the rest wavelength. Line features of these spectra can also be used as tracers of star-formation

(Cohen 1976; Kennicutt 1983) for example, using Hα or [OII]. The key observable for this thesis is the observation of the H_α emission line which is emitted via recombination of the ionized gas created by the formation of new stars, so called HII regions. This emission line, therefore, not only traces SFR but also the gas content of galaxies.

As observations will probe a specific set of wavelengths and there is no single wavelength that will probe all populations of stars within a galaxy, a calibration to calculated properties must be carried out. In the case of SFR, an initial mass function (IMF) must be used in order to extrapolate the total SFR and stellar mass (Salpeter 1955). There are several IMFs to choose from and their validity in specific observations is a matter of debate (Chabrier 2003; Kroupa 2001; Salpeter 1955).

Spectroscopy also has the ability to inform us of the metal content of objects which is important in determining their evolutionary history and ages. This is achieved using a combination of spectral lines and, therefore, as with SFR appropriate metal abundance calibrations must be applied in order to extrapolate the wider metal content from known relationships (Kewley & Dopita 2002; Pettini & Pagel 2004).

1.5.3 Integral Field Spectroscopy (IFS)

The fastest way to determine the properties of a target is photometry. The most robust way to determine chemical and kinematic properties is through spectroscopy. Slit-less grism spectroscopy aims to gain the best of both worlds but it has its limitations. Integral field spectroscopy is an attempt to retain the robustness of spectroscopy without the drawbacks of grism. We can think of IFS in a couple of different ways for example; it can be thought of as obtaining images at discrete wavelengths across a specific observational band, it can also be thought of as obtaining a spectrum per pixel of an image allowing us to spatially resolve spectral features in a single shot. The first concept of an Integral Field Unit (IFU) came in 1982 (Courtes 1982) with the first practical application coming a few years later with first light in 1987 on the Canada-France-Hawaii Telescope (CFHT) with the TIGER ("Traitement Intégral des Galaxies par l'Étude de leurs Rays") instrument.

Since TIGER saw first light, developments have been made in IFS such that three main types of IFU now exist. The initial concept began with a lenslet array for TIGER, this IFU type utilises a grid of small lenses, the output of which is fed into a multi-slit

spectrograph in order to generate the spectral array. This fundamental principle of IFS remains consistent across all types of the instrument, the final data product is an array of spectral pixels or 'spaxels'. This lenslet array has many advantages including the ease of manufacturing such an instrument and the 100% sky fill factor if the lenslets are a square or hexagonal shape. A fibre fed IFU builds on the principles of current fibre based multi-object spectrographs in that these optical fibres are placed on sky but in a grid format, the grid is then passed into a spectrograph to retain the spectral data cube. This method can be combined with the microlens array but also has the advantage of being able to convert another spectrograph into an IFU relatively simply. However, when using a fibre fed IFU we must consider the throughput losses of the optical fibre alongside the $< 100\%$ filling factor. A now decommissioned example of a fibre-fed IFU is the Sydney-AAO Multi-object Integral-field unit (SAMI; Bryant et al. 2015). A modern and recently commissioned example of a fibre fed IFU and MOS is the WHT Enhanced Area Velocity Explorer (WEAVE; Jin et al. 2023) currently installed on the 4.2m William Herschel Telescope (WHT).

The final key IFU type is the image slicer which images onto an array of mirrors which are in turn are projected onto a slit to perform the spectral dispersion. The final spatial slicing of the data is performed by the pixels of the detector grid. The fibre-fed and image slicer IFUs compliment each others optical drawbacks. Due to the nature of the fibre-fed IFU it is not possible to cryogenically cool the system to reduce infrared noise, therefore it is restricted to optical wavelengths. Whereas the image slicer generates a large scatter at optical wavelengths restricting its usefulness to the infrared regime for the moment. Beyond these key differences the clear reduction of required telescope time IFUs offer, for observations integrated over the whole galaxy, is further reduced with the introduction of multiplexing IFUs which offers the same benefit as with the use of MOS. Multiple simultaneous observations of targets allows these mutliplexing IFUs to be used as survey instruments and further increase the significance of datasets. The utility of IFUs to modern day observational astronomy cannot be understated, many of the professional facilities in use today offer IFU instrumentation for this reason. Of note is the conversion of the renowned SDSS facilities to include a multiplexing IFU on the Sloan telescope. The Mapping Nearby Galaxies at APO (MaNGA) instrument and survey have continued the legacy of providing robust data of large galaxy samples in order to understand the histories of galaxies through to their

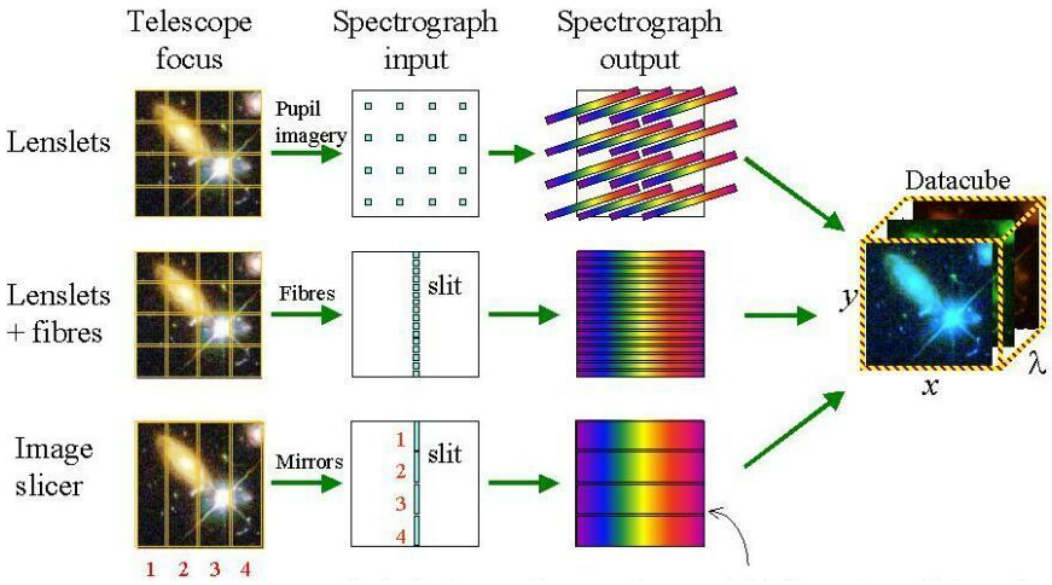

Figure 1.7: IFU types including; lenslet array, lenslet and fibre combination, and the image slicer. More details on these type of instrument can be found in section 1.5.3.
(from Durham University)

eventual deaths (Bundy et al. 2015). Diagrammatic outlines of each of these types can be seen in figure 1.7.

1.6 This work

With the advent of multiplexing Integral-field-units (IFUs) and massively multiplexed multi-object-spectrographs (MOS) the data volume of higher redshift star-forming galaxy samples are increasing, as noted in the example instrumentation and surveys chosen in this chapter. However, these larger samples focus on field galaxies both locally and at cosmic noon and on local galaxy groups and clusters. Additionally, low S/N dictates that they do not always attempt to spatially resolve kinematic and structural properties of their samples. With the use of near-infrared (NIR) wavelengths it becomes possible to probe structural and kinematic properties at the cosmic noon and begin to assess the star-formation and structural parameters of higher redshift cluster galaxies to determine what impact, if any, the environment is having on their host galaxies at this epoch. This investigation is the focus of this work and a primary aim is to increase the

samples sizes of galaxies in overdenstities at $z = 1 - 2$ for comparison to simulation and local samples.

We accomplish this primarily through both spatially resolved and unresolved emission-line diagnostics of cluster galaxies from the KMOS-Cluster-Survey (KCS), more details of which can be found in the next chapter. The sample used in this work is of star-forming galaxies in two overdensities at $z \sim 1.39$ (XMMUJ2235.3-2557) and one at $z \sim 1.46$ (XMMXCSJ2215.9-1738). These are amongst the highest redshift clusters and are located at a key point in the turnover in SFR for field galaxies at the cosmic noon. Therefore by tracing the gas kinematics, SFR, metallicities, and morphological parameters of these galaxies we can investigate SFR activity and quenching occurring within the sample and whether this is driven by environmental mechanisms. In this work we make the distinction of active and passive galaxies and clusters as those that are star-forming and those that are quenched. These clusters, while at similar redshifts, are quite different with the higher redshift cluster (XMM2215) being more active and in the earlier stages of its development, and the lower redshift cluster (XMM2235) being more passive and relaxed. This forms a good point of comparison internally to our sample as we perform the same analysis on each and so can directly compare clusters at the same epoch but with two different evolutionary states.

In section 2 we outline the data used in this investigation and the purposes and science already achieved with the KCS passive galaxy sample. We define the key goals of KCS and ancillary data sets used, along with a description of the KMOS instrument that is the primary source of data for this thesis. Chapter 3 is where we outline the work carried out in spatially resolving the kinematics of 24 of the star-forming emission line galaxy sample across the two clusters focused on in this work. We also assess the morphological properties of these galaxies and place our results in an environmental context. This is important in order to determine the properties that are being impacted by environment and in turn if these are causing differences to the star formation in field galaxy comparisons at this epoch. Here we discuss potential structural changes the these galaxies and how the environment may be influencing this. We are also able to combine our sample with the passive sample of KCS in order to further refine the redshift and cluster mass estimates of these clusters.

We move from spatially resolved properties to global line-ratio analysis of the galaxies in chapter 4 in order to determine metal content differences between these

clusters and how that may tell us about their evolutionary history. We again place this in an environmental context and make assessments of metal-content relations with mass and SFR.

We can learn much about cluster formation and evolution throughout cosmic time by studying the formation of the most massive galaxies found in the Universe and typically located at the centre of galaxy clusters. Chapter 5 focuses solely on these Brightest Cluster Galaxies (BCGs), describing the properties of a potentially forming BCG detected in XMMXCSJ2215.9-1738 at redshift ~ 1.46. We perform a photometric and 1D spectroscopic analysis of this potential BCG and discuss the findings in the context of galaxy cluster evolution, comparing properties with the passive BCG located in XMMUJ2235.3-2557 and with BCGs in local galaxy clusters samples.

In this thesis we use a cosmology with $\Omega_\Lambda = 0.7$, $\Omega_m = 0.3$, and $H_0 = 70$ km s^{-1} Mpc^{-1}. The AB magnitude system and a Chabrier (2003) IMF is utilised throughout. This work makes use of GALFIT (Peng et al. 2010a), SExtractor (Bertin & Arnouts 1996), and ASTROPY (Price-Whelan et al. 2018; Robitaille et al. 2013).

Chapter 2

KMOS Cluster Survey (KCS)

Overview

Here we describe the KMOS Cluster Survey (KCS), a near-infrared integral field spectroscopic survey of 5 overdensities, using the K-band multi-object spectrograph (KMOS) on the 8m Very Large Telescope (VLT) in Chile. We provide a technical overview of the KMOS instrument and how it probed the various galaxy samples within KCS. We outline the data reduction methodology and checks that take place to ensure quality, and include a background on how the targets were selected from ancillary data sets. We also include a brief summary of secondary data used alongside the primary KMOS data set. The emission-line galaxies from the KCS data set form the basis of the analysis presented in the remainder of this thesis.

2.1 Introduction

The use of near-infrared (NIR) wavelengths for astronomy has expanded significantly over the last two decades, with the introduction of VLT class of facilities, the design and launch of JWST, and to future observations with Euclid. However, this push into these wavelengths would not have been possible without building upon work across the previous decades, as is a common theme in astronomy. Work carried out by the United Kingdom Infrared Telescope (UKIRT; Humphries & Purkins 1980) as one of the largest dedicated infrared telescopes in the world demonstrated the utility to a wide range of fields in observational astronomy of these wavelengths. This is paired with the Visible and Infrared Survey Telescope for Astronomy (VISTA; Dalton et al. 2006; Emerson, McPherson & Sutherland 2006), which despite being of similar age to UKIRT will soon be operating as the site of the 4-metre Multi-Object Spectrograph Telescope (4MOST;de Jong et al. 2012) which will provide a large volume of fibre spectroscopy via survey observations. NIR astronomy has a wide utility across many class of object and range of redshift. While its utility is clear, ground based observations at these wavelengths are subject to significant sky interference. Efforts have been made to selectively filter these wavelengths using the development of fibre Bragg gratings (FBGs) over the last couple of decades, use of these gratings allows the suppression of emission lines that are matched to many of the OH lines present across this band of the spectrum. Attempts are also commonly made to make telluric sky subtractions but this is particularly difficult at certain bands of NIR observation, such as H-band ($1.3 - 2.0\mu m$) as sky emission varies in the order of minutes to hours (Oliva et al. 2015). Removing this atmospheric contribution remains the best way on ensuring quality of NIR data and so a number of modern facilities aim to locate above a significant portion of the atmosphere (VLT, E-ELT), with facilities such as JWST removing this contribution altogether by locating in space.

NIR data are significant for the work outlined in this thesis for two main reasons. The first is the targeted wavelengths at the redshift of this work ($z \sim 1.4$) is well aligned with optical wavelengths in the local Universe, which increases the samples available for cross comparison (e.g. SAMI-GS; Medling et al. 2018). The second is that these wavelengths are much less impacted by dust extinction, effectively giving us the ability to 'see through' the intervening optically observed dust contributions and

focus on the galactic gas. We are also able to make use of high quality imaging taken at other facilities at comparable wavelengths to improve our interpretation of the spatially resolved features of the galaxies in question.

These benefits have already been used to great effect in other galaxy surveys in the past decade including the KMOS Redshift One Spectroscopic Survey (KROSS) which studied spatially resolved kinematics and metal properties of field galaxies at $z \sim 1$ (Stott et al. 2016). Work at intermediate redshifts include that performed with the KMOS-Cluster Lensing And Supernova survey with Hubble (K-CLASH) which aimed to compare field and cluster galaxy counterparts in $z \sim 0.2 - 0.6$ (Tiley et al. 2020). While this work has been carried out sample sizes of surveys of cluster galaxies remain relatively small, especially compared to the samples of hundreds of galaxies observed in individual surveys of field galaxies. This is where multiplexing IFU instrumentation becomes a great asset by being able to simultaneously gather data from many galaxies in the highest redshift galaxy clusters. This will allow greater samples of galaxies in clusters at these redshifts to be analysed and gain statistically reliable results of galaxy properties at the so called 'cosmic noon'.

2.2 KMOS

The K-Band Multi-Object Spectrograph (KMOS; Sharples et al. 2013) is a multiplexed Integral Field Unit (IFU) currently mounted on VLT Unit-Telescope 1. As of first-light (21 November 2012) KMOS consisted of 24 individually deployable IFUs within a $7'.2$ diameter circular patrol field, as shown in figure 2.1. This instrument helped to cause a step change to NIR astronomy by providing a multiplexing capability to spatially resolve the spectroscopic features of multiple targets simultaneously. There are two key points to remember when considering the observational argument for IFU data, photometric imaging is quick and has high spatial resolution and spectroscopy provides more expansive diagnostics, such as kinematic and line-ratio information which is key to determining how objects have evolved and how they may interact, but is much slower. IFUs are an attempt to combine the best features of these two modalities. The utility of NIR astronomy to modern observational astronomy is clear but when combined with the powerful class of instrument of an IFU this makes KMOS a desirable instrument

across a range of sub-fields by allowing spatial spectroscopic sampling simultaneously in a grid.

The data provided by an IFU can be thought of in multiple ways, one is an image is provided at each spectral resolution element for the observing band in use. Another could be that they provide a spectrum per spatial pixel of the IFU. The spectral pixels are termed 'spaxels' and can be utilised in a variety of ways to determine a range of properties of an observed object. Current IFU instrumentation is beginning to expand their utility by offering a multiplexing capability (KMOS, VIRUS, WEAVE). KMOS makes use of the image slicer technique outlined in the Introduction of this work (section 1.5.3) and shown in the diagram of figure 2.2.

The detectors used by KMOS are Teledyne substrate-removed Hawaii 2RG detectors that are cooled to approximately 40K while the rest of the KMOS cryostat is kept at 120K. KMOS is compartmentalised into three modules that contains 8 IFUs, a spectrograph and detector which enables instrument use even if a detector or spectrograph fails. Contrary to what the name KMOS might suggest the instrument is capable of observing a range of NIR bands from $0.8 - 2.5\mu$m with spectral resolving power ranging from $R = 2000 - 4200$.

Each IFU consists of a $2.8'' \times 2.8''$ spaxel grid of with a spatial sampling of $0.2'' \times 0.2''$ spaxels. As with multiplexing observations, particularly fibre-fed multi-object spectrographs (MOS), there are practical limitations to the separation of the arms within the instrument field-of-view (FOV). For KMOS this includes no more than 3 IFUs within an arcminute squared box and each IFU must achieve a minimum separation of $6''$ from its nearest neighbour.

2.3 KMOS Cluster Survey (KCS)

The KMOS Cluster Survey (KCS) is a 30 night KMOS GTO programme focused primarily on passive galaxies in four over-densities at $1.04 < z < 1.8$, the details of which are shown in table 2.1. KCS performed deep ($\sim 15 - 20$ hours) absorption line spectroscopy of $20 - 40$ galaxies in each overdensity. This improved the statistical reliability of the study of the environmental impact of passive galaxies in over-dense regions, which has previously been relatively sparse. A summary of the main science

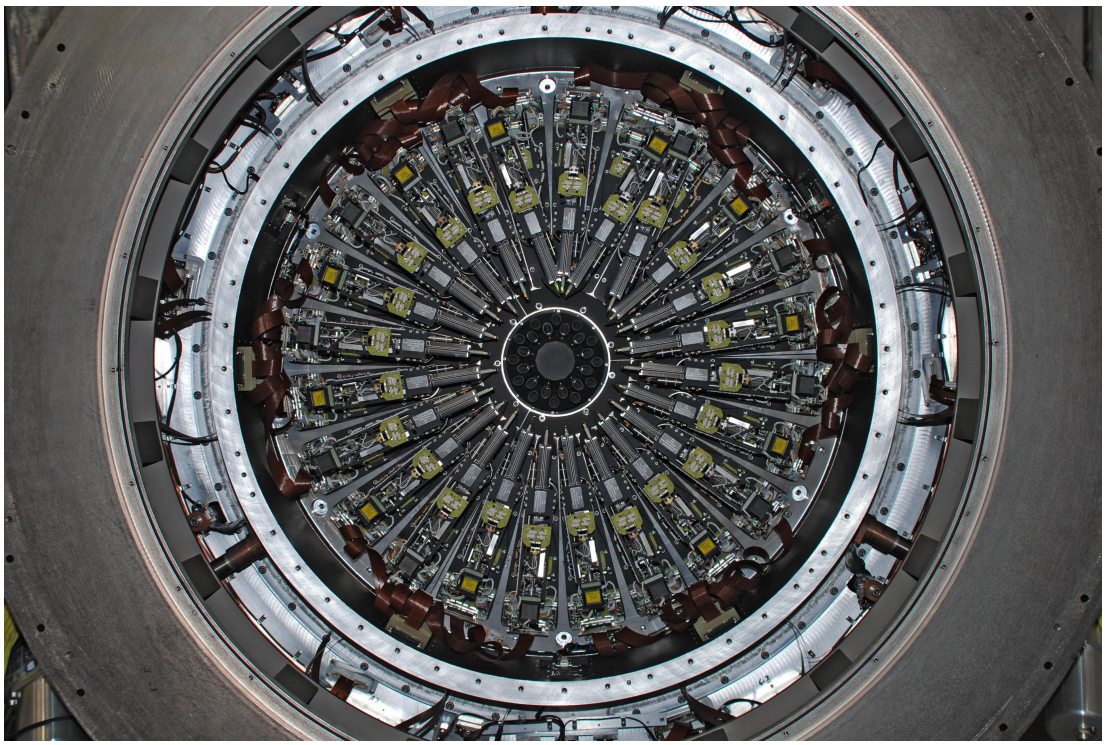

Figure 2.1: The 24 IFU arms of KMOS arranged in a circular aperture, (from ESO)

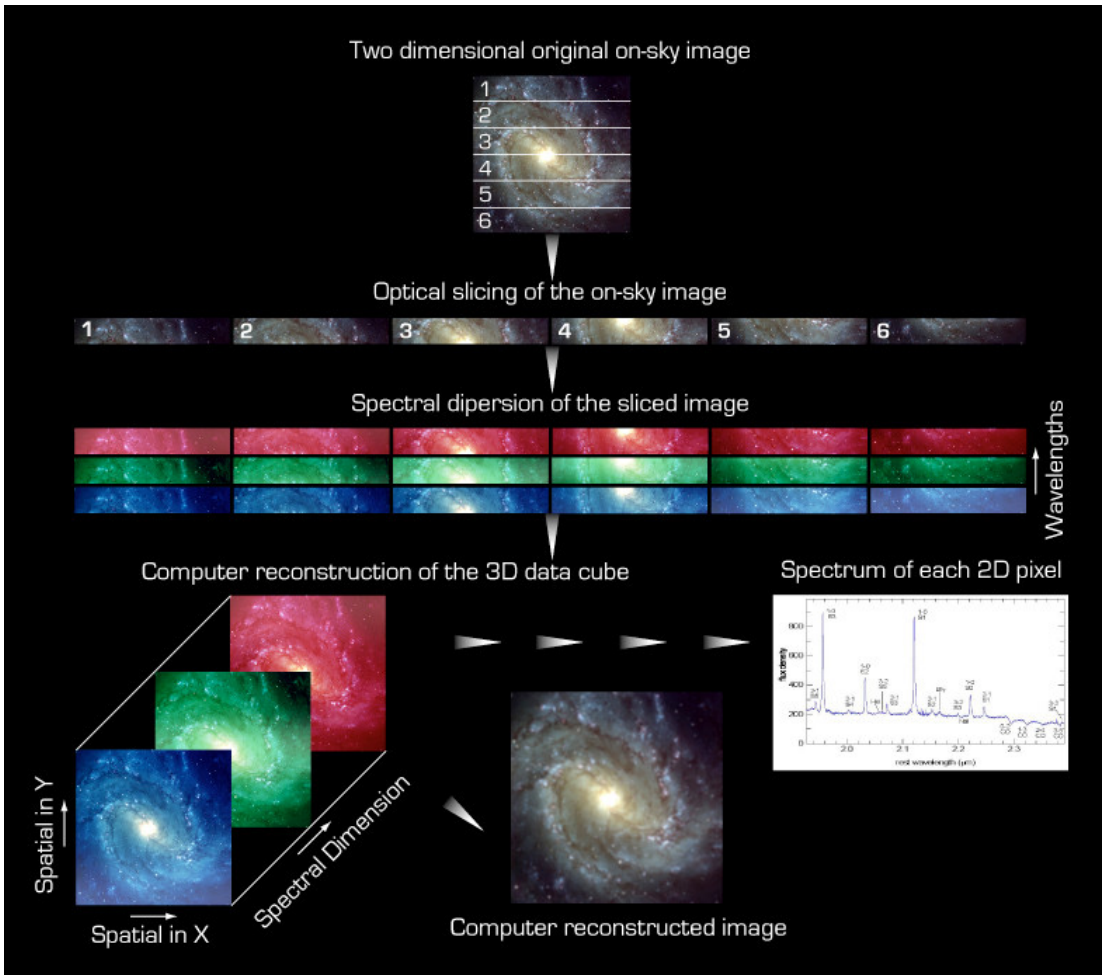

Figure 2.2: An image slicer showing each stage of an image slicing IFU, (from ESO)

Table 2.1: Galaxy clusters observed in KCS. Note that two of these clusters also had a sample of star-forming emission line galaxies observed, these are denoted with an asterisk (*) and are the main focus of this thesis.

Galaxy Cluster	Redshift	$M_{200}\,(h^{-1}M_\odot)$	R.A. (J2000)	Decl. (J2000)
XMMU J2235.3-2557*	1.39	$7.7^{+4.4}_{-3.1} \times 10^{14}$	338.8	-26.0
XMMXCS J2215.9-1738*	1.46	$2.1^{+1.9}_{-0.8} \times 10^{14}$	334.0	-17.6
CL 0332-2742	1.61	$0.64^{+0.3}_{-0.3} - 1.2 \times 10^{14}$	53.1	-27.8
JKCS 041	1.80	$\sim 10^{14}$	36.7	-4.7

results of KCS can be seen in three papers (KCS I; (Beifiori et al. 2017), KCS II; (Chan et al. 2018), KCS III; (Prichard et al. 2017)). The data collected from this survey represents one of the largest spectroscopic samples of passive galaxies in over-densities at $z > 1.3$ (Beifiori et al. 2017).

The target clusters were selected as they are some of the best studied clusters above $z = 1$. The clusters also have a large number of spectroscopically confirmed members, which increased galaxy selection efficiency. They also have a wealth of archival data, including *HST* multi-band photometry and deep ground-based imaging from VLT.

While KCS initially concentrated on passive galaxies, the focus of this thesis is on the emission line spectroscopy of the star-forming population of the two over-densities XMMXCSJ2215.9-1738 ($z \sim 1.47$) and XMMUJ2235.3-2557 ($z \sim 1.39$), hereafter XMM2215 and XMM2235 respectively. The data was obtained during Period 98 with run ID 098.A-0204 between 16 - 20 October 2016.

The first work published with the KCS dataset found in Beifiori et al. (2017) focused on the passive galaxy population in three of the overdensities; XMMU J2235.3-2557, XMMXCS J2215.9-1738, and CL 0332-2742 (hereafter XMM2235, XMM2215, and CL0332 respectively). This analysis concentrated on un-resolved absorption line spectroscopy of this galaxy sample coupled with *Hubble Space Telescope* (HST)/Wide Field Camera 3 (WFC3), *HST*/ACS, or Subaru/MOIRCS imaging along with astrometry from VLT/High Acuity Wide field K-band Imager (HAWK-I). The final dataset consisted of 19 galaxies spread across the three clusters. KCS I used this data to study the Fundamental-Plane (FP) which is a relation that early-type galaxies in the local Universe follow. This relation connects surface brightness, effective radius, and velocity dispersion. This relation has a well established zero-point and evidence of redshift evolution has been indicated. This is likely due to a larger proportion of younger stellar

populations at higher redshift alongside a contribution from galaxy structural evolution over redshift. From an environmental point of view there is also a contribution from accelerated size evolution in clusters compared to field galaxies at $z \sim 1.4$ (Chan et al. 2018; Delaye et al. 2014; Lani et al. 2013; Strazzullo et al. 2013). Some of the final conclusions drawn from this work include tentative evidence that the galaxies in more massive clusters formed at earlier times, the FP B-band zero-point (0.443 for local cluster Coma) evolves with redshift ($-0.10 \pm 0.09, -0.19 \pm 0.05, -0.29 \pm 0.12$ for $z = 1.39, 1.46, 1.61$ respectively) and a trend with median galaxy stellar mass is suggested. This trend with stellar mass (see figure 2.3) shows that the clusters that contain the most massive galaxies tentatively indicate higher redshifts of cluster formation.

The work in Chan et al. (2018) focuses on the same clusters as those from Beifiori et al. (2017) and concentrates on the structural properties of the passive galaxy sample of these three clusters. In order to undertake this analysis those authors use photometry from *HST*/WFC3, *HST*/ACS, and VLT/HAWK-I. This work assessed the mass-size relation between the clusters and compared with local samples and continued to apply a stellar-mass weighting to these assessments. The authors found that the sizes of passive galaxies in the three clusters from the work are smaller than expected from the local mass-size relation on average in the same rest-frame wavelength (see figure 2.4). Comparisons to field samples demonstrate that cluster galaxies undergo much faster structural evolution compared to their field counterparts based off comparing the mass-weighted size distribution of these galaxies to field galaxies at similar redshift.

Prichard et al. (2017) focuses on the single remaining cluster at $z \simeq 1.80$, JKCS 041, the highest redshift cluster in the KCS sample. They focus primarily on the stellar kinematics and structural parameters and builds on the work performed in Beifiori et al. (2017). Here the authors make use of the deep absorption-line spectroscopy from KMOS and *HST* imaging to derive their results. A key result from this work is tentative evidence JKCS041 is forming and comprises of two merging galaxy groups, found by an analysis of the ages of the cluster members compared to their relative velocities within the cluster (see figure 2.5). This result demonstrates the connection between large-scale structure and galaxy age at $z \sim 1.8$.

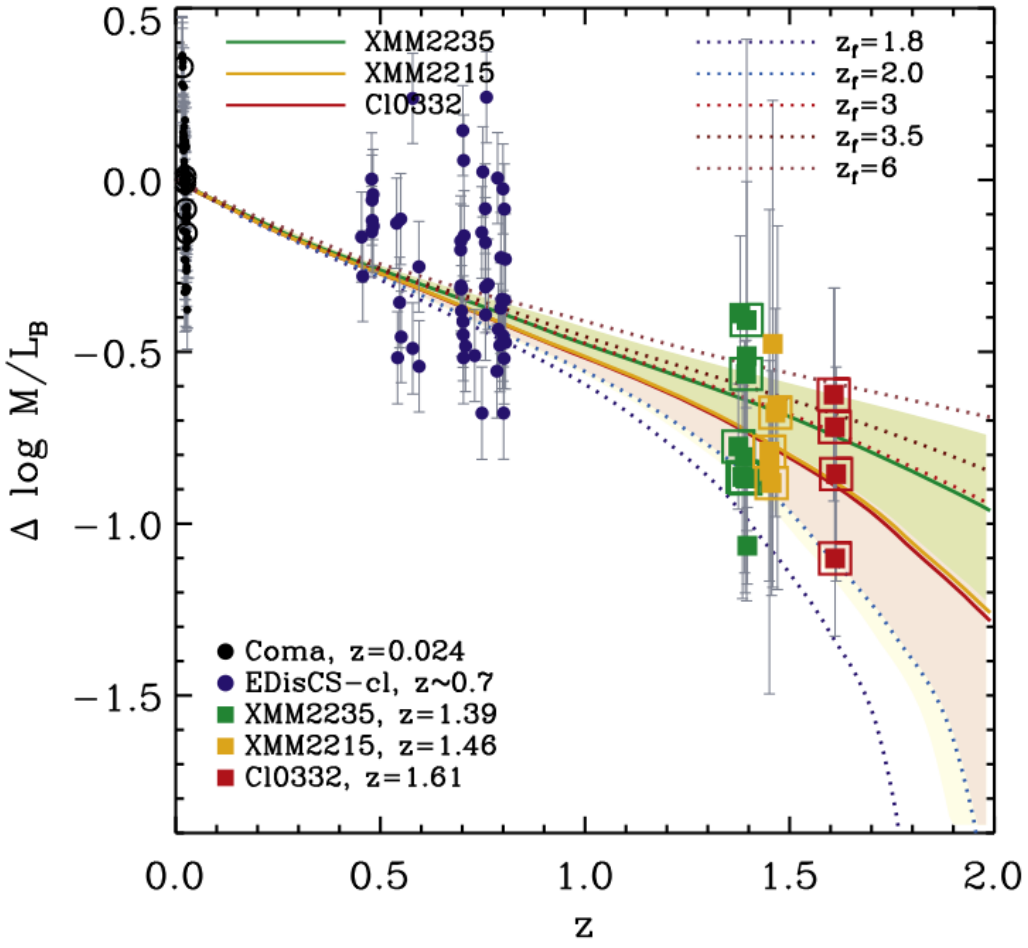

Figure 2.3: Redshift evolution of the fundamental plane highlighting a key conclusion from KCS I that more massive galaxy clusters contain galaxies that formed at earlier times (from Beifiori et al. 2017). The y-axis here indicates the rate of change in B-band mass to light ratio to determine formation ages of these clusters. The dotted lines indicate predictions from simple stellar populations with formation ages corresponding to each of the cluster derived ages, the solid curves show fits for each cluster.

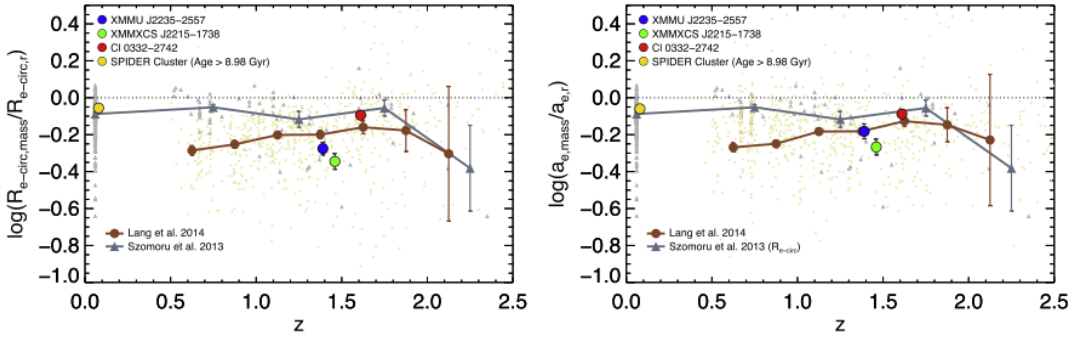

Figure 2.4: The offset of the mass-size relation of two of the galaxy clusters from the KCS sample, providing further evidence of accelerated structural evolution of the galaxies in these clusters, highlighting a key conclusion from KCS II, (from Chan et al. 2018). The coloured circles indicate median properties for each cluster. The brown points indicate the binned median parameters from a comparable study. Likewise the grey points are comparisons of a second external study but for field galaxies.

2.4 The cluster galaxy sample used in this work

XMM2215 is a massive over-density with extended X-ray emission and a mass of $M_{200} = 2.1^{+1.9}_{-0.8} \times 10^{14} h^{-1} M_{\odot}$ (Beifiori et al. 2017; Stanford et al. 2006; Stott et al. 2010). X-ray luminosity and temperature are $L_X = 2.92^{+0.24}_{-0.35} \times 10^{44}$ erg s^{-1} and $T_X = 4.1^{+0.6}_{-0.9}$ keV (Hilton et al. 2010). Studies of the luminosity function indicate a high-mass galaxy population (Strazzullo et al. 2010). Although there is no clear brightest cluster galaxy (BCG), the brightest spectroscopically confirmed member is ~ 300 kpc from the X-ray centroid (Stott et al. 2010). This cluster contains a number of emission-line and dusty star-forming galaxies, and AGN throughout, demonstrating that it is still very active, as defined in section 1.6 (Hayashi et al. 2010; Hilton et al. 2010; Ma et al. 2015). One of the IR/sub-mm sources appears to be a multiple merger in the cluster core and may be the forming BCG (see chapter 5). The targets observed can be seen in figure 2.6. Three of our targets in XMM2215 also cross match with $24\mu m$ sources from (Hilton et al. 2010) and two of these cross match with $850\mu m$ sources from (Ma et al. 2015).

XMM2235 is a very massive cluster for its epoch at $M_{200} = 7.7^{+4.4}_{-3.1} \times 10^{14} h^{-1} M_{\odot}$ and is likely virialised (Stott et al. 2010). X-ray luminosity and temperature are $L_X = 8.5 \pm 0.4 \times 10^{44}$ erg s^{-1} and $T_X = 8.6 \pm 1.3$ keV (Lerchster et al. 2011). The X-ray emission of this cluster indicates a dynamically relaxed state, i.e. a large number

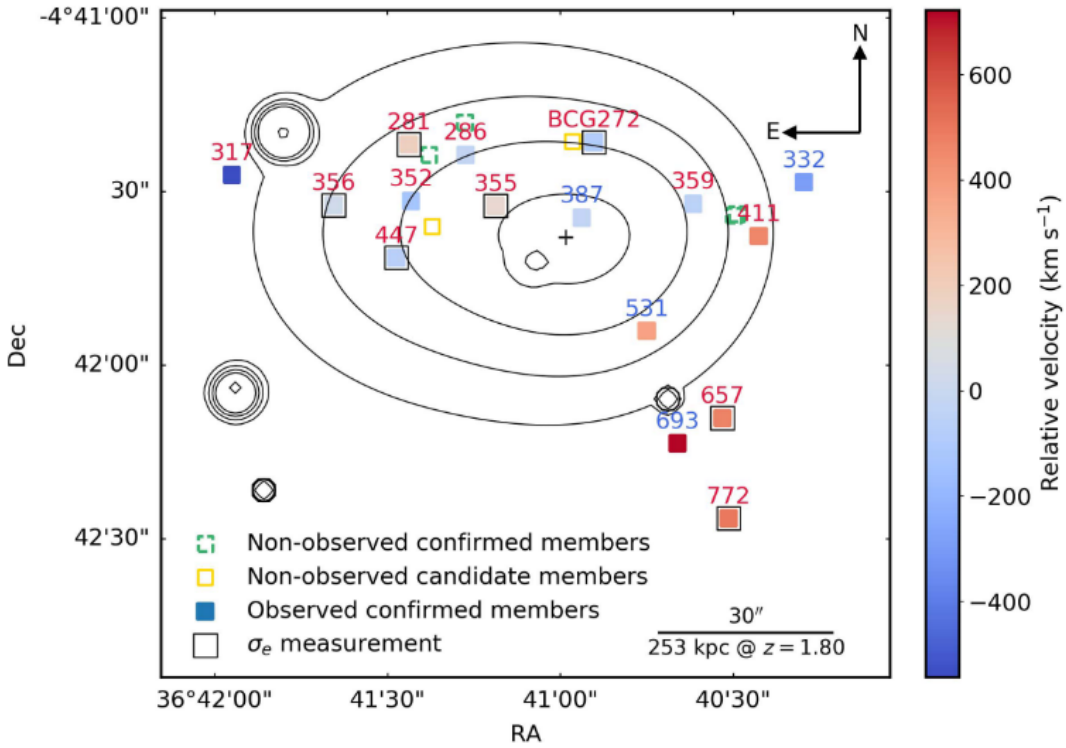

Figure 2.5: The relative velocities and their spatial distribution within JKCS 041 demonstrating, in part, the two groups making up the cluster, a key conclusion from KCS III, (from Prichard et al. 2017). Red galaxy ID labels indicate passive galaxies while blue ones indicate star-forming galaxies. The black contours indicate the X-ray emission with the geometric center indicated by the black plus sign. Unobserved confirmed members are green dashed squares while unobserved candidate members are solid yellow squares.

of virialised galaxies and developed core, due to the centrally peaked profile. As investigated by (Strazzullo et al. 2010), the luminosity function indicates a high-mass population, which suggests this cluster is already at an evolved mass-assembly stage. Unlike XMM2215, the star-forming galaxies located in this cluster are not generally present in the core and as such it appears to have more passive and mature stellar populations, in keeping with its greater halo mass (Beifiori et al. 2017). Again, the targets observed can be seen in figure 2.6. Combined with their respective masses, this difference in star formation activity indicates that, while these two clusters are at a similar redshift, they appear at different stages in their evolution with XMM2215 being the younger of the two clusters.

XMM2215 and XMM2235 have been observed with VLT/KMOS, HST/WFC3 F160W, and VLT/HAWK-I. These clusters were selected due to the large amount of multiband ancillary data and large numbers of spectroscopically confirmed members. The galaxies targeted in these clusters are known Hα or [OII] emission line galaxies discovered using the narrow-band technique for XMM2235 (Grützbauch et al. 2012) and XMM2215 (Hayashi et al. 2010). Some galaxies from (Hilton et al. 2010) with known spectroscopic [OII] emission were also included. The final galaxy selection was further refined by choosing the objects with lowest contamination from sky emission or telluric absorption. This sample is not complete nor completely representative of the entire population of galaxies located in these two clusters. As the aim of this work is to determine the properties of a specific population, star-forming galaxies, and how their star-formation is impacted on environment a selective sample is valid. Of concern is how representative this sample is across the different regions of the cluster and the galaxies were also chosen, where practical, to cover these regions. Additionally to this the targets in this sample were not all detected with an acceptable signal-to-noise despite the selection criteria outlined here. This will leave gaps in the sample that may worsen the incomplete region sampling.

2.5 KMOS data reduction

The IFUs each have a spatial area of $2''.8 \times 2''.8$. The IFU width corresponds to ~ 24 kpc at $z = 1.4$ (8.43 kpc/$''$), which is several times the half light radius of most of the

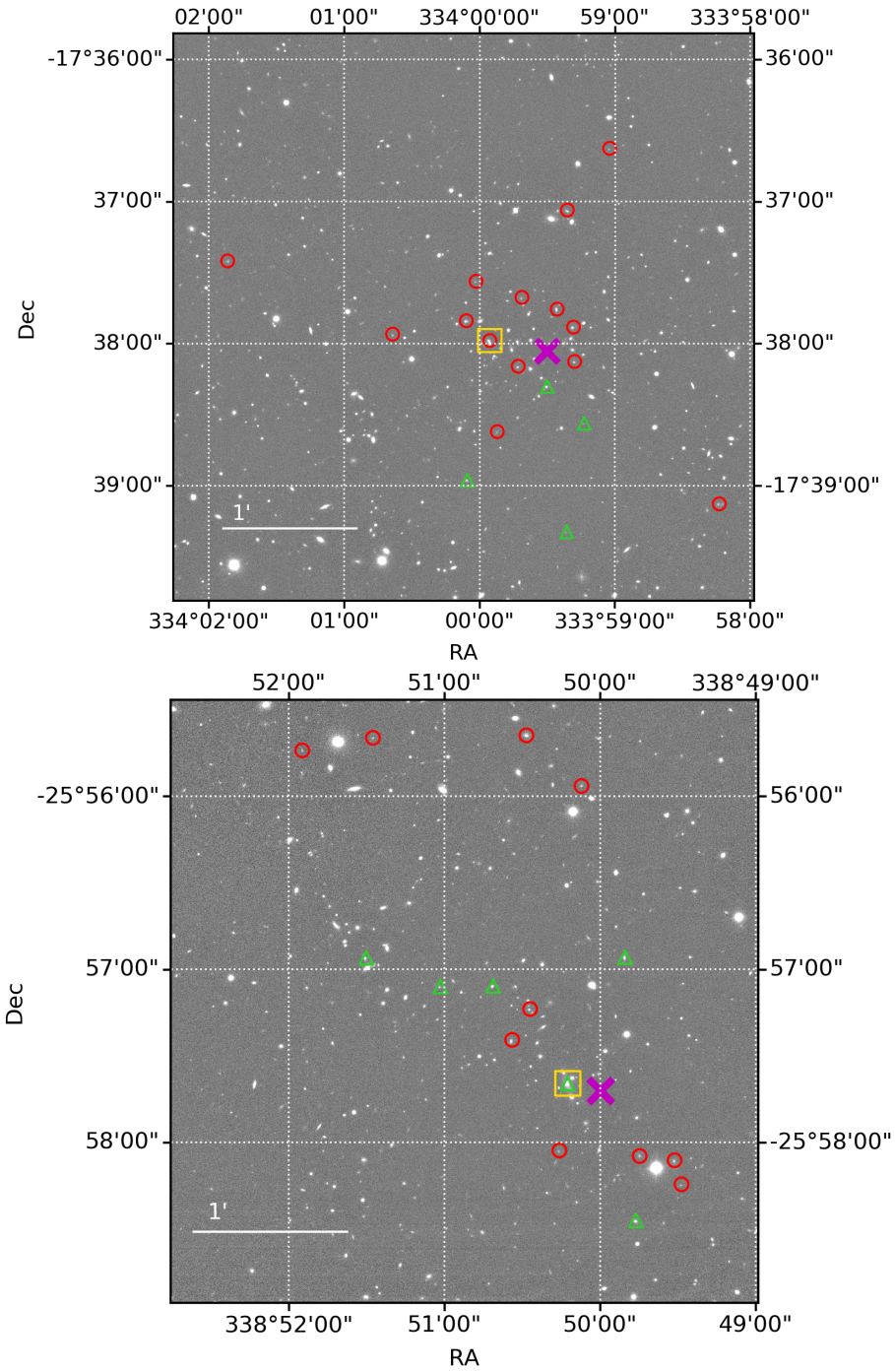

Figure 2.6: *top*: A VLT/HAWKI K_s-band image of the cluster XMM2215, highlighting the galaxy targets with KMOS (green triangles and red circles). The galaxies highlighted with red circles are those that we detect extended Hα emission in the KMOS data. The magenta cross indicates the X-ray emission centroid and the yellow square indicates the merger driven ULIRG which may be the forming BCG of the cluster (note that XMM2215 does not have an unambiguous BCG). *bottom*: The equivalent plot for XMM2235, with the BCG highlighted with a yellow square.

galaxies observed at this redshift (see section 3.3.1.3) so we are confident that each IFU contains the majority of the flux of its target galaxy. The spatial resolution of KMOS is $0''.2 \times 0''.2$ per pixel. Our targets are at $z \sim 1.4$ and so we use the $H-$band grating in order to cover the redshifted Hα and [NII] lines.

The observations were prepared using the KMOS Arm Allocator (KARMA) (Wegner & Muschielok 2008) with ~ 20 arms per cluster used to observe the targets. The remaining arms observe one sky IFU for each of KMOS' three spectrographs to monitor the sky emission, and a relatively faint star to monitor the *point-spread-function* (PSF).

The observations took place on the nights of the 16-19th October 2016 (ESO programme ID 098.A-0204(A) and 098.A-0204(B), P.I. Davies). The seeing during these observations was consistently $\sim 0.7''$, which provided us with a homogeneous and reliable dataset. The two cluster fields were each observed for a total on-target integration time of ~ 6 hours (72×300 seconds) with an object (O) - sky (S) pattern of OSOOSOOSO such that every object frame has an adjacent sky frame, in order to best compensate for sky variability in the H-band and provide a good signal-to-noise (S/N).

The data reduction was performed using the ESOREX / SPARK pipeline (Davies et al. 2013). This extracts slices from each IFU and performs the necessary flat-field, illumination correction and wavelength calibration in order to form the data cube. The reduction was carried out following the same procedure used for KROSS (Stott et al. 2016). To replicate this technique, we reduced each 300s frame separately and removed the majority of the sky emission by combining individual temporally adjacent OS (object-sky) pairs such that a sky frame is subtracted from the object frame. To improve this initial sky subtraction, we use the residual sky emission remaining in that spectrograph's dedicated sky IFU. An average 1D residual sky spectrum is created from this O-S subtracted sky IFU, which is then appropriately scaled and subtracted from each spaxel in the O-S object frame. This average residual sky does not add significant noise compared with subtracting the residual sky cube spaxel-by-spaxel.

The O-S object frames with the residual sky removed are then combined into a final reduced data-cube using a clipped average and oversampled to $0''.1$ per spaxel. The flux calibration is performed using a standard star observed on one IFU per spectrograph such that each has an independent zero-point.

Chapter 3

Kinematics of cluster galaxies at $z \sim 1.4$

Abstract

We present spatially resolved kinematics and photometric properties of 24 star-forming galaxies in two galaxy clusters at $z \sim 1.4$ from the emission line sample of the KMOS Cluster Survey (KCS). XMM2235 is a relaxed cluster with a generally quiescent inner core whereas XMM2215 is dynamically unrelaxed with active star-formation throughout. We quantified kinematic, star-formation and morphological properties of these galaxies, and assessed the impact of their positions in cluster phase space. We found that the location within the cluster environment has little impact on the kinematics of these galaxies, as they are very similar to samples of field galaxies at this epoch. The galaxies generally being turbulent disks, which is presumably driving their high SFR at this epoch as it does for the field population. Differences do occur in terms of morphology and star-formation between the active and more relaxed cluster. We found that more kinematically disturbed galaxies have higher sSFR, especially when considering the more active cluster. We showed that galaxies in the relaxed cluster tend to be rounder in the core of this cluster, perhaps indicating that morphological transformation is preceding cessation in star-formation. We also utilised these data to update the cluster redshifts (XMM2235: $z = 1.3930 \pm 0.0006$,

XMM2215: $z = 1.4570 \pm 0.0002$). Our cluster dynamical mass estimates also agreed well with those derived from X-ray gas observations.

3.1 Introduction

The star-formation history (SFH) of the Universe has been well studied for the general galaxy population (e.g. Madau & Dickinson 2014); it clearly shows a rise in volume averaged star formation rate (SFR) from early times to a peak at "cosmic noon", corresponding to approximately $z = 1 - 2$, followed by a downturn to the present day. This subsequent reduction in SFR is thought to be due to secular quenching processes such as: Active-Galactic Nuclei (AGN) feedback (Fabian 2012; Förster Schreiber & Wuyts 2020; Kauffmann & Haehnelt 2000), supernova (SN) feedback (Davis, Khochfar & Dalla Vecchia 2014; Governato et al. 2010; Mashchenko, Wadsley & Couchman 2008), morphological quenching (Martig et al. 2009), and other internal, mass-quenching processes such as Halo-quenching (Casado et al. 2015; Peng et al. 2010b). However, observations of the SFH of the Universe are derived overwhelmingly from galaxies in the field environment and not those in clusters.

Numerous studies demonstrate the importance of environment for accelerating galaxy quenching (Casado et al. 2015; Medling et al. 2018; Peng et al. 2010b; Tiley et al. 2020). Indeed, environmental quenching processes contribute in addition to the secular processes discussed above, as shown by the prevalence of passive galaxies in clusters up to $z \sim 1$ (Dressler 1980; Dressler et al. 1999; Peng et al. 2010b). Some additional processes that can modify the SFR of cluster galaxies are;

(i) Ram-pressure stripping (Gunn & Gott, J. Richard 1972): a rapid quenching process (~ 1 Gyr) caused by a galaxy falling into a cluster and moving through the intra-cluster medium (ICM), which exerts a force on the cold gas in the disc, removing it from the galaxy.

(ii) Strangulation (Larson, Tinsley & Caldwell 1980): a slower process (~ 3 Gyr) in which a galaxy is unable to accrete gas from its halo however, it continues to form stars with the gas already present in its disc which, over time, depletes without additional accretion.

(iii) Harassment (Moore et al. 1996): multiple high-speed encounters between galaxies that has the effect of increasing SFR which causes a "starburst", eventually leading to quiescence due to the more rapid processing of gas into stars. These interactions are distinct from other merger processes and are more likely than mergers

in clusters due to the much higher relative velocities of galaxies in clusters than those in the field.

These secular and environmental processes are quantifiable and can be separated from each other when considering the star-formation histories of galaxies in the field compared to those in overdense regions (Casado et al. 2015). It has been observed that there is a reversal in the SFR - local density relation at high redshift, indicating that galaxies in clusters should experience a higher SFR than their field counterparts so their greater stellar masses can accumulate by $z \sim 1$ (Hilton et al. 2010; Strazzullo et al. 2013; Tran et al. 2010).

Integral-field-spectroscopy (IFS) is a highly valuable tool in observational astronomy, allowing the observer to gain spatially resolved spectroscopy in a single observation. The power of IFS data analysis in galaxy studies and kinematic investigation has already been proven through many surveys (Beifiori et al. 2017; Medling et al. 2018; Stott et al. 2016). Indeed, IFS studies have expanded our understanding of the peak in the SFH of the Universe with results indicating that gas-rich disks are more turbulent at $z \sim 1 - 3$ (Förster Schreiber et al. 2009; Stott et al. 2016; Swinbank et al. 2012; Wisnioski et al. 2015), contrary to the local Universe when the turbulence in these disks is much lower. This is the likely driver of the peak in the SFH for field galaxies. Another result from Tiley et al. (2021) infers a strong link between halo and host galaxy angular momentum across a range of redshifts and stellar masses suggesting that massive star-forming disc galaxies have followed a similar assembly path since $z \simeq 1.5$.

The increased prevalence of multi-plexed IFS facilities, e.g. Very Large Telescope (VLT)/K-band Multi Object Spectrograph (KMOS; Sharples et al. 2013), Anglo Australian Telescope (AAT)/Sydney-Australian-Astronomical-Observatory Multi-object Integral-Field Spectrograph survey (SAMI; Croom et al. 2012) is greatly improving the sample size of resolved kinematics of galaxies in clusters. These capabilities are further expanded with the introduction of the multi-plexed William Herschel Telescope (WHT)/WHT Enhanced Area Velocity Explorer (WEAVE; Dalton et al. 2012), and the higher spatial resolution and greater depth of the single IFSs *JWST*/Near InfraRed Spectrograph (NIRSpec; Jakobsen et al. 2022), and in the future the European-Extremely Large Telescope (E-ELT)/High Angular Resolution Monolithic Optical and Near-infrared Integral field spectrograph (HARMONI; Thatte et al. 2010).

Understanding resolved galaxy properties in clusters is important for identifying and quantifying any quenching mechanisms in these galaxies. There have been a number of IFS studies of galaxies in relatively nearby clusters (e.g. Bloom et al. 2017; Cortese et al. 2019; Medling et al. 2018). However, there have been fewer IFS studies of the highest redshift galaxy clusters ($z \sim 1.5$). Some results from the low-z works confirm the correlation between kinematic disturbance and star formation (Bloom et al. 2017), providing evidence for environmental impact on star-formation and morphological quenching (Medling et al. 2018; Schaefer et al. 2017).

A star formation study of low redshift ($z < 0.1$) clusters by Medling et al. (2018) with the Sydney-AAO Multi-object Integral field spectrograph (SAMI) Galaxy Survey (SAMI-GS) focuses on spatially resolved properties of the main-sequence of star formation. By using a threshold of deviation from the main-sequence this work delineates a quenched fraction and shows this is almost constant in over-dense environments regardless of their stellar mass. Therefore, internal processes cannot be the only contributing factors in these galaxies.

At intermediate redshifts, work has been done in the KMOS-Cluster Lensing And Supernova survey with Hubble (K-CLASH) survey to compare galaxies in the field to their counterparts in galaxy clusters (Tiley et al. 2020). K-CLASH focuses on $z \sim 0.2 - 0.6$ and utilises the resolved gas kinematics of these galaxies, with the goal of determining how the highly star-forming field and cluster populations of $z \sim 1 - 3$, transition to their relatively passive modern day counterparts at $z \simeq 0$. They find that their galaxies show similar ranges of morphological and kinematic Hα properties regardless of their environment, however, star-forming cluster galaxies have systematically lower stellar masses than their field counterparts for a given SFR. An expansion of this work in Vaughan et al. (2020) focused on the quenching properties of these clusters versus their field sample. They find that by examining the emission-line properties and metallicities of these galaxies, the most likely quenching mechanisms due to environment are strangulation and ram pressure stripping.

The focus of this chapter is to use resolved Hα emission to determine the gas kinematics of cluster galaxies at $z \sim 1.4$, in order to discover if the turbulence we see in cosmic-noon field galaxies is also observed in clusters at the same epoch. We obtain the galaxy star-formation rates (SFRs) from the Hα emission and compare this with their sizes, masses and morphological properties, determined from near-infrared

(NIR) photometry. These are placed in the context of their phase-space positions within the clusters, to further examine whether proximity to the cluster centre impacts SFR, morphology and/or galaxy kinematics. In addition to this, the two clusters we observe are both very different, with one being a massive, relaxed and mature system for this epoch and the other being very actively star-forming.

3.2 Spectra and imaging

3.2.1 KMOS spectral extraction

In order to generate maps of Hα emission per-spaxel, emission line fitting must be performed. To gain sensible initial parameter values for the per-spaxel fitting, a fit to the 1D spectrum of the whole galaxy was performed. To do this we first fit a 2D Gaussian to an image of the Hα emission, made by summing the wavelength slices of the spectral cube around the Hα line. This provided us with a spatial centroid as a starting point to apply a $2''$ aperture through the cube, which generated a 1D spectrum by summing the flux at each wavelength. The redshift of the galaxy clusters was used to provide a prior on the centre of the Hα line for the fitting routines.

The Hα emission line, at a rest-frame vacuum wavelength of 6564.61 Å, is flanked by a red and blue [NII] emission feature at 6549.86 Å and 6585.27 Å respectively. Due to the atomic transitions that produce the [NII] emission features the flux ratio between them is fixed and as such the red [NII] line is 2.95 times brighter than the blue line (Osterbrock & Shuder 1982). We fit the Hα and [NII] with a sum of three Gaussians in order to to fit these lines cleanly. This is a four parameter fit which utilises the fixed ratio between the emission lines and consists of; Hα central wavelength, Hα flux, Hα line width, and red [NII] flux. We assumed that all three lines come from the same HII regions and so the redshift and line widths off these features should be the same. The fitting routine is a least squares method using the PYTHON package LMFIT (Newville et al. 2014). An example 1D fit can be seen in figure 3.1. A catalogue of known skylines (Rousselot et al. 2000) was used in order to down-weight the fit in the region of the FWHM of the KMOS spectrograph around these lines. Whilst some insights can be gained from analysis of this 1D data, we recognise that the true value of IFU data is

in the spatially resolved picture it can provide when analysed fully to build a 2D view of the kinematics of the targets.

The 1D fit parameters were used to provide initial parameters for the per-spaxel fitting. This proceeds as above with a fit being successful if it reached a S/N threshold of 5 for the Hα emission line in individual spaxels. This S/N is determined by estimating the noise level nearby to the emission lines but with consideration of contribution of skylines, the standard deviation of the mean of these regions was used to find the χ^2 of the total emission over the spectral window of the emission lines and of this window minus the Hα emission line. The square root of the difference of these two χ^2 values was then determined to give our final S/N value. If the S/N threshold was not reached the fitting expands to the surrounding spaxels until the threshold was satisfied or the maximum extent of 7×7 spaxels was reached (equivalent to the seeing disk of $0''.7$ as in Stott et al. 2016). If the fitting conditions were not satisfied the spaxel returns blank. With these maps we assessed the spatial variations in Hα + [NII] emission along with deriving kinematic properties. The result of this extraction was that we are able to recover spatially resolved Hα emission for 24 galaxies out of the 34 targeted across both clusters. These were the galaxies carried forward for the remainder of the analysis.

3.2.2 Imaging data

There is high quality imaging data available for both clusters from *HST*/WFC3 (F160W) and VLT/HAWK-I (K_s), covering all of the galaxies in our KMOS sample, details of which can be found in (Chan et al. 2018). The *HST*/WFC3 data for XMM2235 was obtained in June 2005 (as a part of program GTO-10698), July 2006 (GO-10496), and April 2010 (GO/DD-12051), the data for XMM2215 come from proposal GO-013687 observed in June 2015. HAWK-I data for XMM2235 were taken as part of the first HAWK-I science verification run, 7 in October 2007 (Lidman et al. 2008), whereas for XMM2215 the images were obtained under ESO program ID 084.A-0214(A) in October 2009 (Chan et al. 2018).

The targets for both clusters are displayed in figure 2.6. We preferentially used the higher resolution data from *HST* for our photometry and morphology. However, this was not always possible as the spatial extent of the *HST* imaging data does not cover all of the galaxies in both clusters and there are situations in which the data in F160W was

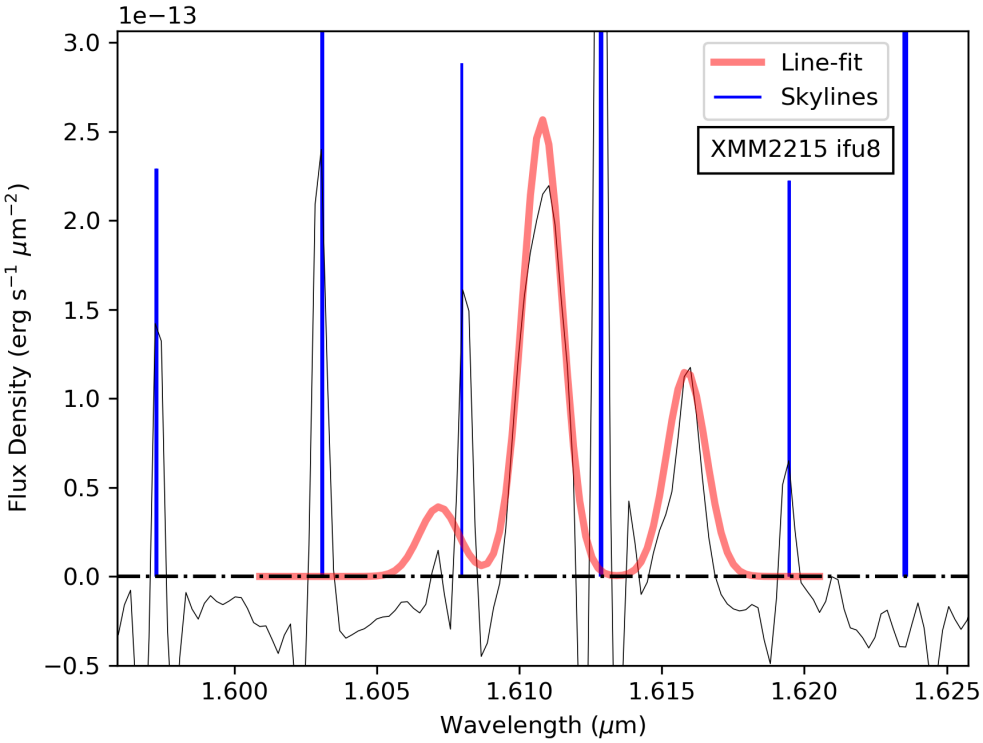

Figure 3.1: An example 1D spectrum centred on the Hα emission line for a single galaxy in XMM2215 (RA: 333.98841 DEC: -17.63140, IFU8). The red curve indicates the simultaneous triple Gaussian fit to the Hα and [NII] emission lines and the blue lines indicate the locations of bright skylines (Rousselot et al. 2000).

poor primarily due to the contamination from stellar diffraction spikes. The galaxies primarily affected by this are located in the bottom right (south west) of figure 2.6 for XMM2235. The PSF FWHM for the *HST* data for XMM2215 and XMM2235 is $0.18''$, and for HAWK-I for XMM2215 and XMM2235 the seeing is $0.42''$ and $0.45''$ respectively. The F160W and K_s photometry was measured from the flux calibrated images with instrumental photometric zero points for each instrument and observation (*HST* - 25.9463 mag and HAWK-I - 30.27 mag for XMM2215 and 30.133 mag for XMM2235), using SExtractor and $2.0''$ diameter apertures for each object.

SExtractor generates a catalogue of sources contained within an image along with a range of parameters of these sources that can be requested by the user including; effective radius, axis-ratio, and a range of methods to determine photometric magnitude. In order to do this it requires information on the photometric zero point, pixel scale and seeing of the images to be catalogued. The user can also alter a detection threshold in order to filter pixels not associated with detected objects.

To compare galaxies with only HAWK-I K_s data to the majority with WFC3 F160W we first calibrated the K_s photometry to the F160W band using galaxies with measurements of both. This was to provide an approximate F160W photometric data-point for these galaxies. This calibration was done by means of a linear fit shown in figure 3.2. We performed two linear fits, one with a fixed 1:1 gradient but free y-intercept and another with a free gradient and intercept.

We used the fixed gradient fit for our final calibration as there was little evidence for a deviation from this. A final calibration of $m_{F160W} = m_{Ks} + (0.31 \pm 0.05)$ was found. This calibration was applied to all K_s band data.

3.3 Analysis and results

In this section, the spatially resolved Hα emission was used to determine the star-formation rates (SFR), velocity maps, rotational velocities, and velocity dispersions of the cluster galaxies. We also derived photometric and morphological properties from the imaging data described above with SExtractor and GALFIT. These galaxy properties were placed into their environmental context within cluster phase space.

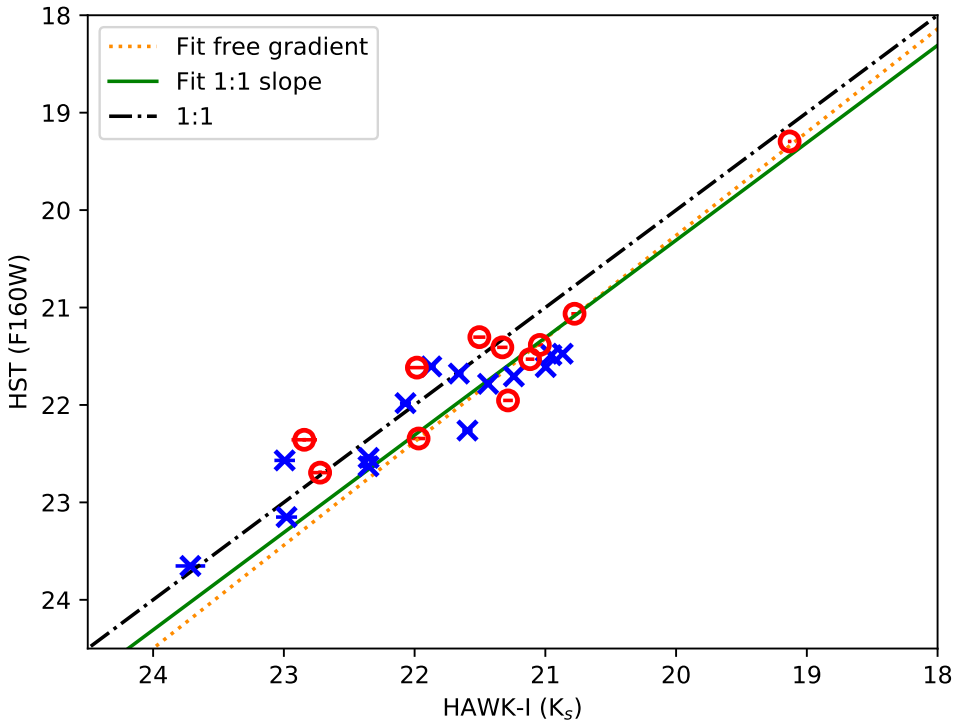

Figure 3.2: Comparison of K_s-band and F160W magnitudes for XMM2215 and XMM2235. The blue crosses indicate the data from XMM2215 and the red circles show the data from XMM2235. The black dot-dashed line shows a 1:1 relationship, the orange dotted line is a linear fit to both datasets and the solid green line shows a linear fit with a fixed 1:1 gradient.

Galaxy redshifts were then used to derive masses for both clusters. Finally, we described witnessing a potential BCG formation event in XMM2215.

3.3.1 Galaxy properties

3.3.1.1 Star formation rates

Star-formation rates for our galaxy sample were calculated using the 1D KMOS spectra (described in section 3.2.1). The SFR was derived from the Hα emission using equation 4.1 from Kennicutt (1998), modified for a Chabrier initial mass function (IMF, Chabrier 2003).

$$\text{SFR} = 4.4 \times 10^{-42} \left(\frac{F_{\text{H}\alpha} 4\pi d_L^2}{10^{\frac{A_{\text{H}\alpha}}{-2.5}}} \right) \tag{3.1}$$

$F_{\text{H}\alpha}$ is the Hα flux, d_L is the luminosity distance to the cluster, and $A_{\text{H}\alpha}$ is extinction. An extinction of $\text{A}_{\text{H}\alpha} = 1$ mag was assumed (Sobral et al. 2012). The SFRs of our galaxies are in the range 8.1 to 70.8 $\text{M}_\odot\text{yr}^{-1}$ with a median value of $<$ SFR $>=$ 27.7 ± 4.6 $\text{M}_\odot\text{yr}^{-1}$.

As mentioned in section 2.4 three targets in our sample are dusty star-forming galaxies, which are submm/IR sources. We therefore calculated that the extinction for these sources should be in the range $\text{A}_\text{v} = 2.5 - 4.0$, as shown in table 3.1. This was calculated by assuming preferentially the $850\mu m$ SFR and where unavailable the $24\mu m$ SFR. These $850\mu m$ and $24\mu m$ SFRs are taken directly from the work by Ma et al. (2015) and Hilton et al. (2010) respectively. For the $850\mu m$ sources Ma et al. (2015) use the method outlined in Swinbank et al. (2013) and perform SED template fitting from the far infrared to the 1.4 GHz band but excluding the $24\mu m$ band to avoid confusion with redshifted polycyclic aromatic hydrocarbon (PAH) features at $z \sim 1.46$. For the $24\mu m$ sources Hilton et al. (2010) estimate infrared luminosity using a range of library templates from Chary & Elbaz (2001) and Dale & Helou (2002). These luminosities are then converted to SFR using the relationship from Kennicutt (1998). The Hα SFR was then uncorrected for extinction and the ratio of these was then taken to correspond to the new $10^{\frac{A_{\text{H}\alpha}}{-2.5}}$. This was then solved for $\text{A}_{\text{H}\alpha}$ and divided by 0.818 to obtain the A_v for the submm and mid-infrared SFR values. Three of these sources

Table 3.1: Global star-formation parameters for cross referenced SMGs. We include data from Hilton et al. (2010), hereafter H10, and Ma et al. (2015), hereafter M15.

Galaxy (Cluster_IFU)	ID (Hilton et al. 2010) (Ma et al. 2015)	SFR $M_\odot$ yr^{-1} (this work, $A_{H\alpha}$)	SFR $(24\mu m)$ (Hilton et al. 2010) $M_\odot$ yr^{-1}	SFR $(850\mu m)$ (Ma et al. 2015) $M_\odot$ yr^{-1}	A_v (mag)
XMM2215_IFU18	744/747 (6)	35.536	140	240	2.82
XMM2215_IFU8	35 (13)	54.836	160	160	2.42
XMM2215_IFU22	53 (-)	16.457	155	–	3.98

are identified as infrared point sources by Hilton et al. (2010) of which two of these are also sub-mm sources from Ma et al. (2015). A further galaxy cross-referenc1ed with an X-ray point-source (PS2) from Hilton et al. (2010). Due to the ambiguity these galaxies introduce to the sample we retained the assumption of $A_v = 1$ and continued to highlight these sources where appropriate in any plots.

During a brief examination of the line-ratios of these galaxies we also identified two of our sample (XMM2215_IFU22 and XMM2235_IFU2) that indicate $\log_{10}([\text{NII}]/\text{H}\alpha) > 0$ with $\log_{10}([\text{NII}]/\text{H}\alpha) = 0.1$ and $\log_{10}([\text{NII}]/\text{H}\alpha) = 0.09$ respectively, which we identified as potential AGN (Baldwin, Phillips & Terlevich 1981; Kauffmann & Haehnelt 2000). One of these two galaxies was also identified as an infrared point source from Hilton et al. (2010) (XMM2215_IFU22), the other is not otherwise associated with these external samples and generally does not display unusual trends within the wider emission line sample from this work. Without more emission line data we cannot be certain about the location of these two sources on the BPT diagram (Baldwin, Phillips & Terlevich 1981). These galaxies are therefore retained in the analysis performed here but are highlighted on the relevant figures where this may have relevance in the interpretation. However, we refer the reader to chapter 4 for further details of additional diagnostics performed for these galaxies.

3.3.1.2 Stellar masses

We infered the stellar masses for our galaxies using the *HST*/WFC3 F160W photometry and the calibration outlined in Stott et al. (2020), using galaxies in the redshift range $z \sim 1.4 - 1.5$, based on the CANDELS survey (Barro et al. 2019), where

$$\log\left(\frac{M}{M_\odot}\right) = (-0.5120 \pm 0.006)\text{m}_{F160W} + (21.62 \pm 0.15) \tag{3.2}$$

The stellar masses of our galaxies are in the range $\log_{10}(\mathrm{M}/\mathrm{M}_{\odot}) = 9.8$ to $11.4\,(\mathrm{M}/\mathrm{M}_{\odot})$ with a median value of $< \log_{10}(\mathrm{M}/\mathrm{M}_{\odot}) >= 10.4 \pm 0.1\,(\mathrm{M}/\mathrm{M}_{\odot})$.

Stellar mass and SFR are plotted in figure 3.3 and compared with the Star-Forming Main-Sequence (SFMS). We plot a SFMS fit (UV+IR/IR) from Speagle et al. (2014), which shows good agreement. We noted that the SFR and stellar masses of our sample occupy same region of parameter space as $z \sim 1.4-1.5$ field galaxies from CANDELS (Barro et al. 2019). This similarity suggests the SFMS of these star-forming cluster galaxies is not strongly affected by the cluster environment. We also included the SFRs derived from submm/IR observations for the dusty star-forming galaxies, as indicated by an additional symbol for each of three relevant galaxies.

3.3.1.3 Galaxy sizes

Here we assessed the sizes of the cluster galaxies using GALFIT. GALFIT enables the fitting of a range of 2-D analytic functions to a range of astronomical sources. Multiple components may be fit by the user to a source where the morphology of said source is complex. By fitting these profiles to a source the user is provided with the best fit parameters of the profiles fit and the final PSF subtracted model, if one is provided. For the galaxies in this sample SEXTRACTOR parameters for magnitude (MAG_AUTO), effective radius (R_e) and axis ratio (b/a) were provided to GALFIT as initial parameter values for a more advanced morphological fitting and correction of the PSF. A 100×100 pixel ($8''.9 \times 8''.9$) cut out *HST*/F160W image centred on each galaxy was provided to GALFIT. We also ran GALFIT on the HAWK-I imaging using equivalent angular sized cut out images. For each GALFIT run a simple sky and single Sérsic model were fit, where appropriate so as to not complicate interpretation of the results. For cut-out images where multiple galaxies were visible, multiple Sérsic profiles were fit in order to remove excess emission from neighbours that could interfere with the fit of the target galaxy. Fitting was performed use a downhill gradient algorithm (Levenberg-Marquardt). The Sérsic profile requires 6 parameters to fit, these are; centroid, total magnitude, effective radius, Sérsic index, axis-ratio, and position angle. The Sérsic profile has the form shown in equation 3.3;

$$\Sigma(r) = \Sigma_e e^{-\kappa[(r/r_e)^{1/n}-1]}, \tag{3.3}$$

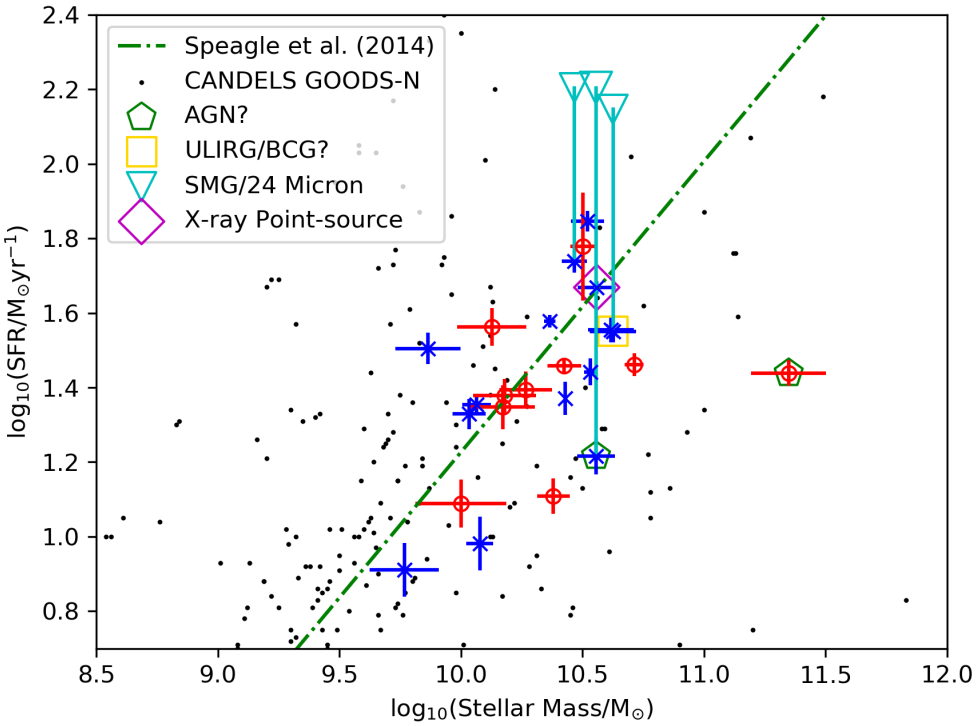

Figure 3.3: Star-formation rate vs stellar mass for both clusters. The blue crosses indicate the cluster XMM2215, red circles XMM2235, and the small black dots indicate data from the CANDELS GOODS-N field from Barro et al. (2019). Green pentagons highlight potential AGN, the gold square indicates the potential BCG of XMM2215 identified as a ULIRG in Hilton et al. (2010). The inverted cyan triangles show the calculated SFRs from Hilton et al. (2010) and Ma et al. (2015) and the magenta diamond shows an X-ray point-source identified from Hilton et al. (2010). The green dot-dashed line shows the $z = 1.4$ SFMS fit performed in Speagle et al. (2014).

where r_e is the effective radius, Σ_e is the surface brightness of the galaxy at r_e, n is Sérsic index, and κ ensures that half of the flux resides within r_e. By using this coupling of κ and n this profile is able to vary between a Gaussian, exponential and de Vaucouleurs. Note that only morphological parameters were taken from our GALFIT catalogue, with the magnitudes taken from the SExtractor MAG_AUTO parameter, which approximates total magnitude (Martini 2001; Stott et al. 2010).

The PSF-removed effective radius was produced via the GALFIT output. Due to the *HST* field-of-view (FOV) not covering all galaxies and the difference in wavelength between WFC3 and HAWK-I we compared our results to verify they were consistent. We find R_e to be generally consistent, as seen in figure 3.4. However, we calibrated the HAWK-I R_e to the WFC3 R_e using a linear fit. This correction was applied to the radii of galaxies with HAWK-I but no WFC3 coverage. The calibration was found to be $Re_{F160W} = (1.48 \pm 0.15) Re_{Ks} - (1.79 \pm 0.53)$. The radii of our galaxies are in the range 1.9 to 5.4 kpc with a median value of $< R_e >= 3.3 \pm 0.2$ kpc.

From our size analysis we compared our sample with the mass-size relation for early- and late-type galaxies (Shen et al. 2003), see figure 3.5. Remembering that our sample targeted star-forming galaxies, we can see that most of our sample are extended galaxies which is consistent with a late-type assumption, however there are some more compact galaxies within the sample.

We also assessed the Sérsic index (n) of our sample, a histogram of which is shown in figure 3.6. As discs can be described as $n = 1$ and ellipticals as $n = 4$ (de Vaucouleurs) we defined an approximate split between these populations at $n = 2$. Using this basic definition we saw that our population is mostly discs (83%), which was expected for a sample targeting the star-forming galaxies of these clusters.

The axis ratios produced by the GALFIT output were converted to galaxy inclination angles using equation 3.4, the same method as Harrison et al. (2017). These inclination angles were used to correct the observed rotational velocities in section 3.3.2.3;

$$\cos^2 \theta_{im} = \frac{(b/a)^2 - q_0^2}{1 - q_0^2}, \tag{3.4}$$

where b/a indicates the axis ratio, θ_{im} is the calculated inclination angle, and q_0 is the intrinsic axial ratio for a galaxy edge-on (Tully & Fisher 1977) and adopted as 0.2 for a thick disc (Harrison et al. 2017). See also figure 3.7 for a histogram of the axis

ratios for the galaxies of each cluster, showing a clear peak in rounder galaxies in our sample.

The X-ray point source in the core of XMM2215 is very round with $(b/a) = 0.992 \pm 0.018$ and so a concern is that this galaxy's morphology is dominated by a central bright AGN. However, the galaxy has a Sérsic index of $n = 4.9 \pm 0.3$, a radius of $R_e = 2.9 \pm 0.2$ kpc, a standard rotation curve (see Appendix) and an $\log([\text{NII}]/\text{H}\alpha)$ line ratio of 0.53 ± 0.04, which puts it in the star-formation region of the BPT diagram (Baldwin, Phillips & Terlevich 1981). In addition, in order to determine if there was poor morphological fitting for the X-ray source or the potential line-ratio AGN (see section 3.3.1.1) we assessed the GALFIT output and verified that the final fit and the residuals did not show any clear point-source behaviour that was problematic for the fitting. Therefore the fits were determined to be reliable and remained in the wider sample but we highlight these points on the relevant figures.

3.3.2 Kinematic modelling

3.3.2.1 Kinematic maps

From the Hα maps we derived velocity maps relative to a galaxies systemic redshift using equation 3.5,

$$\Delta\, z_{spaxel} = \frac{\left(\frac{\lambda_{obs}}{\lambda_{rest}} - 1\right)_{spaxel} - \left(\frac{\lambda_{obs}}{\lambda_{rest}} - 1\right)_{galaxy}}{1 + \left(\frac{\lambda_{obs}}{\lambda_{rest}} - 1\right)_{galaxy}} \tag{3.5}$$

where λ_{obs} is the observed wavelength of Hα in a given spaxel, λ_{rest} is the rest wavelength, and $galaxy$ refers to the systemic redshift of the galaxy from the 1D fit. The velocity of a spaxel is defined as $\Delta\, v_{spaxel} = c\Delta\, z_{spaxel}$.

To aid the analysis of the kinematics we opted to generate a region grown mask to remove excess pixel clumps or single detached pixels from the map by designating the Hα emission centroid as the seed pixel so that the region retained will be the main Hα emission region. We note that such a method would be destructive to data that has patchy emission or close but separate pairs, however from visual inspection this

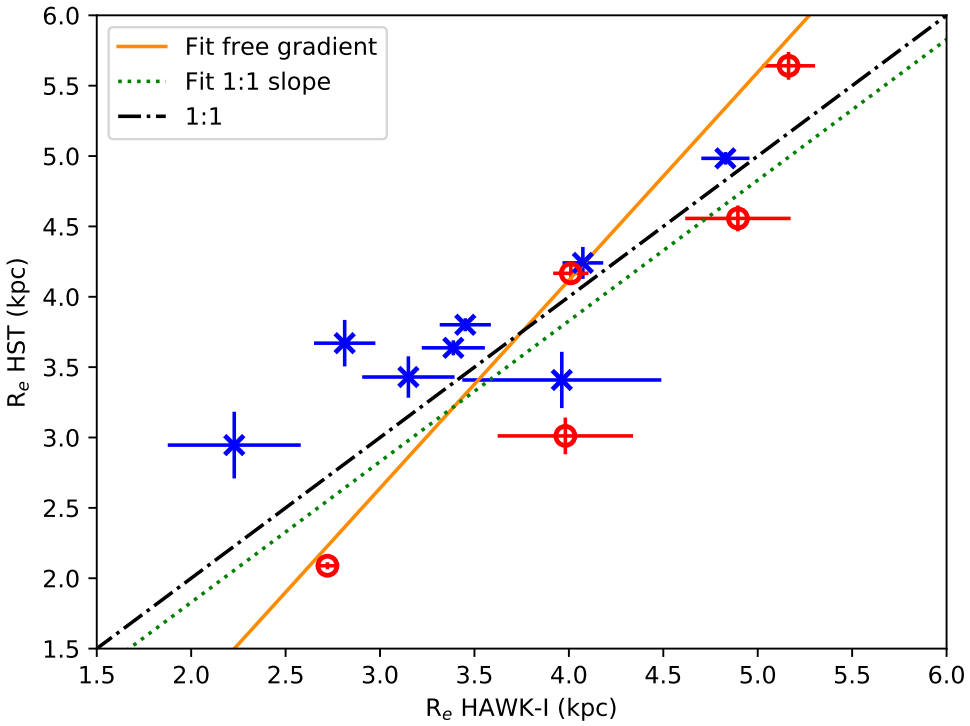

Figure 3.4: Comparison of K-band and F160W R_e for the cluster sample. The blue crosses indicate the data from XMM2215 and the red circles show the data from XMM2235. The black dot-dashed line shows a 1:1 relationship, the solid orange line is a linear fit to both datasets and the dotted green line shows a linear fit with a fixed 1:1 gradient.

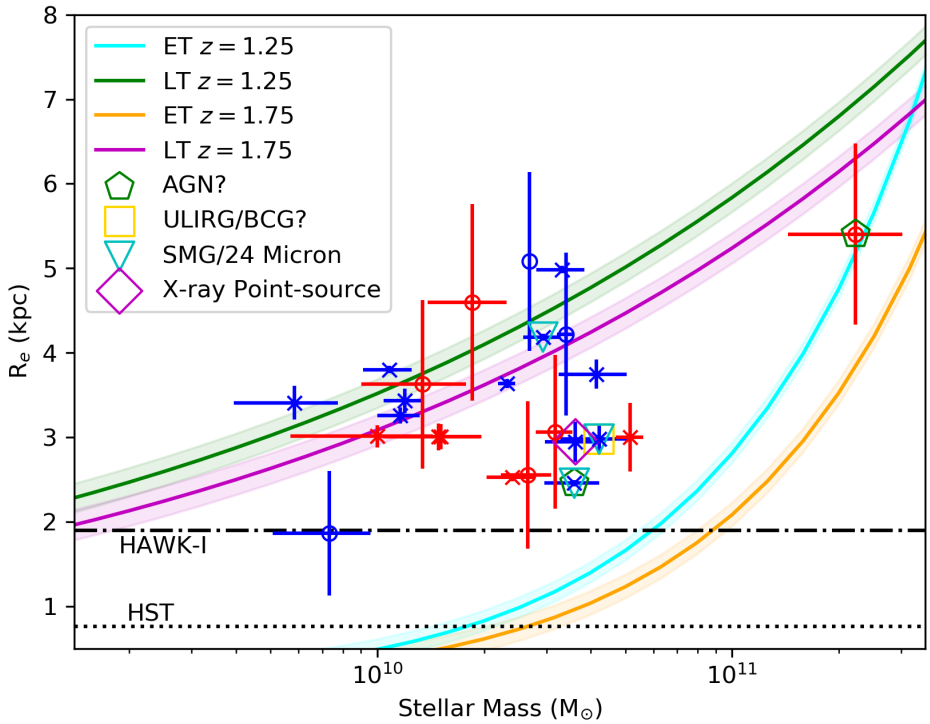

Figure 3.5: Assessment of the mass-size relation (Shen et al. 2003) using the parameters for early- (elliptical passive) and late-type (spiral star-forming) galaxies for the redshift 1.25 and 1.75 bins provided in (van der Wel et al. 2014). The blue markers indicate galaxies in XMM2215 and the red markers are galaxies in XMM2235. The crosses are data from the *HST* subset and circles are from the HAWKI-I subset. The dotted line denotes the PSF limit for the *HST* dataset and the dashed line shows the upper seeing limit for the HAWK-I data. For all other markers we refer the reader to figure 3.3.

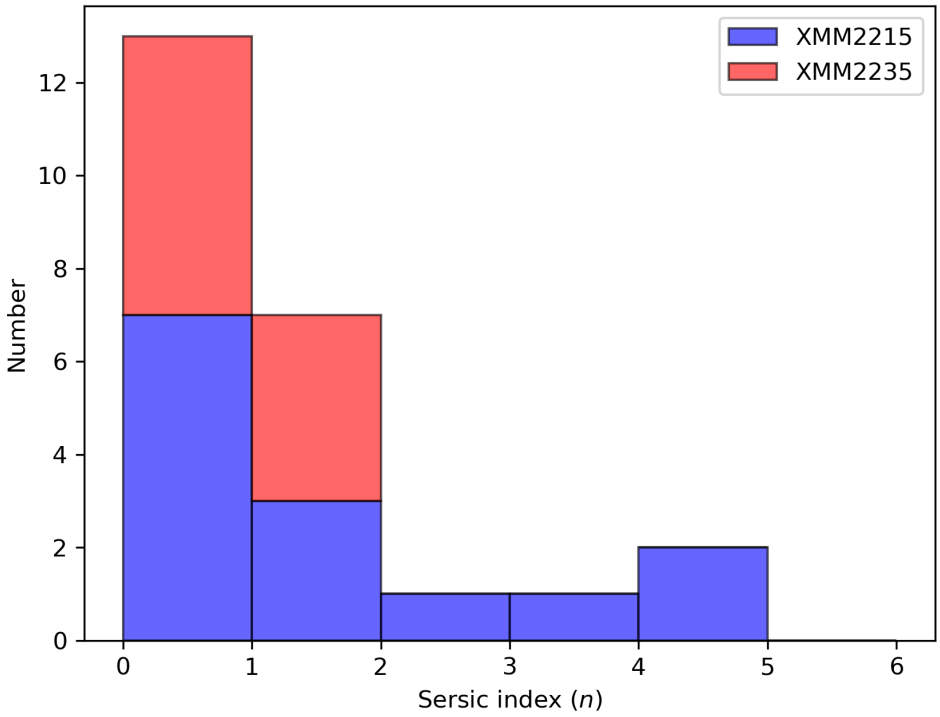

Figure 3.6: Stacked histogram of Sérsic index for our galaxy sample with galaxies from XMM2215 shown in blue and XMM2235 shown in red. Note that the height of each bar shows the cumulative maximum of each bin for the combined sample.

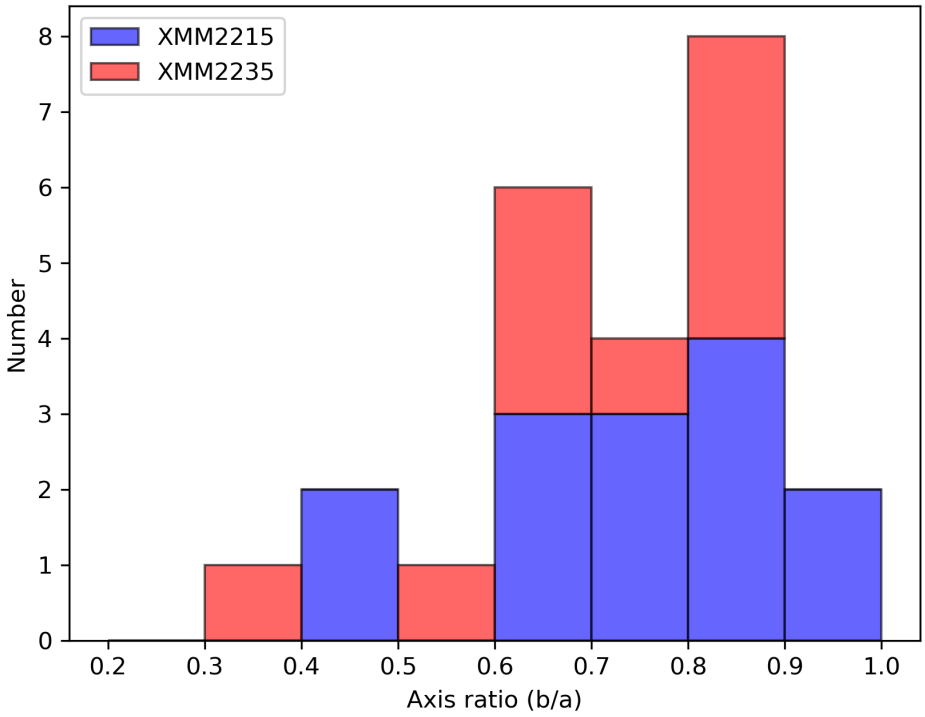

Figure 3.7: Stacked histogram of axis ratios for our galaxy sample, with galaxies from XMM2215 shown in blue and XMM2235 shown in red. Note that the height of each bar shows the cumulative maximum of each bin for the combined sample.

sample did not contain such data. As well as velocity maps, we also generated velocity dispersion maps derived from the width of the Hα line fit (further described in section 3.3.2.5).

3.3.2.2 Kinematic axis

The spatially resolved velocity maps generated in section 3.3.2.1 were first used to derive the kinematic axis of each galaxy. We did this by fitting 1D rotational velocity curves from artificial slits placed on the galaxy centre at systematically different angles. The velocity curves were fit using an analytical model, which takes the form of an arctangent function as shown in equation 3.6 (e.g. Stott et al. 2016).

$$v(r) = \frac{2}{\pi} v_{asym} \arctan(r/r_t) \tag{3.6}$$

where v_{asym} is the asymptotic velocity, r is radius from the galaxy centroid, and r_t is the turnover radius of the velocity curve. v_{asym} here relates to the velocity at the point of plateau in the arctangent profile.

The data to perform this fit was taken from a slit of width $0''.5$ through the Hα centroid of the map. This slit was rotated by 1° intervals with a new fit each time. The data slice extracted from this slit was collapsed into a 1D velocity curve, by taking a median value of each y-axis pixel width, the error on each point was taken as the standard deviation of each column. We performed a rejection on the 1D data that did not have at least 3 pixels of data in each column.

The v_{asym} of each of these fits was plotted against angle and then this was fitted with a sinusoid where the maximum amplitude location in degrees is what we defined as the kinematic axis, as seen in figure 3.8. This approach allowed us to reduce the impact of noise where large anomalous spikes would largely be ignored.

The observed 1D rotation curve for each galaxy was defined as that along the kinematic axis, derived from the method outlined in this section. It is shown along side the kinematic maps in an example shown in figure 3.9. The remaining galaxies can be seen in figures A.1 - A.3 and A.4 - A.5.

We assessed the differences between the kinematic and morphological axes provided by GALFIT, which may be an indicator of galaxy disturbance (Ristea et al. 2022). For a basic comparison we plot the position angle of the kinematic axis (PA_{kin}) with

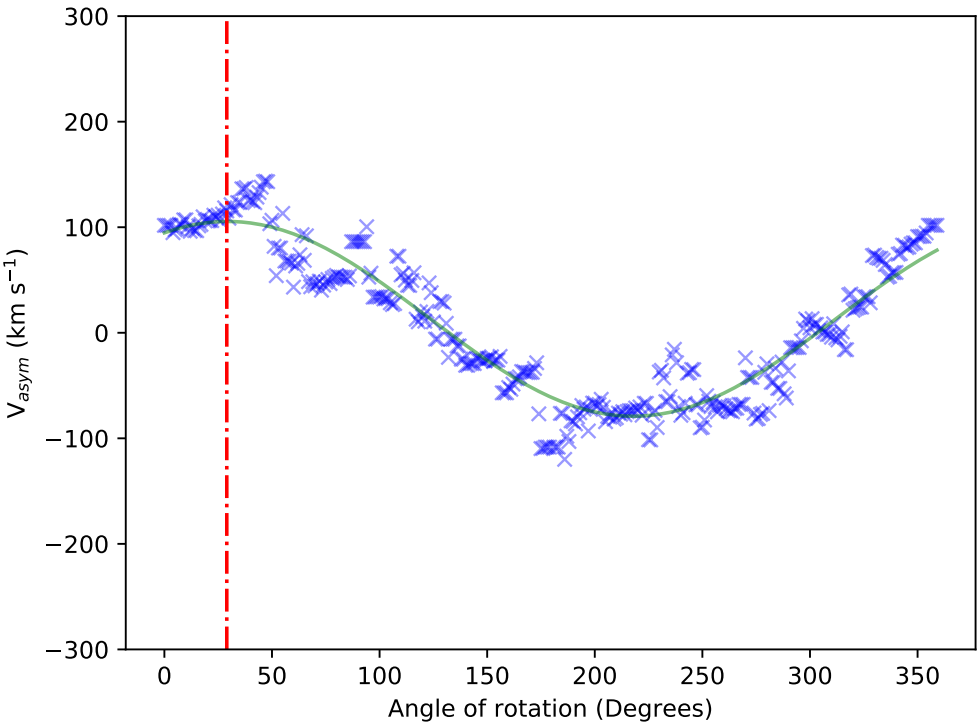

Figure 3.8: An example of the sinusoidal trend in the fitted v_{asym}, derived from equation 3.6, for each potential kinematic axis angle for a single galaxy in XMM2215 (RA: 338.825, DEC: -25.971, IFU11). The green curve shows the sinusoid fit to this, with the red dashed line indicating the angle with the detected maximum v_{asym} and therefore the kinematic axis. Note that the errors on each point have been excluded for ease of viewing but are provided during fitting as described.

morphological axis (PA_{im}), shown in figure 3.10. We noted that the galaxies were generally scattered around the 1:1 line, as expected, but with some outliers. To quantify this, we found that 67% (83%) of PA_{kin} lay within $30°$ ($45°$) of their galaxy's PA_{im}. We also compared the absolute difference between these two position angles, defined by $|\sin(PA_{im} - PA_{kin})|$, and specific star-formation rate (sSFR) in figure 3.11. This showed some correlation (Pearson's $r = 0.47$), such that the more disturbed galaxies with a higher PA offset have a higher sSFR. We explored $|\sin(PA_{im} - PA_{kin})|$ in the larger context of the cluster environment in section 3.3.4.

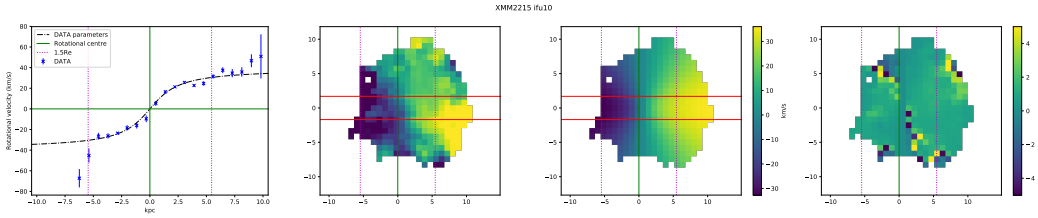

Figure 3.9: Velocity data, derived from equations 3.5 and 3.6, for the galaxy with RA: 333.98827 and DEC: −17.63543 in the cluster XMM2215 observed with IFU10. From left to right the panels are: 1D rotation curve; 2D observed velocity map; model velocity map; and the model velocity map divided by the data.

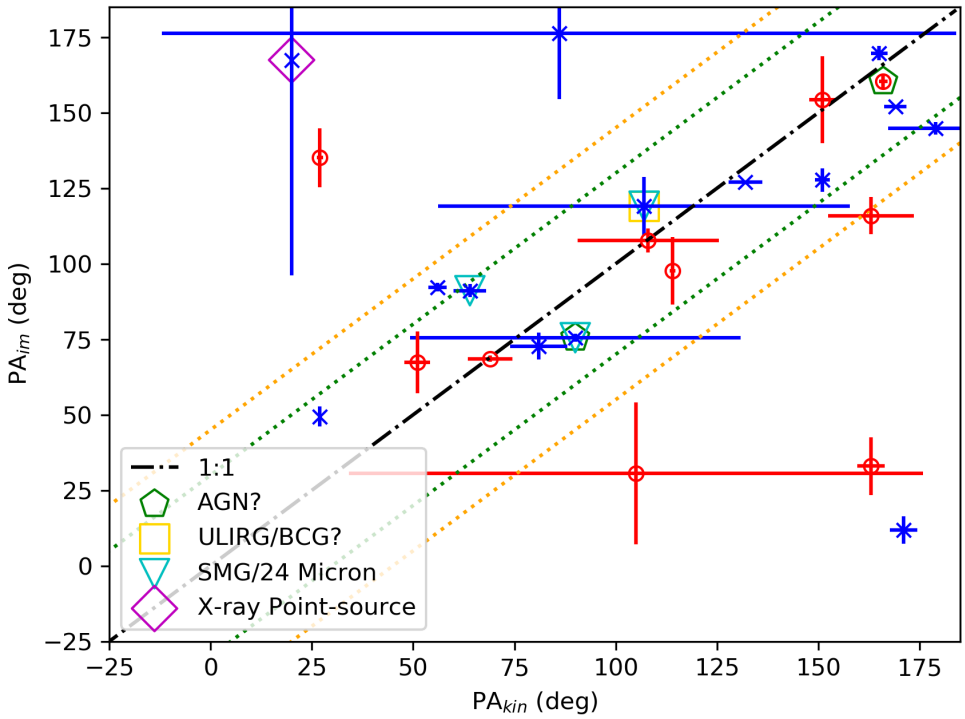

Figure 3.10: Direct comparison between kinematic and morphological axis position-angle. The crosses in blue show the data for XMM2215 and the circles in red show the data for XMM2235. The black 'dot-dashed' line shows a positive 1:1 relationship. 67% (83%) of the kinematic axes lie within 30°, green dotted line, (45°, orange dotted line) of their galaxy's morphological axis. For all other markers we refer the reader to figure 3.3.

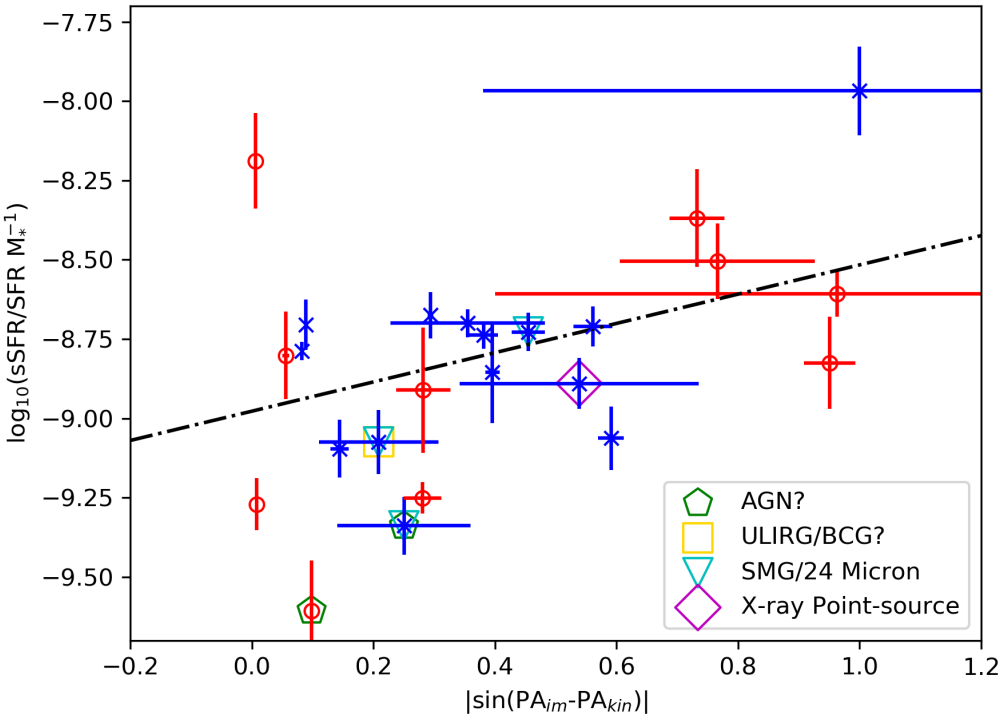

Figure 3.11: Absolute offset between morphological and kinematic axis with sSFR. In both plots the crosses in blue represent data for XMM2215 and the circles in red are for XMM2235. The dashed black line indicates a linear fit. For all other markers we refer the reader to figure 3.3.

3.3.2.3 Velocity map models

In this section the 1D velocity model fitted in section 3.3.2.2 was used to generate a 2D velocity model for quantitative analysis and comparison with the observed velocity maps generated in section 3.3.2.1. These models are shown in figures 3.9, A.1 - A.3 for XMM2215 and figures A.4 - A.5 for XMM2235. This analysis projected a 1D arctangent into a 2D field as would be observed. A crucial step in this process was to take the rotation curve fit results described in section 3.3.2.2 and the inclination angle results from section 3.3.1.3 in order to generate the correct orientation of the model. This map went through a minimisation of the residuals compared to the original map data by systematically stepping through values of v_{asym} at 1 km s^{-1} intervals, until a final best 2D model was found.

3.3.2.4 Rotation velocity

The rotation velocities for those galaxies with resolved kinematics were calculated by following a similar extraction method as when building the initial 1D rotation curve but this time with the derived 2D velocity model map and taking the velocity at 1.5R$_e$ from the rotation centre. We used 1.5R$_e$ to easily compare between galaxies and we found that the rotation curve is generally flattened (or flattening) here as demonstrated in the 1D rotation curves in the left panel of figure 3.9 and figures A.1 to A.5. The rotation velocities of our galaxies are in the range 5.0 to 467.5 km s^{-1} with a median value of $< v >= 124.3 \pm 23.8$ km s^{-1}.

We compared these velocities to stellar mass, shown in figure 3.12, as expected there is a positive correlation between these two values. A linear fit gives $\log_{10}(v_{1.5}) = (0.74 \pm 0.29)\log_{10}(m_*) - (5.65 \pm 3.08)$.

3.3.2.5 Velocity dispersion

The velocity dispersion was calculated from the Hα emission using the form shown in equation 3.7;

$$\sigma = \left(\frac{v_{wid}}{2.35} \frac{1}{v_{cen}} \right) c, \tag{3.7}$$

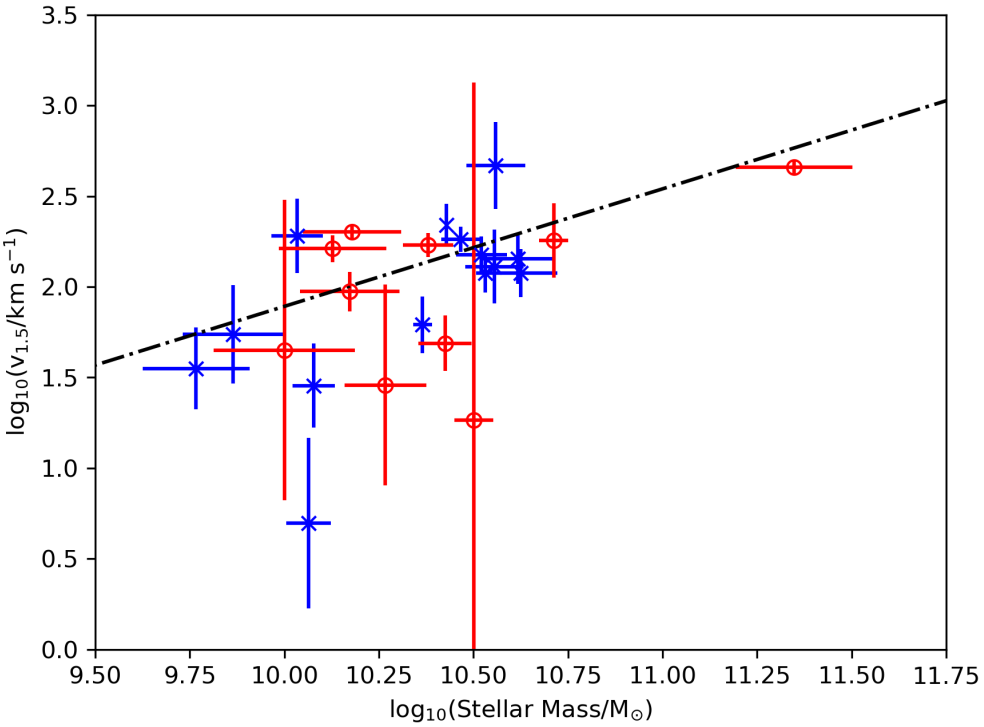

Figure 3.12: The velocity at $1.5R_e$ plotted against stellar mass. The crosses in blue represent data for XMM2215 and the circles in red are for XMM2235. The dot dashed black line represents a linear fit and demonstrates the positive correlation between rotational velocity and stellar mass.

where v_{wid} is the emission line width, v_{cen} is the line centroid, and c is the speed of light in km s^{-1}.

The velocity dispersion was extracted from the Hα maps and we attempted to mitigate the effect of beam smearing in this analysis. Beam smearing broadens the velocity via a combination of a gradient in velocity and limited spatial resolution due to seeing. The effect is greatest where there is the greatest change in velocity (typically in the core of our galaxies). We therefore decided to remove the width of the seeing disc ($0''.7$) in a strip about the centre of each galaxy, orthogonal to PA$_{kin}$. This reduced the effect of beam smearing by removing the region with the greatest change of velocity with radius. The observed velocity dispersion of the galaxy was taken as a median of this cleaned velocity dispersion map with the KMOS instrumental velocity resolution removed in quadrature. The velocity dispersions of our galaxies are in the range 11.1 to 95.6 km s^{-1} with a median value of $< \sigma >= 44.9 \pm 5.4$ km s^{-1}. We expect velocity dispersion to be higher in a denser environment such as a galaxy cluster compared to the field environment as discussed in section 3.4.1.2 due to the more complex gravitational well these galaxies are present in causing a higher likelihood of disturbance and interaction. We plot velocity dispersion against stellar mass in figure 3.13, but found no strong correlation. We note that no correlation was found with either SFR or sSFR.

3.3.3 Rotation or dispersion dominated galaxies

In order to determine if the galaxies are rotation- or dispersion-dominated we followed the same simple definition of Stott et al. (2016) with rotation-dominated $v_{1.5}/\sigma > 1$ and dispersion-dominated $v_{1.5}/\sigma < 1$. The $v_{1.5}/\sigma$ of our galaxies are in the range 0.3 to 7.0 with a median value of $< v_{1.5}/\sigma >= 2.6 \pm 0.4$, these values indicate that $v_{1.5}/\sigma$ is lower in our sample compared to the local values ($5 - 20$, Epinat et al. 2010) and agrees with those in the field at similar redshift (Förster Schreiber et al. 2009; Stott et al. 2016). We therefore concluded they are as turbulent as their field counterparts at this epoch. We found that using this threshold $(v_{1.5}/\sigma < 1)$ four of our galaxy sample, spread equally across the two clusters, were dispersion-dominated, constituting $17\% \pm 9$ of the sample. The remainder (83%) were rotation-dominated as expected for star-forming galaxies.

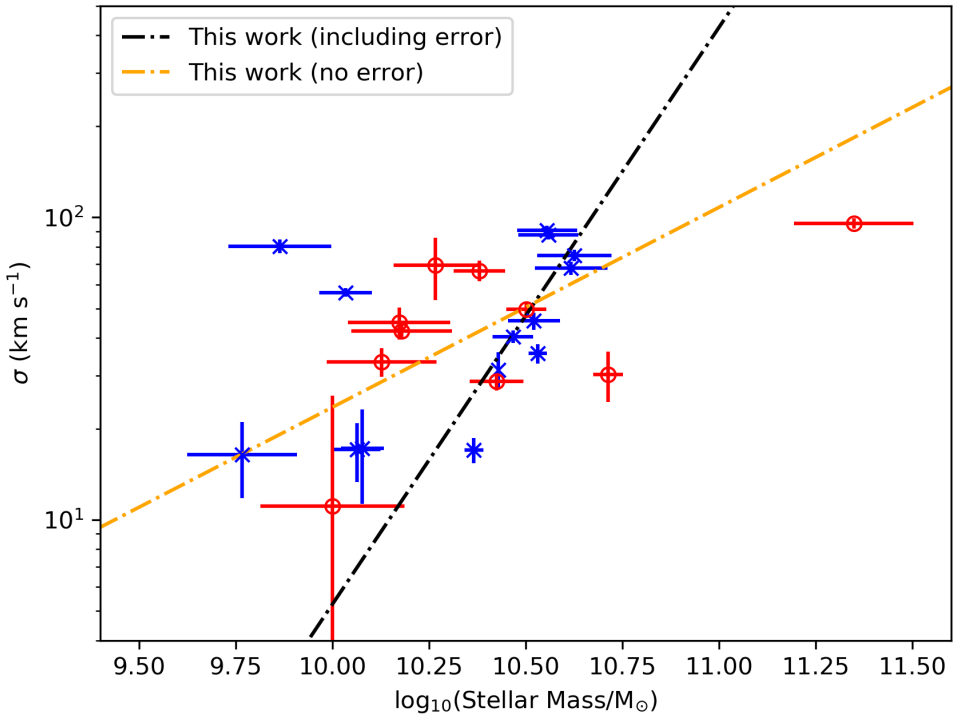

Figure 3.13: Velocity dispersion plotted against Stellar mass. The crosses in blue represent data for XMM2215 and the circles in red are for XMM2235. The black line indicates a linear fit accounting for errors on the data whereas the orange line is a linear fit without errors included.

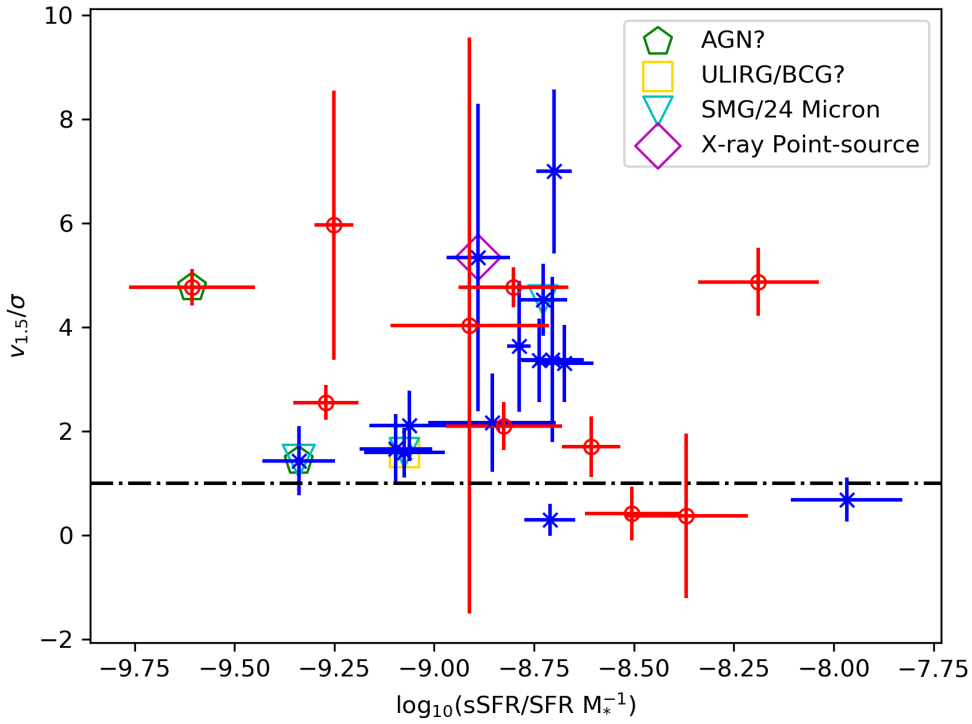

Figure 3.14: v/σ plotted against sSFR. The crosses in blue represent data for XMM2215 and the circles in red are for XMM2235. The dashed black line indicates the rotation- to dispersion-dominated threshold. For all other markers we refer the reader to figure 3.3.

We assessed the relationship between dispersion- or rotation-dominated systems and other parameters. No correlation was seen with stellar mass or SFR, however in figure 3.14 we found that the dispersion-dominated galaxies had some of the highest sSFRs in our sample, $\log_{10}(\text{sSFR yr}^{-1}) > -8.8$. Because of this, we found that the dispersion-dominated galaxies also sat above the SFMS. Similarly, the dispersion-dominated galaxies all had a large offset between these kinematic and morphological axes $|\sin(\text{PA}_{im} - \text{PA}_{kin})|$ (> 0.55). We found an average $|\sin(\text{PA}_{im} - \text{PA}_{kin})| = 0.28 \pm 0.06$ for the rotation-dominated sample and 0.75 ± 0.07 for the dispersion-dominated sample. We note that our dispersion-dominated sample consists of four galaxies, two per cluster. This indicates that kinematic disturbance is responsible for the misalignment of axes rather than fitting difficulties. This is further evidence that more disturbed systems drive enhanced star-formation.

3.3.3.1 Total masses

We used the kinematics to determine the total mass of our galaxies within $1.5R_e$. The majority of our sample are rotation dominated and so we use the formula

$$M_{dyn}(r < r_{1.5}) = \frac{v_{1.5}^2 r_{1.5}}{G}, \tag{3.8}$$

to determine the total mass (as used by e.g. (Stott et al. 2016)), where $r_{1.5}$ and $v_{1.5}$ are defined as $1.5R_e$ from the rotational centre and G is the gravitational constant.

For galaxies that are dispersion dominated we used the virial theorem;

$$M_{dyn}(r < r_{1.5}) = \frac{\alpha\sigma_0^2 r_{1.5}}{G}, \tag{3.9}$$

where α here is fixed to provide the same stellar mass to dynamical mass ratio for the dispersion-dominated galaxies as for the rotation-dominated galaxies and was found to be 1.53 ± 0.78.

We compared these total masses with stellar mass, in figure 3.15. The majority of our sample have a higher dynamical mass than stellar mass, as expected, with a median stellar mass to dynamical mass of 84% at $1.5R_e$. We note that three galaxies have a $> 2\sigma$ excess in stellar mass compared with dynamical mass.

3.3.4 Galaxy property dependencies on the cluster environment

Cluster galaxies are not evolving in isolation and therefore it is important to assess their properties alongside their location within the cluster environment itself. For this we performed a cluster phase space analysis.

In order to determine where the galaxies are located within the cluster environment we need to determine the cluster centre. In the case of our clusters we can choose either the X-ray emission centroid or the location of the BCG. The locations of these can be seen in figure 2.6. We decided that the cluster centre was better described by the X-ray emission for XMM2215 as there is no obvious BCG (Stott et al. 2010, see sections 5.4 and 5.5) and by the location of the BCG for XMM2235, as it appears to be in the centre of a dense core of passive galaxies (Chan et al. 2018).

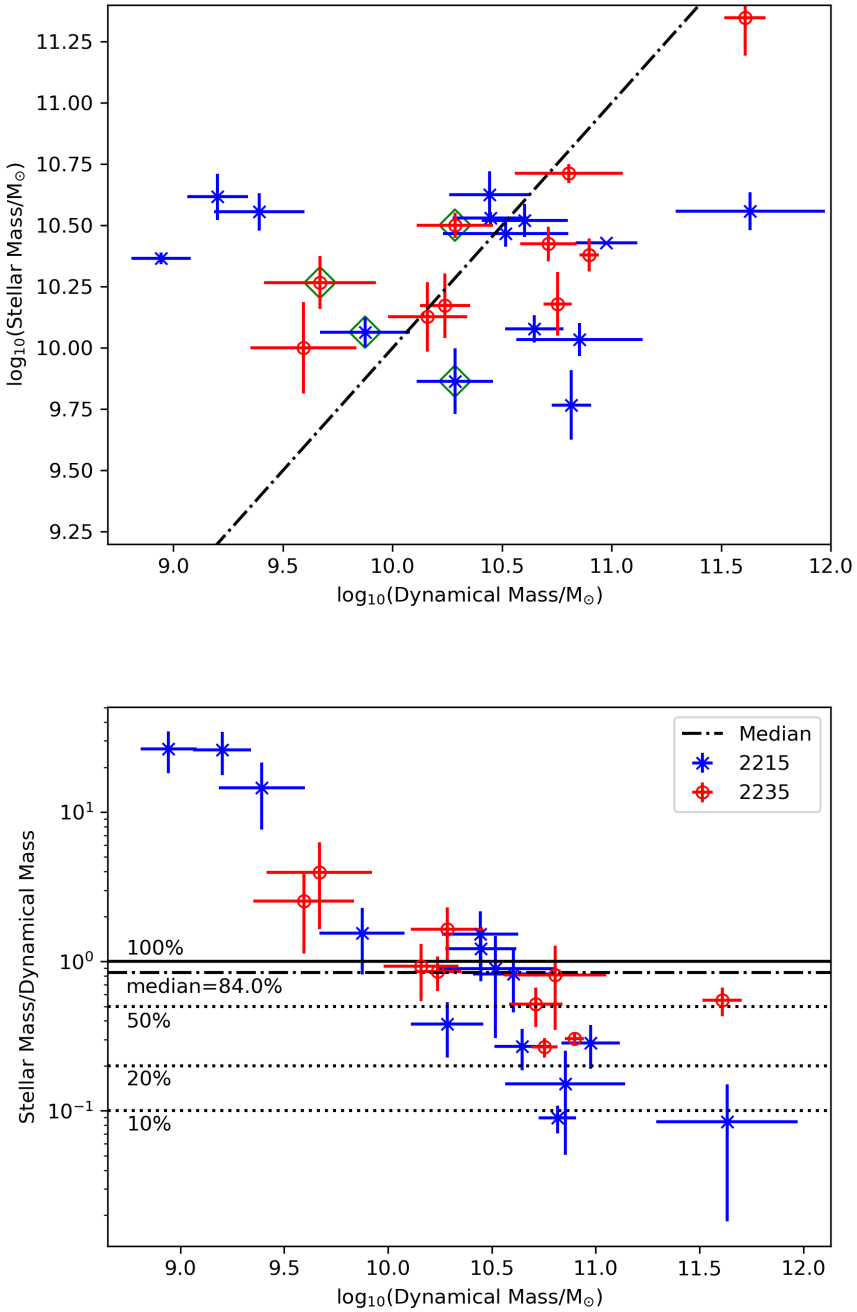

Figure 3.15: *top*: Stellar mass plotted against Dynamical mass within $1.5R_e$. The 'X' points in blue represent data for XMM2215 and the 'O' points in red are for XMM2235. 1:1 line shown as the black dot dashed line. The dispersion dominated galaxies are highlighted with green diamonds. *bottom*: Ratio of stellar mass to dynamical mass plotted against dynamical mass. Included are lines of one to one ratio, 10, 20, 50 per cent mass, and the sample median.

The average cluster redshift was determined by comparing the distribution of galaxy redshift for each cluster, this is shown in figure 3.16. For a more accurate determination of the average z, this included the redshifts of the passive galaxies presented in Chan et al. (2018) which was then clipped by 2σ to remove further outliers that may be present in the sample. As these redshift distributions are narrow and include the wider cluster population we used a mean to determine the cluster redshifts for a more accurate average of the sample. The redshfits of the emission line sample presented in this work are located in table 3.2. The dominant sources of errors contributing to these refined redshifts would be the inclusion of interlopers in the sample, primarily removed by using only spectroscopically confirmed members of the cluster, and poor fitting of the Hα emission line centroid, also minimised by visual inspection of the final 1D fitting used and applying S/N limits to the galaxies carried forward in the analysis of this work previously described. This sample serves to update current cluster redshifts as follows: 1.3930 ± 0.0006 for XMM2235 and 1.4570 ± 0.0002 for XMM2215.

In order to determine the phase-space location of each galaxy within the cluster environment, we followed the methodology outlined in Noble et al. (2013). The parametrisation of the environment, Γ, is shown in equation 3.10

$$\Gamma = \frac{r}{r_{200}} \times \frac{\Delta v_{gal}}{\sigma_c}, \tag{3.10}$$

where distance (r) from the cluster centre is normalised by r_{200} and Δv_{gal} is the relative line-of-sight velocity for each galaxy to the cluster redshift normalised by the velocity dispersion of the cluster σ_c. This allows us to assess each galaxy in a consistent phase-space of the cluster. We can define lines of constant phase-space to highlight regions of cluster environment. For these constants we followed those described in Noble et al. (2013) for the virialised, backsplash, and infall regions. Any galaxy below $\Gamma = 0.1$ was defined as being in the virialised core of the cluster, between 0.1 and 0.4 as the backsplash region and galaxies with $\Gamma \geq 0.4$ were infalling. The backsplash region contains those galaxies that have already completed an initial pass of the cluster core and also those that are approaching the core for the first time.

The phase-space location for each galaxy, including passive galaxies from KCS II (Chan et al. 2018), is shown in figure 3.17. This shows that, at least for our selection, the passive galaxies in XMM2235 live almost exclusively in the core, whereas for

XMM2215, they are more scattered throughout phase-space. This reinforces the picture that XMM2235 is a more mature and dynamically relaxed cluster than XMM2215. We also see that this method of delineating these cluster regions is imperfect due to the overlap of galaxies defined as 'infall' and 'backsplash'. Backsplash galaxies can be seen as those galaxies completing orbit of the cluster core they settle and virialise. However, infall galaxies are those that are commencing their first pass of the cluster core. Due to this overlap it is not possible using this method to distinguish how many orbits a galaxy has completed and therefore to be sure that infall galaxies are not backsplash and vice versa. This limitation is also noted in the work of Noble et al. (2013). We therefore limit our discussion to those galaxies that are identified as being in the virialised core of the clusters and those that are not.

In order to investigate the impact of cluster environment on these galaxies we include colour bars, representing galaxy properties, on the phase-space diagrams (e.g. figure 3.17), these properties include; SFR, ΔMS, $v_{1.5}/\sigma$, axis-ratio, R_e, $v_{1.5}$, σ, Sérsic index, sSFR, and $|\sin(PA_{im} - PA_{kin})|$. To further aid interpretation, we also include plots that collapse the phase-space information into a single axis so we can see multiple galaxy properties in their environmental context. We note that the majority of our star-forming galaxy properties appear to have no preferred region of phase-space, including; $v_{1.5}/\sigma$, R_e, $v_{1.5}$, σ, Sérsic index, sSFR, and $|\sin(PA_{im} - PA_{kin})|$.

To understand environmental quenching, we assessed the effect of cluster environment on star formation. The phase space diagram for SFR is shown in figure 3.18. Galaxies with the highest SFR in XMM2215 were found to live in the core of the cluster with the $\log_{10}(\mathrm{SFR}/[\mathrm{M}_\odot\,\mathrm{yr}^{-1}])$ range of 1.35 to 1.85 with a median value of $< \log_{10}(\mathrm{SFR}/[\mathrm{M}_\odot\,\mathrm{yr}^{-1}]) >= 1.63 \pm 0.15$, this is further reinforced when we look at a radially averaged vector plot of SFR shown in figure 3.19. As noted above, there is no clear trend with sSFR as the galaxies with the highest SFR are also more massive. Although, we note that the three galaxies in our sample with the highest sSFRs ($\log_{10}(\mathrm{sSFR}\,\mathrm{yr}^{-1}) > -8.5$) are all outside of the cluster cores, perhaps indicating the core region is having some quenching effect. However, a further indicator of star formation activity is the galaxy position relative to the SFMS. In figure 3.20 we show that the core galaxies of XMM2215 lie above the main sequence relative to the rest of the sample. We found no significant correlation between regions for the combined sample. However, when we assessed XMM2215 alone, we found $< \Delta\mathrm{MS} >= 0.071 \pm 0.047$

in the core region and -0.177 ± 0.083 in the backsplash region, a difference of 1.6σ although depending on definition of the core boundary using a radially averaged vector approach, shown in figure 3.21, we did not see this conclusion. This potentially illustrates the benefit of combining kinematic and positional data to determine the cluster region rather than positional data alone. The above results again demonstrate the active nature of XMM2215 compared with XMM2235.

We found a potential link between cluster region and galaxy axis-ratio within XMM2235, which can be seen in figures 3.22 and 3.23 such that the axis ratio (b/a) appears to be higher on average in the cluster core. We found a $(b/a) = 0.87 \pm 0.06$ in the core region and 0.70 ± 0.05 in the backsplash region of XMM2235, a difference of 2σ, however more data would be required to determine its significance. The galaxies in the core, which are potentially most processed by the cluster, are therefore found to be the most round. By plotting the axis-ratio with a radially average vector from the cluster centre we can see a similar picture but also that the galaxies in XMM2215 seem to fall within two groupings with those closest to the cluster core being the roundest and slowly becoming more elongate towards Mpc h^{-1} and then becoming more scattered beyond this boundary. This adds weight to the above argument of a falloff of rounder galaxies further from the cluster core. By comparing this to sSFR, also in figure 3.23, we can see that galaxies with the higher axis ratios in the core have very typical sSFRs for the sample. Up to this point we have assumed that axis ratio is a proxy for inclination angle but this may instead be an indication of morphological transformation preceding the cessation in star formation (we discuss this further in section 3.4). This could also be an indicator of the more evolved nature of XMM2235 when compared with XMM2215.

When making the same comparison with stellar mass in XMM2235 we found the same significance with galaxies in the core having a lower stellar mass than those outside. We found a median value of $< \log_{10}(\text{Stellar Mass}/\text{M}_\odot) >= 10.18 \pm 0.06$ in the core compared to $< \log_{10}(\text{Stellar Mass}/\text{M}_\odot) >= 10.61 \pm 0.18$ in the backsplash region. This may be an indicator of downsizing in the core, with star-formation taking place in progressively lower mass galaxies with time (Cowie 1996).

Table 3.2: The coordinates and calculated redshifts of the KCS emission-line sample for XMM2215 and XMM2235.

Galaxy (Cluster_IFU)	z	RA (^{o})	DEC (^{o})
XMM2215_ifu2	1.46342	333.99476	−17.62791
XMM2215_ifu4	1.45827	333.98917	−17.61767
XMM2215_ifu5	1.45504	333.98396	−17.61043
XMM2215_ifu6	1.45177	333.99042	−17.62929
XMM2215_ifu8	1.45377	333.98841	−17.63140
XMM2215_ifu10	1.45150	333.98827	−17.63543
XMM2215_ifu11	1.46065	333.97046	−17.65213
XMM2215_ifu14	1.45277	333.99522	−17.63600
XMM2215_ifu16	1.45843	333.99780	−17.64366
XMM2215_ifu18	1.46699	333.99872	−17.63297
XMM2215_ifu20	1.46100	334.01069	−17.63223
XMM2215_ifu22	1.45181	334.00161	−17.63065
XMM2215_ifu23	1.45887	334.03100	−17.62364
XMM2215_ifu24	1.45363	334.00041	−17.62604
XMM2235_ifu1	1.35936	338.86513	−25.92886
XMM2235_ifu2	1.38974	338.84116	−25.92744
XMM2235_ifu4	1.38981	338.83525	−25.93228
XMM2235_ifu11	1.40033	338.82462	−25.97074
XMM2235_ifu12	1.38210	338.82532	−25.96843
XMM2235_ifu14	1.41163	338.82903	−25.96796
XMM2235_ifu16	1.38154	338.83768	−25.96747
XMM2235_ifu17	1.39712	338.84275	−25.95680
XMM2235_ifu18	1.39900	338.84087	−25.95383
XMM2235_ifu22	1.39222	338.85753	−25.92764

Table 3.3: Kinematic and mass parameters of the resolved sample.

Galaxy (Cluster_IFU)	v/σ	σ (km s^{-1})	$\log_{10}$(Stellar mass/M$_\odot$)	SFR (M$_\odot$ yr^{-1})	$\log_{10}$(sSFR)/SFR M$_\odot^{-1}$)
XMM2215_ifu2	1.7 ± 0.7	17.2 ± 5.9	10.08 ± 0.06	9.6 ± 1.6	-9.10 ± 0.09
XMM2215_ifu4	3.3 ± 0.7	45.5 ± 3.0	10.52 ± 0.07	70.2 ± 4.4	-8.67 ± 0.07
XMM2215_ifu5	0.7 ± 0.4	80.2 ± 4.2	9.86 ± 0.13	32.0 ± 3.1	-7.97 ± 0.14
XMM2215_ifu6	2.1 ± 0.7	68.0 ± 3.4	10.62 ± 0.09	35.9 ± 2.7	-9.06 ± 0.10
XMM2215_ifu8	4.5 ± 0.7	40.4 ± 1.9	10.47 ± 0.05	54.8 ± 3.9	-8.73 ± 0.06
XMM2215_ifu10	3.6 ± 1.3	17.0 ± 1.6	10.37 ± 0.02	37.8 ± 1.5	-8.79 ± 0.03
XMM2215_ifu11	3.4 ± 0.8	35.5 ± 2.6	10.53 ± 0.02	27.7 ± 2.3	-8.74 ± 0.04
XMM2215_ifu14	5.3 ± 3.0	87.5 ± 3.0	10.56 ± 0.08	46.6 ± 1.8	-8.89 ± 0.08
XMM2215_ifu16	0.3 ± 0.3	17.1 ± 3.8	10.06 ± 0.06	22.6 ± 1.2	-8.71 ± 0.06
XMM2215_ifu18	1.6 ± 0.5	74.9 ± 3.3	10.63 ± 0.10	35.5 ± 2.4	-9.07 ± 0.10
XMM2215_ifu20	3.4 ± 1.6	56.5 ± 1.9	10.03 ± 0.07	21.3 ± 2.0	-8.70 ± 0.08
XMM2215_ifu22	1.4 ± 0.7	90.6 ± 3.4	10.56 ± 0.08	16.5 ± 1.9	-9.34 ± 0.09
XMM2215_ifu23	7.0 ± 1.6	31.4 ± 4.4	10.43 ± 0.0003	23.5 ± 2.4	-8.70 ± 0.04
XMM2215_ifu24	2.2 ± 0.9	16.4 ± 4.6	9.77 ± 0.14	8.2 ± 1.4	-8.86 ± 0.16
XMM2235_ifu1	4.9 ± 0.7	33.3 ± 3.6	10.13 ± 0.14	36.5 ± 4.3	-8.19 ± 0.15
XMM2235_ifu2	4.8 ± 0.4	95.6 ± 3.9	11.35 ± 0.15	27.5 ± 2.2	-9.61 ± 0.16
XMM2235_ifu4	1.7 ± 0.6	28.7 ± 1.9	10.42 ± 0.07	28.8 ± 1.4	-8.61 ± 0.07
XMM2235_ifu11	2.1 ± 0.5	44.9 ± 5.5	10.17 ± 0.13	22.2 ± 3.1	-8.83 ± 0.15
XMM2235_ifu12	6.0 ± 2.6	30.3 ± 5.7	10.71 ± 0.04	28.9 ± 2.0	-9.25 ± 0.05
XMM2235_ifu14	0.4 ± 1.6	49.7 ± 2.3	10.50 ± 0.05	60.0 ± 20.1	-8.37 ± 0.15
XMM2235_ifu16	4.0 ± 5.5	11.1 ± 14.7	10.00 ± 0.19	12.3 ± 1.8	-8.91 ± 0.20
XMM2235_ifu17	2.6 ± 0.3	66.7 ± 5.3	10.38 ± 0.07	12.8 ± 1.4	-9.27 ± 0.08
XMM2235_ifu18	4.8 ± 0.4	42.1 ± 2.0	10.18 ± 0.13	23.9 ± 2.5	-8.80 ± 0.14
XMM2235_ifu22	0.4 ± 0.5	69.5 ± 16.2	10.27 ± 0.11	24.8 ± 2.8	-8.50 ± 0.12

Table 3.4: Morphological parameters of the sample.

Galaxy (Cluster_IFU)	R_e (k pc)	Sérsic index (n)	Axis ratio (b/a)	Morphological PA (^{o})	Kinematic PA (^{o})
XMM2215_ifu2	3.4 ± 0.1	1.1 ± 0.1	0.8 ± 0.02	72.7 ± 4.4	81.0 ± 7.0
XMM2215_ifu4	5.0 ± 0.04	0.5 ± 0.01	0.4 ± 0.004	151.9 ± 0.4	169.0 ± 2.8
XMM2215_ifu5	1.9 ± 0.7	0.6 ± 0.1	0.9 ± 0.1	176.2 ± 21.8	86.0 ± 98.1
XMM2215_ifu6	3.7 ± 0.2	2.2 ± 0.1	0.6 ± 0.01	92.2 ± 1.5	56.0 ± 2.2
XMM2215_ifu8	4.2 ± 0.04	0.9 ± 0.01	0.9 ± 0.01	91.1 ± 2.2	64.0 ± 4.0
XMM2215_ifu10	3.6 ± 0.1	1.6 ± 0.02	0.9 ± 0.01	169.7 ± 2.4	165.0 ± 2.0
XMM2215_ifu11	4.2 ± 1.0	0.6 ± 0.03	0.6 ± 0.1	49.4 ± 3.3	27.0 ± 0.4
XMM2215_ifu14	2.9 ± 0.2	4.9 ± 0.3	1.0 ± 0.02	167.4 ± 71.2	20.0 ± 0.5
XMM2215_ifu16	3.3 ± 0.1	4.0 ± 0.8	0.6 ± 0.01	144.9 ± 2.1	179.0 ± 11.8
XMM2215_ifu18	3.0 ± 0.2	0.7 ± 0.1	0.8 ± 0.03	119.0 ± 9.6	107.0 ± 50.8
XMM2215_ifu20	3.8 ± 0.05	0.7 ± 0.02	0.5 ± 0.005	126.9 ± 0.6	132.0 ± 4.1
XMM2215_ifu22	2.5 ± 0.04	3.0 ± 0.05	0.8 ± 0.01	75.5 ± 1.3	90.0 ± 40.8
XMM2215_ifu23	5.1 ± 1.1	0.7 ± 0.03	0.7 ± 0.1	11.8 ± 4.5	171.0 ± 3.4
XMM2215_ifu24	3.4 ± 0.2	2.0 ± 0.1	0.8 ± 0.02	127.7 ± 3.8	151.0 ± 1.9
XMM2235_ifu1	3.6 ± 1.0	0.7 ± 0.1	0.4 ± 0.1	107.7 ± 4.0	108.0 ± 17.4
XMM2235_ifu2	5.4 ± 1.1	1.5 ± 0.03	0.7 ± 0.1	160.4 ± 2.3	166.0 ± 1.0
XMM2235_ifu4	2.6 ± 0.9	0.6 ± 0.1	0.9 ± 0.2	30.6 ± 23.5	105.0 ± 70.8
XMM2235_ifu11	3.0 ± 0.2	1.3 ± 0.1	0.9 ± 0.03	135.1 ± 9.7	27.0 ± 0.8
XMM2235_ifu12	3.0 ± 0.4	0.7 ± 0.2	0.7 ± 0.1	97.7 ± 11.2	114.0 ± 0.7
XMM2235_ifu14	3.1 ± 0.9	0.9 ± 0.1	0.6 ± 0.1	115.9 ± 6.1	163.0 ± 10.6
XMM2235_ifu16	3.0 ± 0.1	1.2 ± 0.1	0.9 ± 0.03	67.4 ± 10.3	51.0 ± 3.1
XMM2235_ifu17	2.5 ± 0.05	0.9 ± 0.03	0.6 ± 0.01	68.6 ± 1.0	69.0 ± 5.5
XMM2235_ifu18	3.0 ± 0.2	1.1 ± 0.1	0.9 ± 0.03	154.2 ± 14.4	151.0 ± 3.3
XMM2235_ifu22	4.6 ± 1.2	0.9 ± 0.1	0.7 ± 0.1	33.0 ± 9.6	163.0 ± 3.4

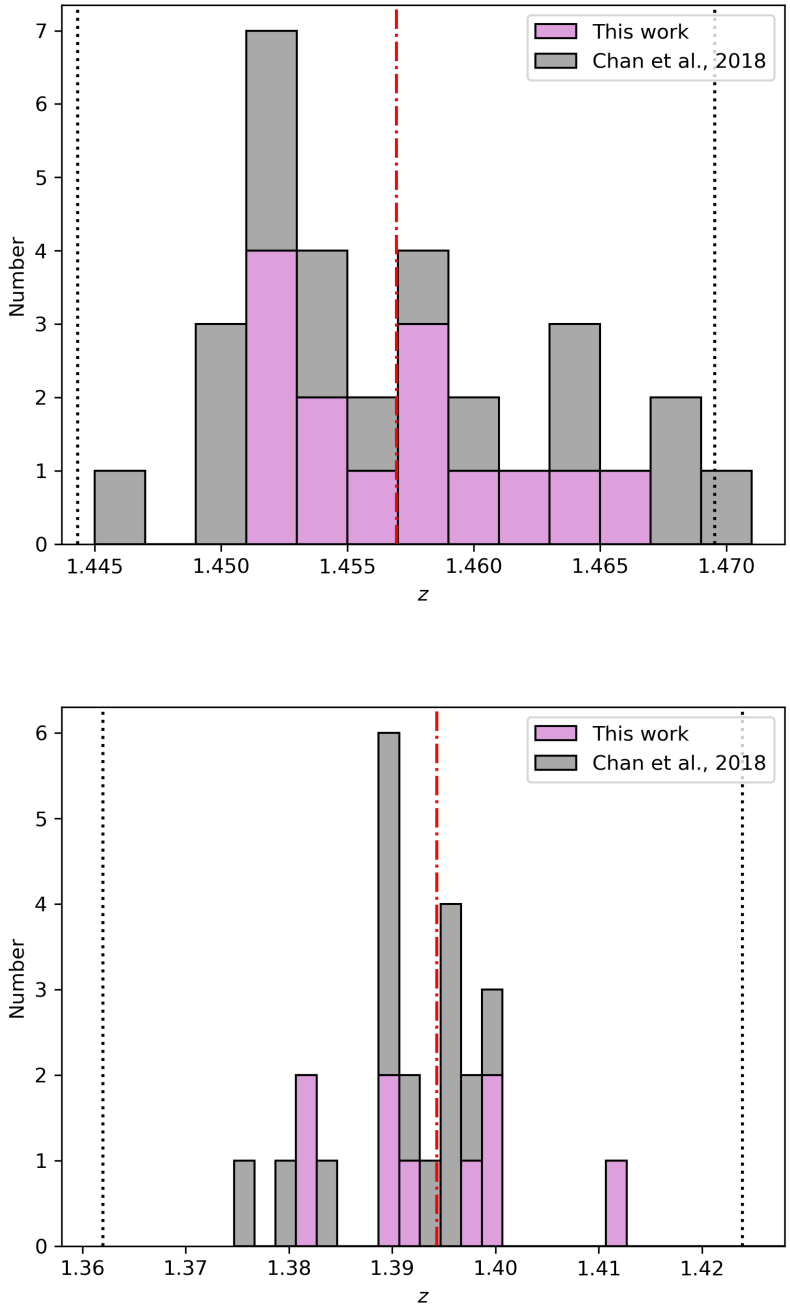

Figure 3.16: *top*: Distribution of redshift for cluster galaxies in XMM2215. Bars in purple are redshift values calculated from this work and those in grey are values for the passive galaxies from Chan et al. 2018. The red dashed line indicates the mean redshift and the upper and lower black dotted lines indicate 2 standard deviations from the mean. *bottom*: Distribution of redshift for cluster galaxies in XMM2235, with the colour bars defined as above.

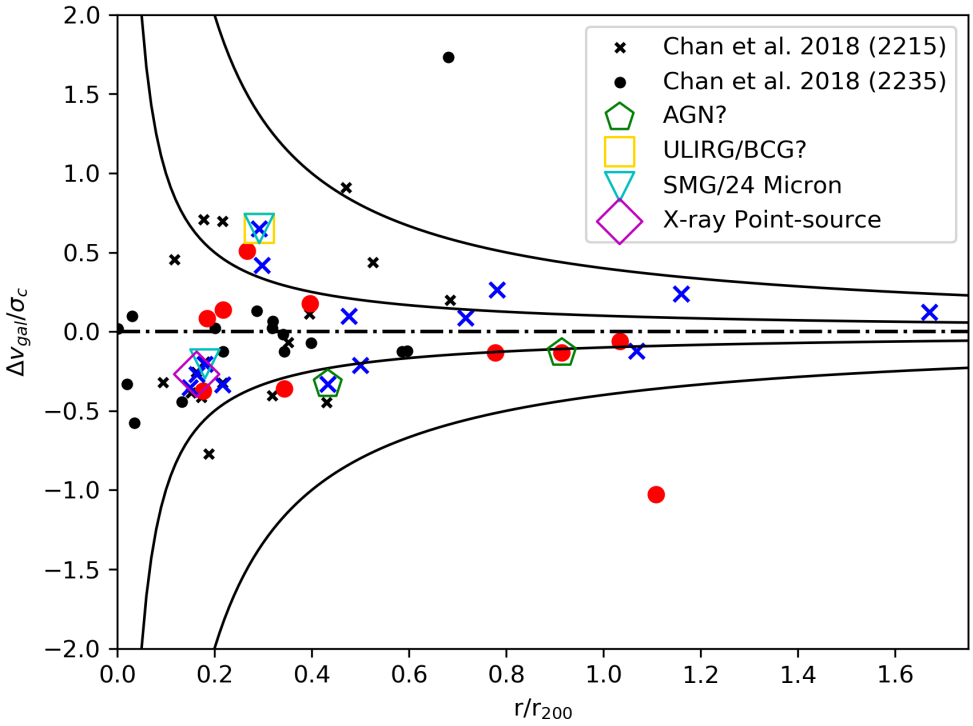

Figure 3.17: A cluster phase-space plot of relative galaxy line-of-sight velocity normalised by cluster velocity dispersion against galaxy distance from cluster centre normalised by r_{200}. The blue crosses indicate those galaxies in XMM2215 from this work and the red circles indicate those within XMM2235 from this work. All black points indicate passive galaxies from Chan et al. (2018). The black curves represent lines of constant Γ, the inner line is $\Gamma = 0.1$ and represents the boundary of the cluster virialised core, the outer line $\Gamma = 0.4$ and represents the outer boundary of the cluster. Galaxies between these two curves are defined as backsplash galaxies and those beyond $\Gamma = 0.4$ are approaching infall. We note the core location of the passive galaxies in XMM2235 demonstrates its mature dynamics compared with XMM2215. For all other markers we refer the reader to figure 3.3.

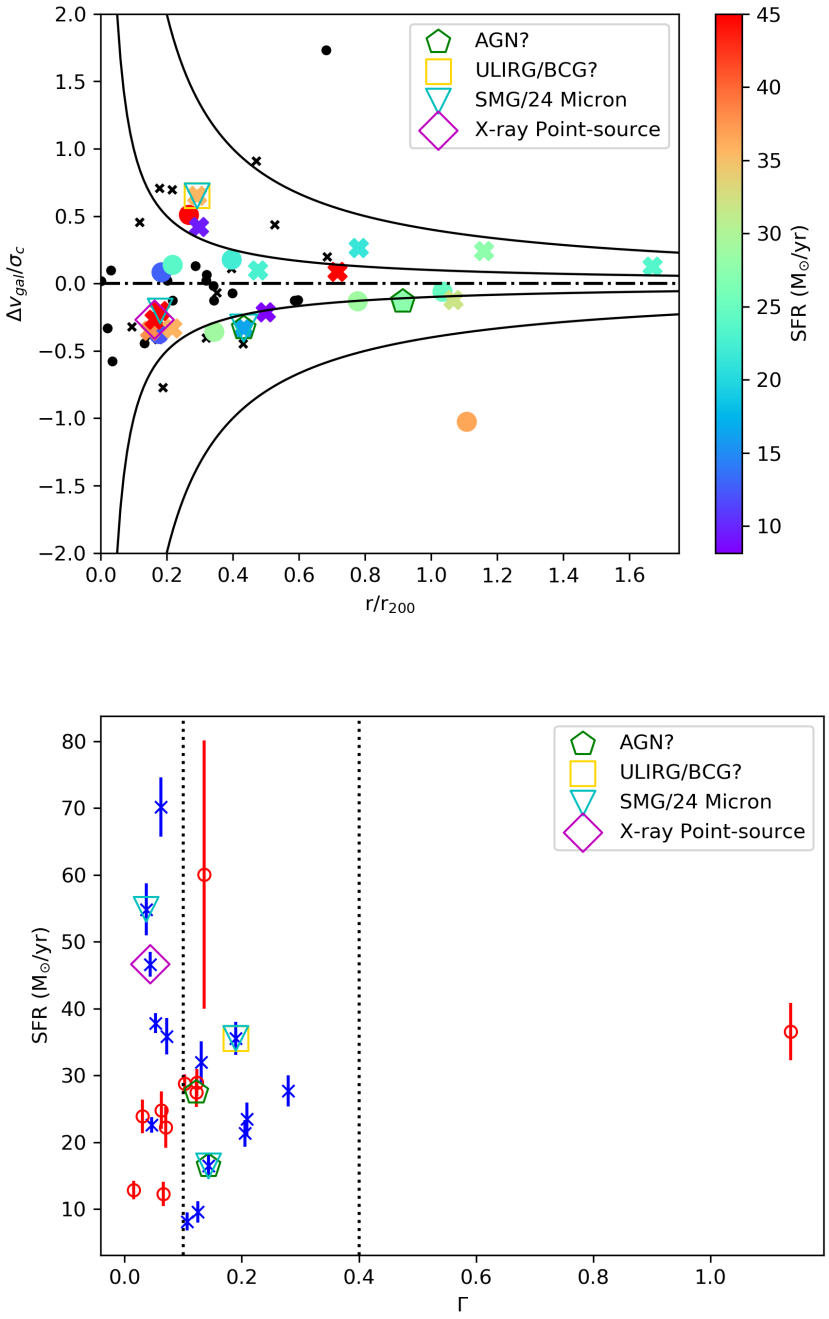

Figure 3.18: *top*: Cluster phase-space diagram, the colour-space indicates SFR. The crosses indicate those galaxies in XMM2215 from this work and the circles indicate those within XMM2235 from this work. All black points indicate passive galaxies from Chan et al. (2018). The solid black curves represent lines of constant Γ, as described in figure 3.17 caption. In colour space we plot the SFR for each galaxy within their respective clusters. *bottom*: Collapsed cluster phase-space with SFR. For all other markers we refer the reader to figure 3.3.

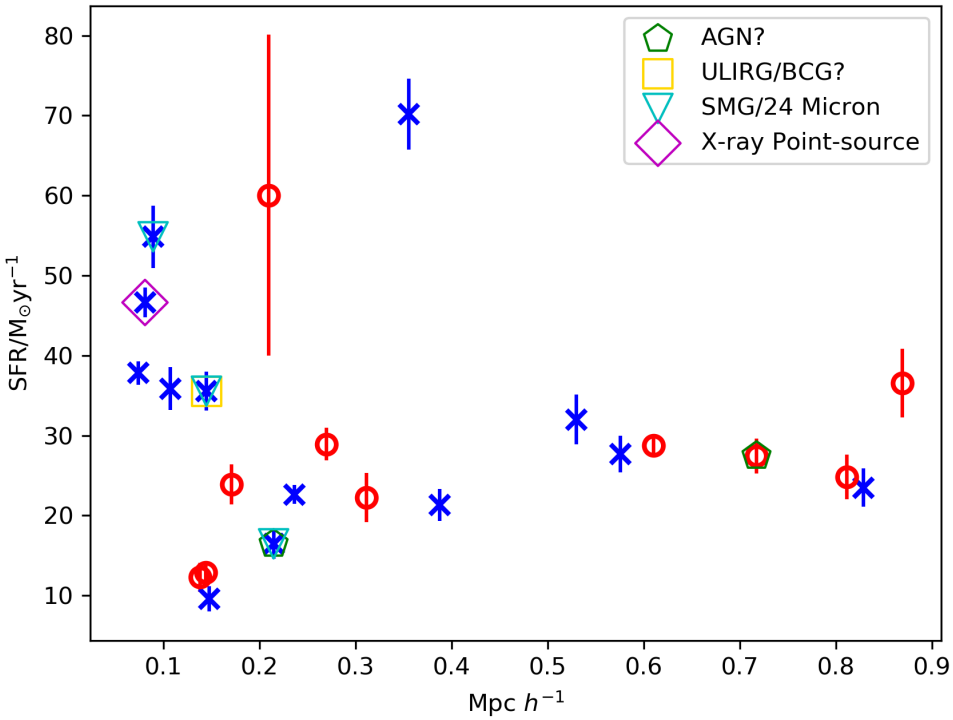

Figure 3.19: Radially averaged vector from cluster centroid of each galaxy in our sample with SFR. The galaxies for XMM2215 are indicated with the blue crosses and the galaxies from XMM2235 are shown with the red circles.

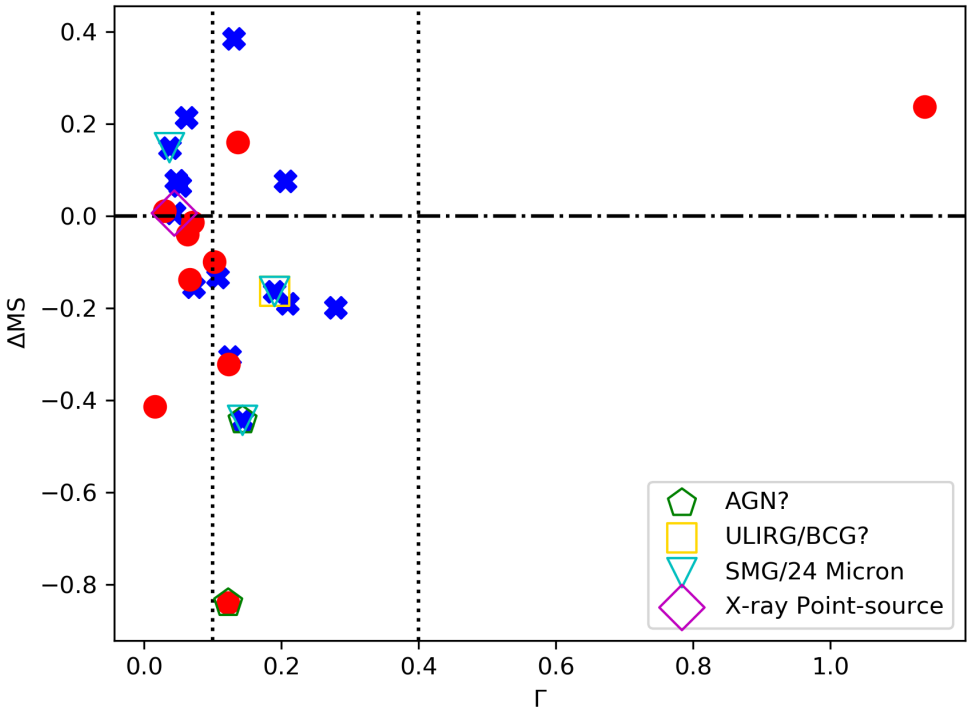

Figure 3.20: The deviation from SFMS (Speagle et al. 2014) plotted against a 1D representation of phase-space Γ (equation 3.10). The crosses indicate those galaxies in XMM2215 from this work and the circles indicate those within XMM2235 from this work. The vertical dotted lines represent lines of constant Γ, as described in figure 3.17 caption. For all other markers we refer the reader to figure 3.3.

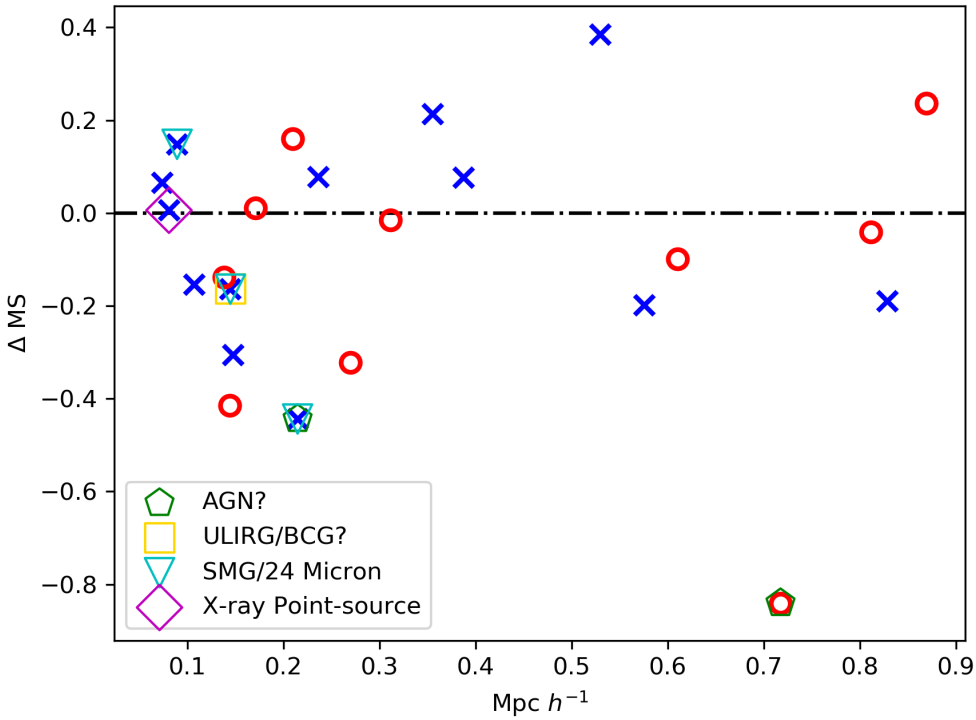

Figure 3.21: Radially averaged vector from cluster centroid of each galaxy in our sample with deviation from the SFMS. The galaxies for XMM2215 are indicated with the blue crosses and the galaxies from XMM2235 are shown with the red circles. The black dot-dashed line indicates the zero line.

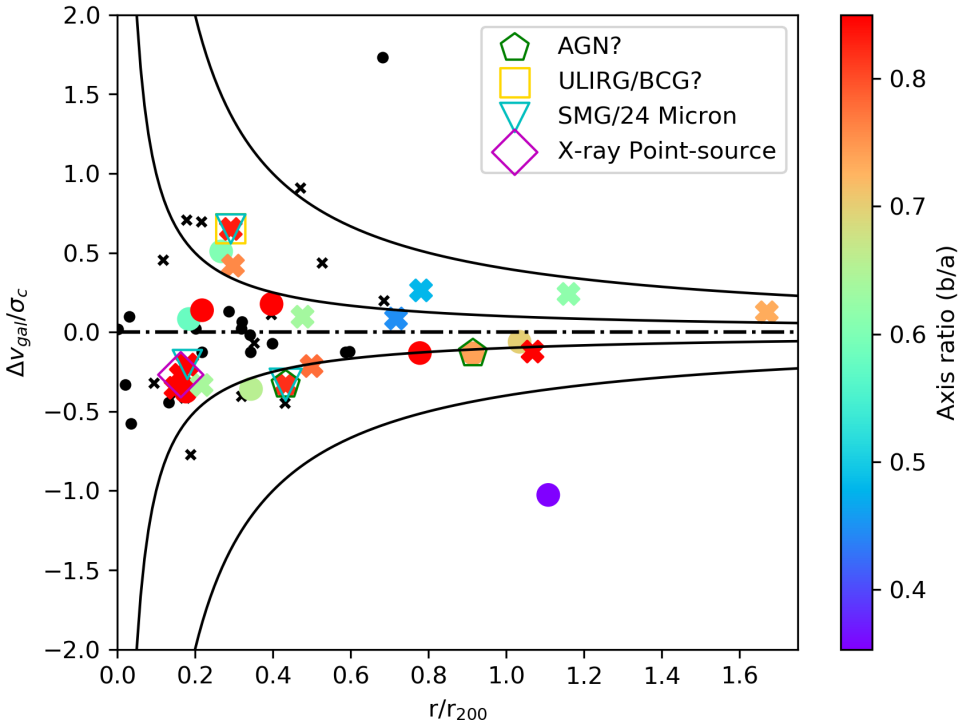

Figure 3.22: Cluster phase space diagram. The crosses indicate those galaxies in XMM2215 from this work and the circles indicate those within XMM2235 from this work. All black points indicate passive galaxies from Chan et al. (2018). The solid black curves represent lines of constant Γ, as described in figure 3.17 caption. In colour space we plot the axis ratio for each galaxy within their respective clusters.

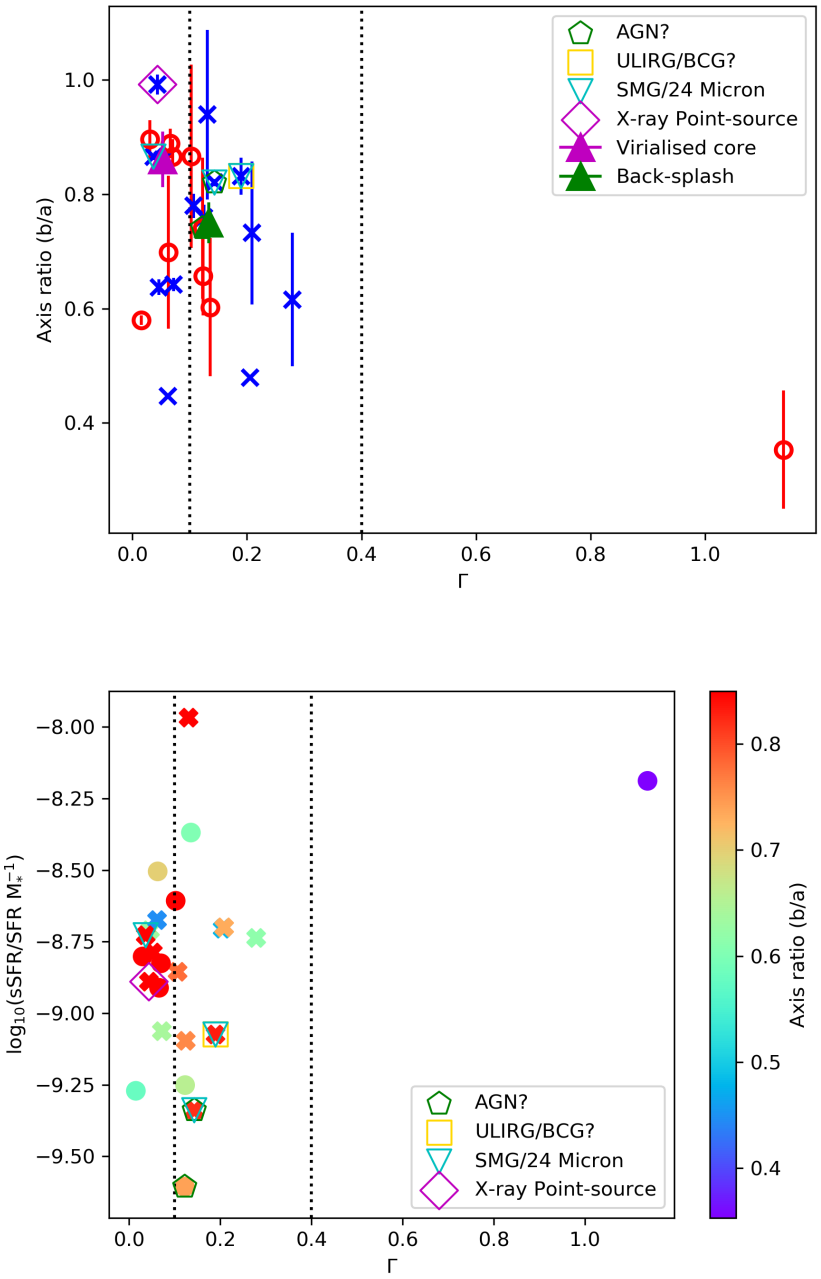

Figure 3.23: *top*: Galaxy axis-ratio plotted against a 1D representation of phase-space, Γ. The blue crosses indicate those galaxies in XMM2215 and the red circles indicate those within XMM2235. The black dotted lines represent constant Γ, as described in figure 3.17 caption. Median values for each region and the overall sample are also plotted as triangles where; magenta is the virialised core and green is backsplash. *bottom*: Cluster phase space with sSFR and axis-ratio plotted in colour-space. The blue crosses indicate those galaxies in XMM2215 and the red circles indicate those within XMM2235. The black dotted lines represent constant Γ, as described in figure 3.17 caption. For all other markers we refer the reader to figure 3.3.

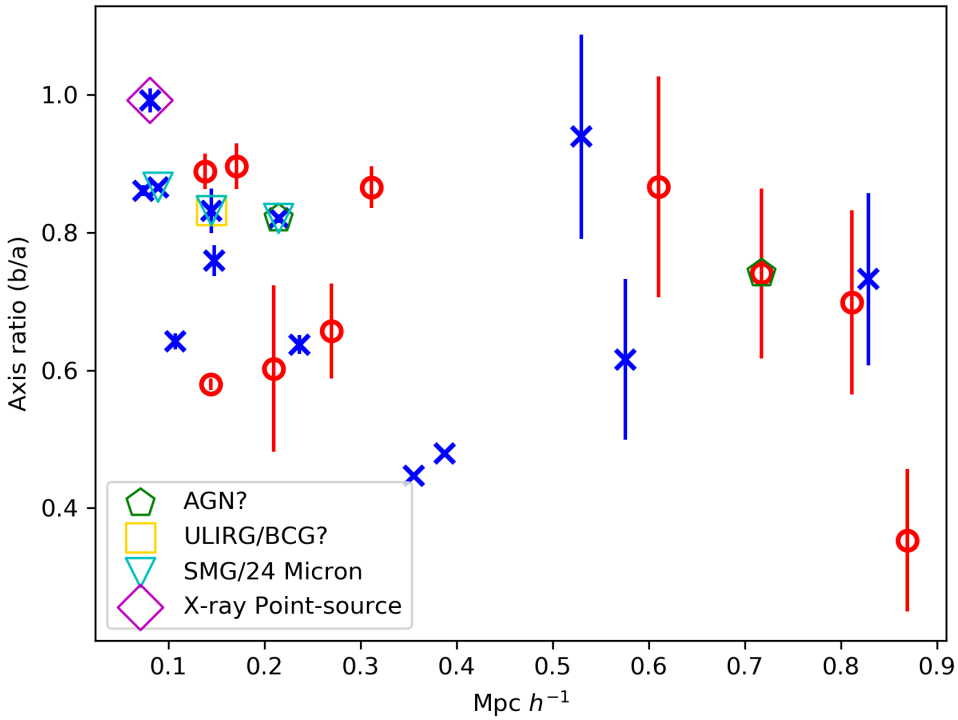

Figure 3.24: Radially averaged vector from cluster centroid of each galaxy in our sample with axis ratio. The galaxies for XMM2215 are indicated with the blue crosses and the galaxies from XMM2235 are shown with the red circles.

3.3.5 Cluster masses

The redshifts we obtained for our emission line galaxy sample, were combined with those of the passive population from Chan et al. (2018), to estimate the dynamical masses of the clusters. As stated in section 3.3.4, the combination of the star-forming and passive populations yielded average redshifts for the two clusters of 1.3930 ± 0.0006 for XMM2235 and 1.4570 ± 0.0002 for XMM2215, which improves the accuracy of these values compared to the previous literature.

In order to obtain a reliable mass estimation for our clusters we assumed the virial theorem applies to their galaxy members and that the members of the cluster have approximately equal masses. This allowed us to calculate the masses of the two galaxy clusters using the virial mass estimator shown in equation 3.11 (Nascimento et al. 2016),

$$M_V = \frac{3\pi N}{2G} \frac{\sum (v_i - V)^2}{\sum_{i<j} 1/R_{ij}}, \tag{3.11}$$

where N is the number of galaxies in the cluster, v_i is the velocity of an individual cluster member, V is the mean velocity of all members, and R_{ij} is the separation between galaxies i and j.

Using this estimator we found that the cluster mass of XMM2215 is $(2.51 \pm 0.15) \times 10^{14} M_\odot$ and for XMM2235 is $(8.72 \pm 1.09) \times 10^{14} M_\odot$. These masses agree well with the X-ray emission calculated M_{200} values for each cluster in Stott et al. (2010), $M_{200} = (2.1^{+1.9}_{-0.8}) \times 10^{14} h^{-1} M_\odot$ and $M_{200} = (7.7^{+4.4}_{-3.1}) \times 10^{14} h^{-1} M_\odot$ for XMM2215 and XMM2235 respectively.

3.4 Discussion

3.4.1 Kinematics

For many parameters, our sample of cluster galaxies at $z \sim 1.5$ is generally consistent with star-forming field galaxies at this redshift, with no strong sign of influence of the cluster environment. This is perhaps unsurprising, as the galaxies in this sample of KCS are selected to be line-emitters in either [OII] or Hα. That said, there are some

deviations from the field population, which may be indicators of quenching mechanisms or the reversal of SFR - density relation, as discussed below.

3.4.1.1 Basic galaxy properties

The stellar masses and SFRs for our cluster sample were found to be in agreement with the SFMS at this epoch (Speagle et al. 2014), we found XMM2215 to be more actively star-forming than XMM2235.

The majority of our galaxies follow the mass-radius relation of Shen et al. (2003) for late-type galaxies at this redshift, as one would expect for star-forming galaxies in general. Similarly, the majority of our galaxies (83%) are disky, having Sérsic indices $n < 2$.

We therefore have an overall picture of the basic properties of star-forming galaxies in clusters being indistinguishable from their field counterparts at this redshift. However, as can be seen in sections 3.4.1.2 and 3.4.1.3, differences begin to emerge when we study these properties with respect to the galaxies' positions within the clusters.

3.4.1.2 Resolved galaxy properties

The kinematics of these galaxies were extracted from the resolved spectroscopy provided by KMOS. This includes; rotation velocity, velocity dispersion, and a 2D velocity map.

We used the ratio of velocity to velocity dispersion (v/σ) to decide whether a galaxy is rotation- or dispersion-dominated, where galaxies with $v/\sigma > 1$ were considered to be rotation-dominated. By this metric, 17% of our galaxies are dispersion-dominated while the majority (83%) are rotation-dominated as expected for star-forming galaxies. The median v/σ is 2.55, which is low compared with local galaxies ($5-20$, Epinat et al. 2010). This suggests that the enhanced star formation rate of cluster galaxies at this epoch is also driven by turbulence as is seen for the field. The dispersion-dominated galaxies were found to have the highest sSFRs, and sit above the SFMS. Indicating that starbursts are likely driven by disturbance.

The morphological major axis, derived from GALFIT, was compared with the kinematic axis, with larger differences suggesting a disconnect between the stellar and gas components, indicative of a disturbance (Ristea et al. 2022). The galaxies with the

largest differences were found to have the highest sSFRs which supports the idea that to have enhanced star-formation above the main-sequence, requires a disturbance.

3.4.1.3 Cluster environment phase space

While the resolved and global properties of the star-forming cluster galaxies are on average in agreement with those for the field population, we also studied how the location within the cluster affects the galaxies. To this end we used caustics in phase-space (space and velocity) to differentiate between the core, backsplash and infall regions.

When looking at the distribution of star-forming and passive galaxies in the clusters one can see that the passive galaxies of XMM2235 live almost entirely in the core whereas for XMM2215 they occur throughout suggesting the latter is not a relaxed system. This is further support for the relative youth of XMM2215 compared to XMM2235.

The highest SFR galaxies in XMM2215 and the ones lying above the SFMS were found to live preferentially in the core, with lower star-formation activity taking place in the backsplash region. The core of XMM2215 is of higher SFR than XMM2235 with median values of 42.22 ± 6.16 $M_{\odot}$ yr^{-1} and 22.24 ± 2.46 $M_{\odot}$ yr^{-1} respectively. This indicates the reversal of the morphology density relation may still be happening within XMM2215. That is, galaxies are still actively building up their stellar mass through star formation before becoming passive, as seen by prevalence of dusty star-forming galaxies in this cluster (Hilton et al. 2010; Ma et al. 2015). An alternative explanation is that the galaxies in XMM2215 are experiencing a final burst of star-formation before quenching due to violent processes such as ram-pressure stripping or major merging.

The galaxies in the core of XMM2235 were found to be more round in terms of their axis ratio when compared with galaxies outside, with a median value of 0.87 ± 0.06 for the core and 0.70 ± 0.05 for the backsplash galaxies. This may just be an indicator that the galaxies in the core are more face-on than we assumed when calculating the inclination angles in section 3.3.1.3, as we also found that these galaxies generally have disky Sérsic indices. However, it could also be an indicator of morphological transformation caused by the core. These round galaxies have similar sSFRs to the rest of the sample, which would indicate morphological change leading quenching

for some galaxies. We note that for the five core galaxies in XMM2235 three of the lowest mass galaxies have the highest (b/a). This perhaps indicates the relative ease of morphologically transitioning lower mass galaxies. This, coupled with the lower SFR in the core of XMM2235 compared with XMM2215, may be an indicator of the onset of so called 'Morphological Quenching' Martig et al. (2009). Lower mass galaxies are more susceptible to morphological changes due to; minor galaxy-galaxy interactions such as minor-mergers, and harassment. These events can lead to a more spheroidal morphology and in turn cause spontaneous quenching without removal or suppression of gas content by other mechanisms. These are also more likely to occur in the the more densely populated cluster core (Moore et al. 1996; Moore, Lake & Katz 1998).

The results above, relating to galaxy morphological change leading quenching of star formation in these clusters, are only potential scenarios, $\sim 2-3\sigma$. This is perhaps due to the fact that the phase space diagrams cannot distinguish between galaxies that have just entered a region of the cluster for the first time and those that have made multiple passes. This would act to wash out differences between the core and backsplash region. It is also a case for the need of a larger sample in order to draw more statistically significant conclusions.

3.4.1.4 Global cluster properties

Finally, we combined the redshifts for the star-forming and passive galaxies and derive dynamical masses for the clusters (XMM2215: $(2.51 \pm 0.15) \times 10^{14}$ $M_{\odot}$, XMM2235: $(8.72 \pm 1.09) \times 10^{14}$ $M_{\odot}$). These masses are in excellent agreement with those estimated from X-ray emission, again supporting the picture of XMM2215 being the lower mass, less mature system. This combined star-forming and passive sample also acts to update the cluster redshifts with values from this work: XMM2235 $= 1.3930 \pm 0.0006$ and XMM2215 $= 1.4570 \pm 0.0002$.

3.5 Conclusions

We have presented a near infrared IFS and photometric study of 24 galaxies in the two overdensities of XMM2215 ($z \sim 1.46$) and XMM2235 ($z \sim 1.39$) and provide a

summary of our key results below:

(i) SFMS of our star-forming galaxy sample occupy the same region of parameter space as the $z \sim 1.4 - 1.5$ field galaxies from CANDELS, suggesting that the SFMS of these galaxies is not strongly affected by the cluster environment.

(ii) We note a correlation between $|\sin(\mathrm{PA}_{im} - \mathrm{PA}_{kin})|$ and sSFR, such that more disturbed galaxies have a higher sSFR. This correlation is stronger when we consider the more active cluster, XMM2215.

(iii) $< v_{1.5}/\sigma >$ is lower in the $z = 1.4$ cluster environment compared to local values. This agrees with the field at this epoch and therefore turbulent disks are likely the driver of the high SFR.

(iv) $17 \pm 8.5\%$ of the sample, spread equally across the two clusters, are dispersion dominated and $83 \pm 18.68\%$ are rotation-dominated.

(v) The dispersion dominated sample all have large $|\sin(\mathrm{PA}_{im} - \mathrm{PA}_{kin})|$ which is further evidence of more disturbed systems driving star-formation.

(vi) The passive galaxies in XMM2235 live almost exclusively in the core compared to XMM2215 where they are scattered throughout phase-space. This reinforces that XMM2235 is a more dynamically relaxed cluster.

(vii) Galaxies with higher SFRs in XMM2215 live in the core of the cluster (2.8σ).

(viii) The majority of the core galaxies in XMM2215 lie above the SFMS relative to the rest of the sample (2.3σ).

(ix) Using the virial mass estimator with the star-forming (S.F.) and passive galaxies we find that the cluster mass of XMM2215 is $(2.51 \pm 0.15) \times 10^{14} M_{\odot}$ and for XMM2235 is $(8.72 \pm 1.09) \times 10^{14} M_{\odot}$ which agree well with the X-ray derived values from Stott et al. (2010).

(x) The combined star-forming and passive sample also acts to update the cluster redshifts with the new values being: XMM2235 $= 1.3930 \pm 0.0006$ and XMM2215 $= 1.4570 \pm 0.0002$.

(xi) We find that galaxies in the core of XMM2235 tend to be rounder than those outside of this core region for this cluster. One possible scenario is it may be an indication that morphological transformation is preceding cessation in star formation with morphological quenching a possible mechanism. However, more data would be needed to determine if this is significant.

(xiii) Beyond these conclusions we find no significant impact of cluster environment region on the kinematics of their S.F. galaxies.

Chapter 4

The Mass Metallicity and Fundamental Metallicity Relations for star-forming cluster galaxies at $z \sim 1.4$

Abstract

We present spectroscopic properties of 24 star-forming galaxies in two galaxy clusters at $z \sim 1.4$, from the emission line sample of the KMOS Cluster Survey (KCS). We compared the gas-phase mass metallicity and fundamental metallicity relations to those found in field galaxies at the same epoch. Our combined cluster galaxy sample show a difference between the mass metallicity relation found and that derived from field galaxy samples. This metallicity enhancement could be an indicator of additional quenching due to environment compared to the field at his epoch. However, this result is mainly driven by XMM2215 with XMM2235 being similar to the field. Investigating the intra-cluster regions we see the backsplash region shows a greater enhancement when compared to a mass metallicity relationship derived for field galaxies. This increased "metallicity" may not be due to abundance but perhaps an indication of the gas being shocked, producing an enhanced [NII] emission line due to ram pressure stripping. The fundamental metallicity relation for galaxies in our clusters is lower than that

for local galaxies but this is also true for field galaxies at this redshift. We believe the enhancement in metallicity in the cluster environment and increased [NII]/Hα emission line-ratio in the backsplash region indicate that the major driver of quenching in clusters at this epoch is ram pressure stripping.

4.1 Introduction

Investigating the gas phase metal content of galaxies in clusters allows us to constrain the impact of the cluster environment on their evolution. It reflects the star formation history of the galaxy and gas exchange between the galaxy and its environment. Much effort has been applied in studying the star-formation history (SFH) of the Universe for the general galaxy population. This SFH shows a clear increase in star formation rate across cosmic time, which reaches a peak at approximately $z = 1 - 2$. This stellar mass building seen in these field galaxies potentially occurs at earlier epochs in galaxies in clusters (Tran et al. 2010). The peak in the volume averaged star-formation rate (SFR) is followed by a gradual downturn to the present day (Madau & Dickinson 2014). This reduction is caused through a variety of quenching mechanisms, some of which can be traced through the examination of the emission line-ratios of the galaxies.

Star-formation has the net effect of increasing metallicity over time. However, metal content within a galaxy can be diluted by inflow and outflow which will in turn have an impact on stellar masses and SFR (Dalcanton 2007; Gao et al. 2018; Lilly et al. 2013). By studying line-ratios, we can track the evolution of the mass metallicity relation (MZR) across this universal peak in the volume averaged SFR for clusters at this epoch. This relation gives us an observable to compare across galaxies in order to describe the evolution history of galaxies.

Very few studies investigate the MZR in cluster galaxies but the few that do are crucial to our understanding of the importance of nature vs nurture in galaxy evolution (Ellison et al. 2009; Kacprzak et al. 2015; Magrini et al. 2012). Indeed studies of this relation often show conflicting results especially at higher redshifts (Kacprzak et al. 2015), especially in forming cluster environments. This confusion also occurs as cluster and field galaxies are often combined into a single sample when determining MZR, this will add environmental impacts into a sample that assumes very little and will cause confusion of interpretation. However, when comparing field galaxies samples across a range of redshifts we can see a smooth evolution of the MZR from $z \sim 3 - 0$ (Yabe et al. 2012).

Much of the work investigating metallicity relations in an environmental context occur at higher redshifts with protocluster environments ($z > 1.6$) and are concerned with the impact of early formation stages and when these relations evolve, if at all

(Kacprzak et al. 2015; Kulas et al. 2013; Shimakawa et al. 2015; Valentino et al. 2015; Wang et al. 2022). Valentino et al. (2015) reports that for star-forming galaxies in a protocluster at $z = 1.99$ the metallicity is lower than that seen in an analogous sample of field galaxies. Whereas Kulas et al. (2013) and Shimakawa et al. (2015) both show that low mass galaxies in their protoclusters demonstrate a metallicity enhancement compared with field galaxies. (Wang et al. 2022) ask whether the evolution is being established by internal processes or is it a gaseous inflow or outflow restriction causing an evolution in early galaxy cluster formation, that sets the mass metallicity relation development for the galaxy cluster.

Conversely to the MZR there is a more fundamental metallicity relation (FMR) that does not appear to evolve strongly with redshift (Mannucci et al. 2010). This brings in SFR as a third parameter that forms a three dimensional plane that connects stellar mass, metallicity, and SFR in a complex way (Mannucci et al. 2010). This low-z FMR has been found to be consistent with cluster galaxies at the cosmic noon ($z \sim 1.4$), perhaps demonstrating that the environmental impact on galaxy metallicity at this epoch is minimal (Magrini et al. 2012), this relation is even seen to show no evolution in field galaxies up to redshift ~ 3 (Curti et al. 2020).

A highly valuable tool in observational astronomy is integral-field-spectroscopy (IFS), which allows the observer to gain spatially resolved spectroscopy in a single observation. The power of IFS data analysis in galaxy studies and kinematic investigation has already been proven through many large surveys at cosmic noon (e.g. chapter 3, Beifiori et al. 2017; Stott et al. 2016) and in low z clusters (e.g. Medling et al. 2018). IFS studies have expanded our understanding of the peak in the SFH of the Universe with results indicating that gas-rich disks are more turbulent at $z \sim 1 - 3$ (Förster Schreiber et al. 2009; Stott et al. 2016; Swinbank et al. 2012; Wisnioski et al. 2015), in contrast the local Universe exhibits much lower turbulence in these disks (Epinat et al. 2010). This is the likely driver of the peak in the SFH for field galaxies.

Multiplexing IFS facilities are becoming more common, e.g. Very Large Telescope (VLT)/K-band Multi Object Spectrograph (KMOS; Sharples et al. 2013), Anglo Australian Telescope (AAT)/Sydney-Australian-Astronomical-Observatory Multi-object Integral-Field Spectrograph survey (SAMI; Croom et al. 2012) and are particularly useful for probing cluster galaxies due to their on-sky density. The recent introduction of the multiplexed William Herschel Telescope (WHT)/WHT Enhanced

Area Velocity Explorer (WEAVE; Dalton et al. 2012) will not only expand on existing multiplexing IFU facilities but also offers several modes including a massively multiplexed MOS and monolithic IFU. Available facilities are further expanded with the recent start to science operations of *JWST*/Near InfraRed Spectrograph (NIRSpec; Jakobsen et al. 2022) with its greater depth and spatial resolution of single IFS, and in the future with the European-Extremely Large Telescope (E-ELT)/High Angular Resolution Monolithic Optical and Near-infrared Integral field spectrograph (HARMONI; Thatte et al. 2010).

The focus of this chapter is to assess the gas phase metallicity of star-forming galaxies in clusters at $z \sim 1.4$. We utilise the [NII]/Hα emission line-ratio in the galaxy sample, combined with the Hα derived SFR and stellar mass from complementary near-infrared (NIR) photometry. We investigate the environmental impact on the MZR and FMR at this early epoch of galaxy cluster development. This is to determine whether the metallicity provides any information on potential evolutionary mechanisms that may be at work in dense environments at this epoch. These will be placed in the context of their positions within their respective clusters, using a cluster phase-space analysis as performed in chapter 3.

4.2 Data sample

The data used in this chapter was the same source outlined in chapter 2 and followed the same reduction and extraction methodology. However, here we did not use the data in a spatially resolved way but rather we determined spatially unresolved properties in order to increase the S/N of our final sample. Resolved analysis is very useful and a powerful diagnostic tool however for this sample the signal of the [NII] emission line is too low to be useful for line-ratio analysis in our case.

4.3 Analysis and results

In this chapter, the unresolved Hα and [NII] emission was used to assess the mass metallicity relation (MZR) and fundamental metallicity relation (FMR) for star-forming

cluster galaxies at $z = 1.4$. We then discuss these relations in the context of the cluster environment phase-space.

4.3.1 Mass and SFR

Throughout this chapter we used the stellar mass and SFRs calculated in chapter 3 from the complementary photometry and Hα emission respectively. We obtained the SFR assuming a Chabrier initial mass function (IMF, Chabrier 2003) and from Kennicutt (1998) we use equation 4.1:

$$\text{SFR} = 4.4 \times 10^{-42} \left(\frac{F_{\text{H}\alpha} 4\pi d_L^2}{10^{\frac{A_{\text{H}\alpha}}{-2.5}}} \right) \tag{4.1}$$

where $F_{\text{H}\alpha}$ is the Hα flux, d_L is the luminosity distance to the cluster, and $A_{\text{H}\alpha}$ is extinction. We assumed $\text{A}_{\text{H}\alpha} = 1$ as in Sobral et al. (2012).

We obtained stellar masses for our sample using the preferred *HST*/WFC3 F160W or calibrated VLT/HAWK-I photometry using the method outlined in Stott et al. (2020), for the redshift range $z \sim 1.4 - 1.5$ with the following:

$$\log \left(\frac{M}{M_\odot} \right) = (-0.5120 \pm 0.006) \text{m}_{F160W} + (21.62 \pm 0.15), \tag{4.2}$$

for further detail we refer the reader to chapter 3.

4.3.2 Metal abundance calibration

To measure the [NII] to Hα line-ratio we used our unresolved 1D spectra from section 3.2.1. An example 1D spectral fit can be seen in figure 3.1 which highlights a fit to Hα and the [NII] emission lines.

In order to obtain metallicity we adopted a method to convert to oxygen gas abundance from our chosen line-ratio. First we convert the $f_{[\text{NII}]}/f_{\text{H}\alpha}$ ratio into the N2 quantity via equation 4.3 (Alloin et al. 1979; Denicoló, Terlevich & Terlevich 2002; Kewley & Dopita 2002),

$$\text{N2} = \log(f_{[\text{NII}]}/f_{\text{H}\alpha}) \tag{4.3}$$

where $f_{[\mathrm{NII}]}$ is the flux of the 6585Å [NII] emission line and $f_{\mathrm{H}\alpha}$ is the flux of Hα. This N2 value can then be used to estimate oxygen abundance using the method outlined in Pettini & Pagel (2004) and shown in equation 4.4,

$$12 + \log(\mathrm{O/H}) = 8.9 + 0.57 \times \mathrm{N2}. \tag{4.4}$$

This provided our gas-phase metal abundance estimates used for the remainder of this work.

4.3.2.1 Signal-to-noise ratio

The integrated Hα emission line is detected to S/N > 6 in all cases with a median value of ~ 26 for the 1D spectra integrated over the aperture centred on the target galaxy as described in the initial galaxy spectral fitting in section 3.2.1. In order to assess the significance of the line ratios we must also determine the S/N of the 6585Å [NII] emission line. To do this we compared the χ^2 of two models derived from the 1D Gaussian fit demonstrated in figure 3.1 in order to determine the signal to noise of the 6585Å [NII] emission line. This was performed by taking the square root of the difference between the χ^2 of the sum of three gaussian model and that of a sum of two Gaussians. The two Gaussian model was fit only to the blue [NII] and Hα i.e. ignoring 6585Å [NII]. We estimated the noise from a section of the spectrum ~ 1500 Å away from the emission lines and any potential skyline contamination. We took these [NII] S/N and apply a simple cut at S/N > 2, if a value was less than this threshold then we assumed an unreliable point and took double the noise level as an upper limit. We identified a single galaxy that failed to reach this threshold and so our sample has good S/N, the remaining galaxies achieved a S/N > 6 in all cases with a median value of ~ 12.

During this assessment we also identified galaxies with skylines within the FWHM of the 6585Å [NII] emission line and identified those that are deemed to fit poorly with the sum of three Gaussian model. Eight galaxies in the sample have a skyline located within the designated range and two of these were deemed to fit poorly. These points are highlighted across the appropriate plots throughout this work.

4.3.2.2 AGN identification and classification

We also used the [NII] to Hα line-ratio to identify any potential AGN in our sample assuming a positive N2 to be a potential AGN by comparing to the BPT diagram (Baldwin, Phillips & Terlevich 1981). We cannot make a definitive identification using this method as the line ratio we use, [NII]/Hα, is a single axis of the diagram as we have no spectral coverage of [OII] and Hβ. Based on this assumption we found two potential AGN in our sample; (XMM2215_IFU22 - RA: 334.00161 and DEC: -17.63065 and XMM2235_IFU2 - RA: 338.84116 and DEC: -25.92744) with $\log_{10}([\mathrm{NII}]/\mathrm{H}\alpha) = 0.1$ and $([\mathrm{NII}]/\mathrm{H}\alpha) = 0.09$ respectively.

However, this simplistic approach is limited as we are only considering a single axis of data and can only indicate possibilities. More in-depth diagnostics can be used in order to determine the AGN type or if these galaxies can be classified as AGN, Star-forming, or passive galaxies. Although we have limited spectral lines that can be used we can still use other properties of those lines to delineate AGN and galaxy type. This diagnostic (WHAN; Cid Fernandes et al. 2011) uses the [NII]/Hα and the equivalent width of the Hα line (EW[Hα]) in order to delineate between LINER and Seyfert AGN type and passive galaxies on the y-axis as follows, star-forming and AGN are delineated on the x-axis. Using the line-ratios from Stasińska et al. (2006) there is an additional hybrid region between star-forming and AGN adding ambiguity to these separations between $\log_{10}([\mathrm{NII}]/\mathrm{H}\alpha) = -0.4$ and $([\mathrm{NII}]/\mathrm{H}\alpha) = -0.2$. Therefore, we note the two AGN previously simplistically identified in this section are the only two AGN in this sample we can adequately define as AGN (Seyfert specifically) within the calculated errors using this approach.

4.3.3 Mass metallicity relation

We investigated the MZR of our $z = 1.4$ cluster galaxies and compared to the relationships found in other samples across a range of z and environment. The MZR for this work is displayed in figure 4.2, along with some comparisons. The most relevant comparison would be the relationship from Yabe et al. (2012) as this is from a field sample at $z \sim 1.4$. The majority of our sample lies above this relationship meaning they

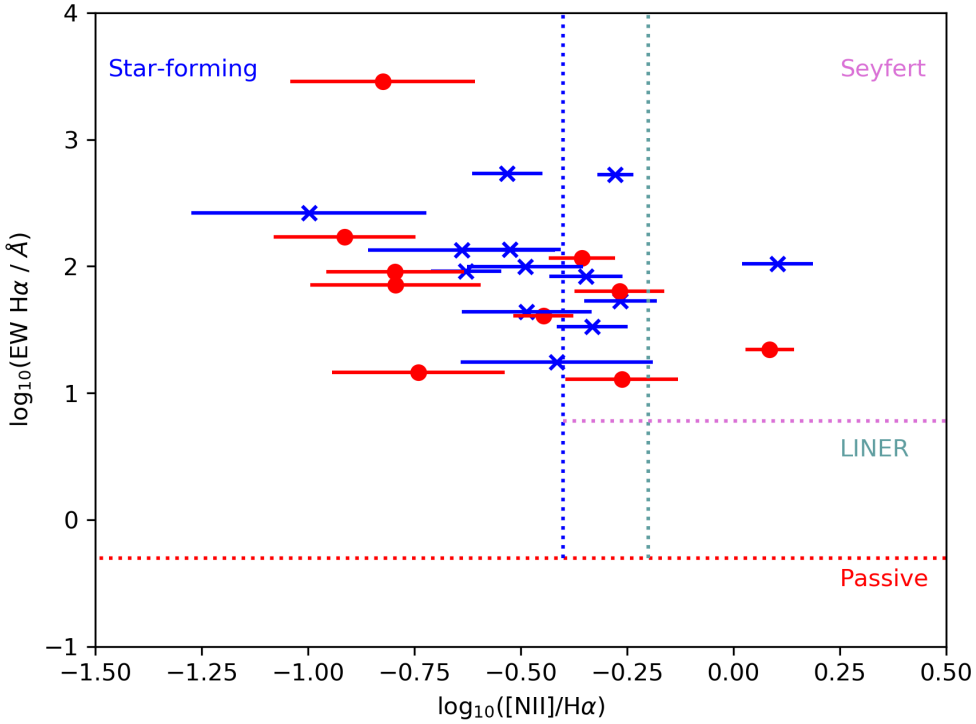

Figure 4.1: $\log_{10}$ EW Hα vs $\log_{10}([\text{N}\textsc{ii}]/\text{H}\alpha)$. Regions of this plot are demarcated into Star-forming, passive, Seyfert, and LINER galaxies and AGN respectively. The vertical dotted light blue line in the Seyfert/LINER region indicates an extra line of uncertainty and can be described as a hybrid Star-forming/AGN region. The blue crosses indicate galaxies from XMM2215 and the red circles indicate galaxies from XMM2235. From this we can see that with reasonable certainty two galaxies are Seyfert AGN and when considering the uncertainties of this analysis the remainder are likely Star-forming galaxies with no passive galaxies present.

are more metal-rich. This may be an indicator that environment is impacting evolution of the inter-stellar medium (ISM) at, resulting in an earlier enrichment at this redshift.

We fit two relationships to our data. A multi-order polynomial and linear model to aid comparison with other studies. When performing these fits we did not include data that was designated as having a poor spectral fit, poor S/N, or is identified as an AGN. The polynomial has the form

$$12 + \log(\mathrm{O/H}) = -0.0864(\log M_* - \log M_0)^2 + K_0 \tag{4.5}$$

from Maiolino et al. (2008) where M_* is stellar mass and K_0 is a constant. The best fitting values for our sample were $\log M_0 = 12.16 \pm 0.62$ and $K_0 = 8.91 \pm 0.18$. These parameters align well with the Maiolino et al. (2008) fit to the data of (Erb et al. 2006) $z = 2.2$ ($\log M_0 = 12.38$ and $K_0 = 8.99$), shown in figure 4.2, and across the redshift range used in Maiolino et al. (2008). We therefore did not include our polynomial fit in figure 4.2 as it was very similar to that described by the latter.

The linear model used follows the form

$$12 + \log(\mathrm{O/H}) = \alpha(\log M_*) + \beta \tag{4.6}$$

where the fit coefficients for our galaxies are found to be $\alpha = 0.31 \pm 0.10$ and $\beta = 5.40 \pm 1.07$.

We can see that over the mass range of our data both the linear and polynomial fit are valid. Without galaxies at higher or lower masses than our sample it is not possible to determine if the relationship is better described by one or the other. As these fits are very similar in the mass range of our sample, going forward we used the linear relationship from equation 4.6, as this describes the data well with the fewest parameters. The scatter about the linear model is shown in figure 4.3, along with the scatter about the fit from Yabe et al. (2012).

By qualitative assessment of the individual clusters compared to the MZR relationships from other works, we see that the cluster XMM2235 sits more closely to the fit for $z \sim 1.4$ galaxies from Yabe et al. (2012). This contrasts with XMM2215 which sits at higher metallicity. In order to quantify this we calculated the RMS scatter for each of these clusters individually compared to the Yabe et al. (2012) line and found that the RMS scatter for XMM2215 about this line is 1.05 and for XMM2235 it is 0.16, thereby

reinforcing our qualitative assessment. We also assess the median of the residuals of the line from Yabe et al. (2012) and found that for the combined sample there is an enhancement of $\Delta(\text{O/H}) = 0.09 \pm 0.03$ dex. We found that the median residuals from the Yabe et al. (2012) MZR for XMM2215 and XMM2235 are $\Delta(\text{O/H}) = 0.16 \pm 0.03$ dex and $\Delta(\text{O/H}) = 0.01 \pm 0.03$ dex respectively, thereby reinforcing our argument. Work carried out in Maier et al. (2019) on a subset of galaxies in the virialised core of XMM2215 agrees with this view but our results from XMM2235 contradict that this is a global result for all star-forming galaxies in clusters at this epoch.

4.3.4 Fundamental metallicity relation

We continued our investigation of metallicity dependences within our sample by assessing the FMR at this epoch. This is the dependence of metallicity on both stellar mass *and* SFR. At a given stellar mass, metallicity is found to anti-correlate with SFR, such that high SFR galaxies are similar to low mass ones. In this work we visualised this relationship in figure 4.4 by plotting metallicity against $\log_{10}(\text{SFR})$ and placing $\log_{10}(\text{M}_*)$ in colour space as a third axis. We assessed our SFR-metallicity relationship in figure 4.4 alongside relationships from Mannucci et al. (2010) for a range of stellar masses. These curves show some evidence that there is a misalignment of our sample with the FMR in Mannucci et al. (2010) but that a plane appears to be present.

In order to assess how well our data aligns with the FMR we used a linear combination of stellar mass and SFR as in Mannucci et al. (2010) which is defined by

$$\mu_\alpha = \log(\text{M}_*) - \alpha \log(\text{SFR}), \tag{4.7}$$

where α is a free parameter that minimises the scatter in metallicity. We adopted $\alpha = 0.32$ as presented in (Mannucci et al. 2010). This FMR was calibrated at low-z but is supposed to be applicable out to $z = 2$ (Mannucci et al. 2010). To that end we plotted metallicity verses $\mu_{0.32}$ with stellar mass in colour space in figure 4.5. On this figure we over-plotted the linear relationship derived in Mannucci et al. (2010) for their sample of SDSS galaxies alongside a fit for our sample, using the same exclusions from our previous fitting. We can see that the majority of our sample lies below the fit from Mannucci et al. (2010) ($\text{O/H} = 0.48(\mu_{0.32} - 10) + 8.9$), and our

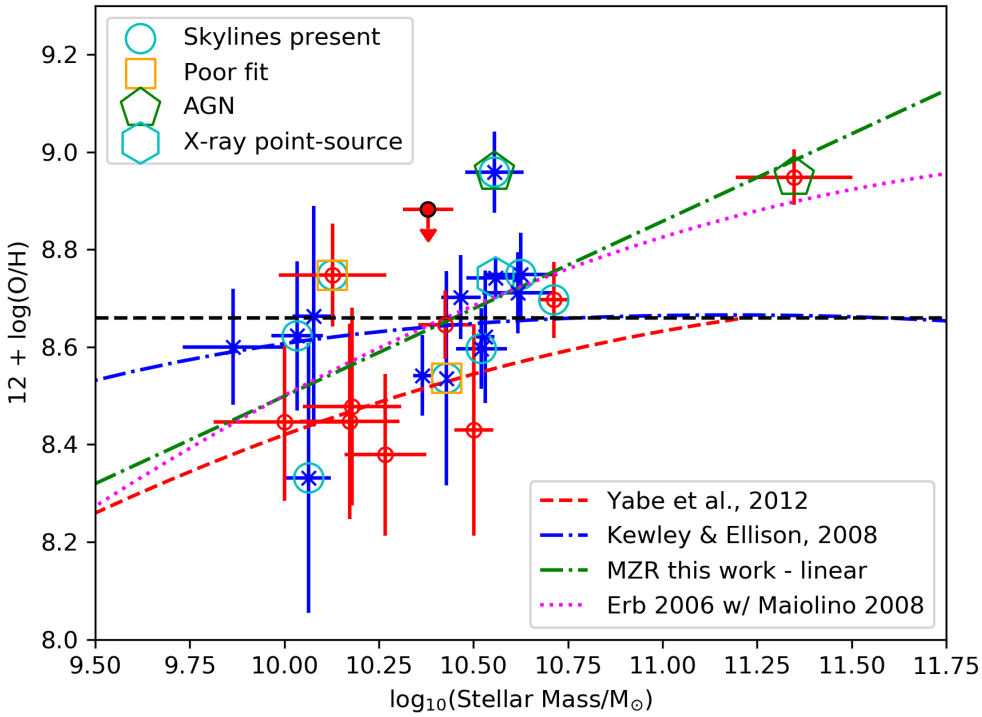

Figure 4.2: The mass metallicity relation for our star-forming cluster galaxy sample. Blue crosses indicate galaxies in XMM2215, red circles indicate galaxies in XMM2235. Those galaxies highlighted with a cyan circle have skylines within the FWHM of the [NII] line, those highlighted with an orange box indicate galaxies where skylines have adversely impacted the fit. Galaxies highlighted with a green pentagon show likely AGN. For those galaxies where the S/N of the [NII] emission line is poor (S/N < 2) we only indicate an upper limit. Also included are the MZR fits for $z \sim 0.1$ (Kewley & Ellison 2008), the blue dot-dashed line, and $z \sim 1.4$ (Yabe et al. 2012), the red single dashed line, and the magenta dotted line at $z \sim 2.2$ (Erb et al. 2006; Maiolino et al. 2008). We also include a linear fit to our sample shown by the dot-dashed green line.

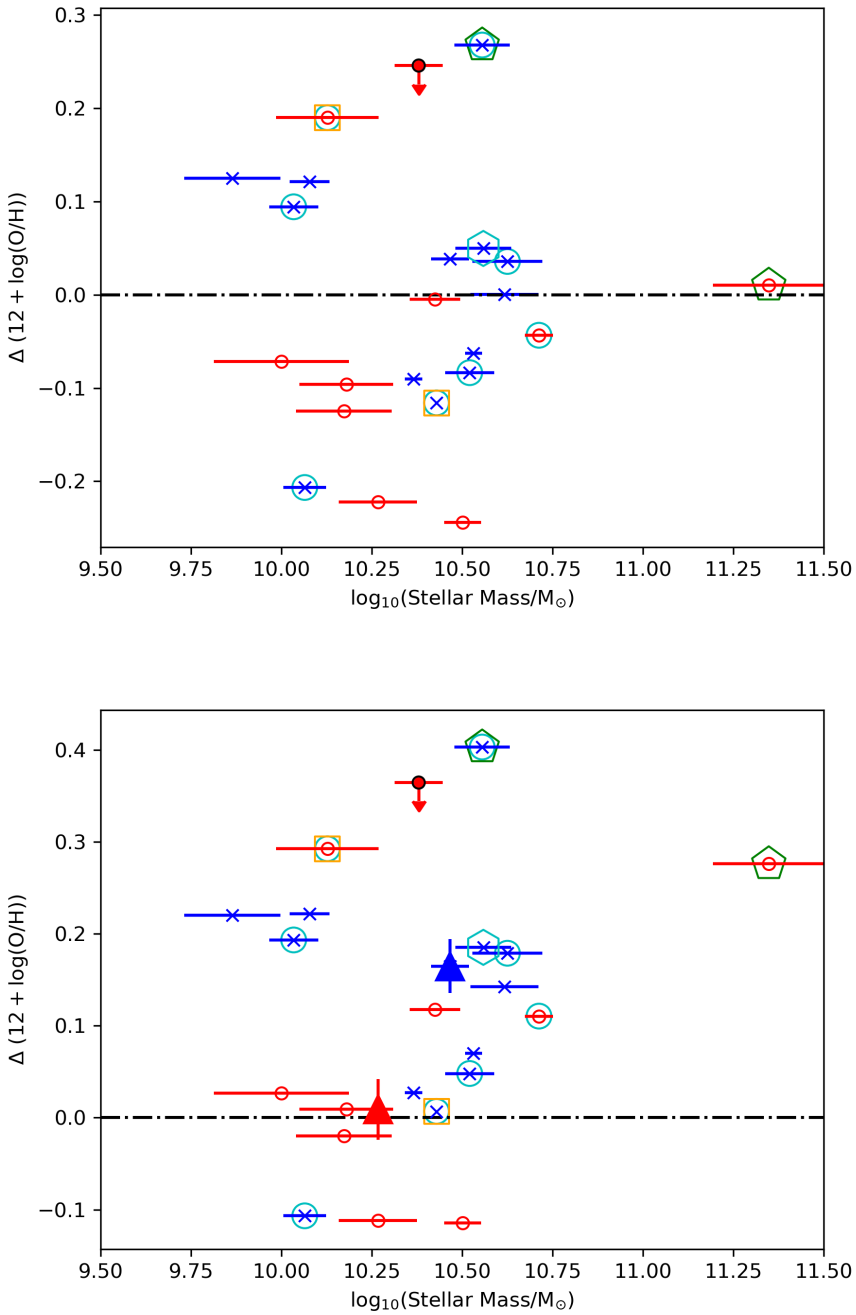

Figure 4.3: *top:* Scatter in MZR about the linear fit to our galaxies. Highlighted points follow the same convention as in figure 4.2. The blue crosses indicate galaxies from XMM2215 and the red circles indicate galaxies from XMM2235. *bottom:* Scatter in MZR compared to the relationship from Yabe et al. (2012) with this work with median values for each cluster and associated standard error, shown as the blue triangle for XMM2215 and the red triangle for XMM2235. The blue crosses indicate galaxies from XMM2215 and the red circles indicate galaxies from XMM2235. It is clear that XMM2215 is at higher metallicity.

fit (O/H $= 0.36 \pm 0.12(\mu_{0.32} - 10) + 5.09 \pm 1.18$) also has a shallower gradient than the fit from Mannucci et al. (2010), although we should note that the upper error on the gradient from the fit to our galaxies would bring it in line with that found in Mannucci et al. (2010). As with the MZR we compare our cluster sample to the field. The median residuals of our combined cluster sample shows a deficit of Δ(O/H) $= -0.28 \pm 0.03$. This deviation is replicated in individual clusters where the median residual for XMM2215 is Δ(O/H) $= -0.21 \pm 0.03$ and Δ(O/H) $= 0.32 \pm 0.03$ for XMM2235. This is potentially an indicator of environmental factors playing a role in the position of the FMR at a given epoch as we see a consistent overestimation of the predicted metal content of our cluster galaxy sample. However, we note that some field galaxy samples at this redshift, when using the same metallicity calibrations, also find a deficit with Mannucci et al. (2010) e.g. Stephenson et al. (2024).

4.3.5 Cluster environment

We then placed the gas phase metallicity of the individual galaxies, the FMR, and MZR in the context of the cluster environment. Galaxies may have entered the cluster at different times and so investigating where this sample is located in their respective intra-cluster regions allows us to gain an appreciation of the different evolutionary history of our sample. This is similar to the analysis presented in Maier et al. (2019), which uses one of the clusters presented in this work. We note however, that here we did not isolate galaxies within the virialised core at a defined fraction of r_{200} but expanded our analysis to include the wider cluster environment using the relative kinematics of the individual galaxies to their host cluster combined with relative positional information.

4.3.5.1 Metallicity within the cluster environment

Using the definitions for cluster phase-space discussed in chapter 3 we looked to determine potential correlations between metallicity and cluster environment, if any (see figure 4.6). Galaxies in the virialised core were found to have median $\log$(O/H) $= 8.49 \pm 0.39$ dex. Those outside the core have median $\log$(O/H) $= 8.71 \pm 0.04$ dex. However, this apparent lower metallicity in the core is not statistically significant and

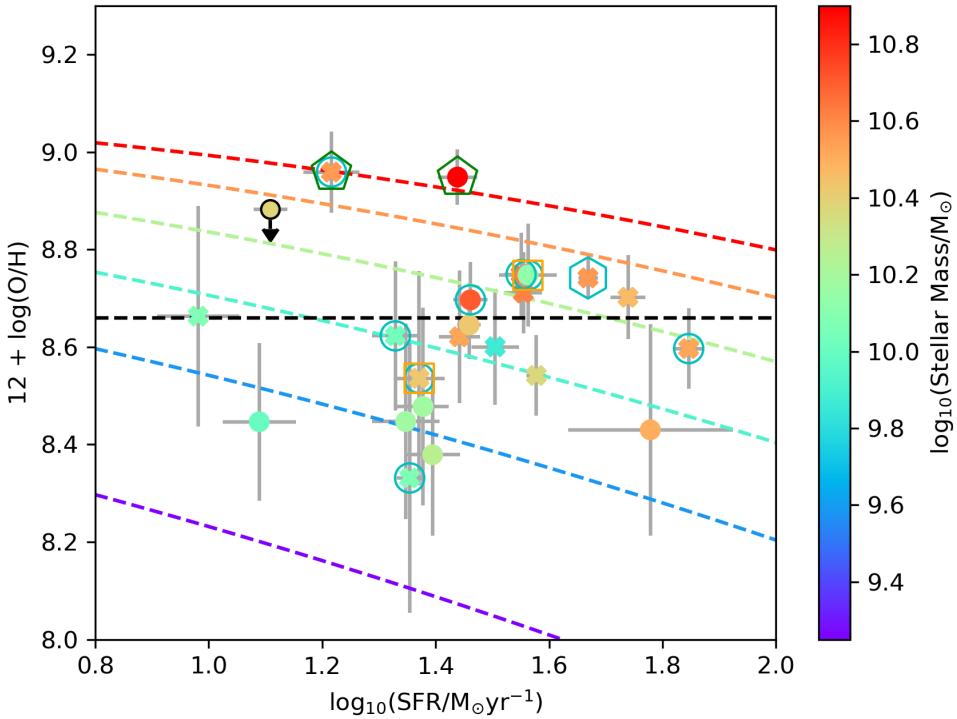

Figure 4.4: The fundamental metallicity relation for our star-forming emission-line cluster galaxy sample. The same highlights are used as figure 4.2. Plotted above are a range of stellar mass FMR curves from Mannucci et al. (2010) in the same colour-space as the individual galaxy stellar mass. The coloured crosses indicate galaxies from XMM2215 and the coloured circles indicate points from XMM2235. Solar metallicity is indicated by the black dashed line.

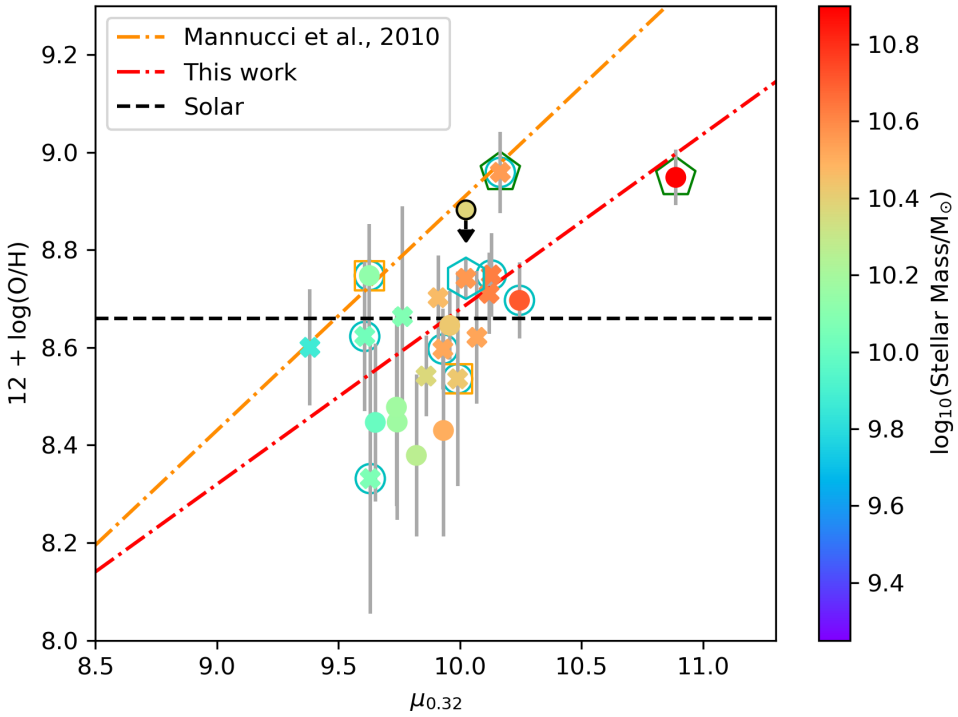

Figure 4.5: Fundamental metallicity relation expressed as $\mu_{0.32}$ as in Mannucci et al. (2010). The orange dot-dashed line is the fit produced in Mannucci et al. (2010) whereas the red dot-dashed line is a fit performed on the sample from this work excluding any AGN or indicated poor fits. Also shown in colour space is stellar mass as in figure 4.4. Solar metallicity is indicated by the black dashed line.

was further investigated using a radially averaged vector plot of Mpc h^{-1} shown in figure 4.7, which does not highlight anything further.

In figure 4.8 we collapsed this phase-space into a single axis, Γ (equation 3.10), to put mass, metallicity, and SFR in an environmental context. Investigating any correlations between these properties is important as it may indicate the preferred quenching mechanism. However, there was little correlation between these properties and cluster phase space.

We note deviations from established relationships from previous work with regards to the MZR and FMR from Yabe et al. (2012) and Mannucci et al. (2010) respectively with our combined sample (see sections 4.3.3 and 4.3.4). We assessed the deviation of galaxies from these relations with respect to their location within the cluster, figure 4.9. Assessing the median metallicity residuals of these intra-cluster regions, we find that there may be an enhancement (2.5σ) in the backsplash region ($\Delta(\text{O/H}) = 0.15 \pm 0.04$) compared to the virialised core ($\Delta(\text{O/H}) = 0.03 \pm 0.03$). Therefore, while our results for an overall metallicity enhancement for clusters at this epoch agrees with Maier et al. (2019), this higher metallicity backsplash region may disagree with their interpretation i.e. if cluster galaxies show higher metallicity because they have had their pristine gas supply removed, why do more recent arrivals show a stronger effect? The core members should be the ones with their gas supply cut off for the longest period. With regards to the FMR we note that the most significant deviation occurs in XMM2215 (2.3σ) with a deviation a field galaxy FMR from Mannucci et al. (2010) of $\Delta(\text{O/H}) = -0.26 \pm 0.03$ for the virialised core and $\Delta(\text{O/H}) = -0.13 \pm 0.05$ for the backsplash region.

4.4 Discussion

We study the effect of environment on metallicity and for 24 star-forming galaxies in two galaxy clusters at cosmic noon. We compare our cluster galaxy sample to metallicity relations derived from field galaxy samples at a similar epoch. We also subdivide our sample into intra-cluster regions to determine if recently captured galaxies are impacting our overall view of galaxy clusters at the cosmic noon.

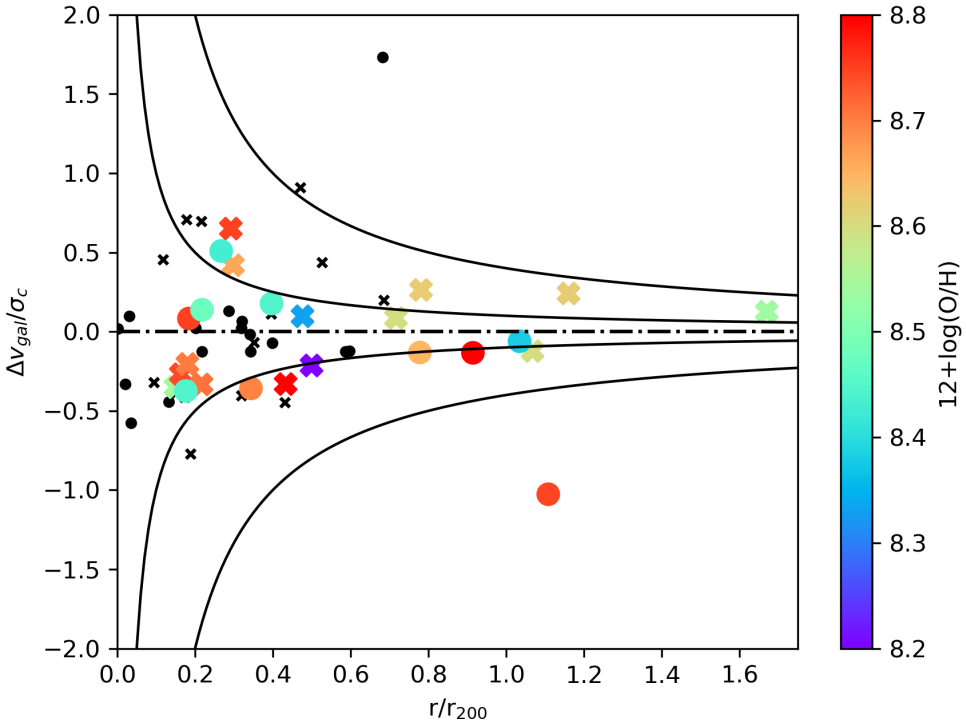

Figure 4.6: A cluster phase-space plot of relative galaxy line-of-sight velocity normalised by cluster velocity dispersion against galaxy distance from cluster centre normalised by r_{200}. The crosses indicate those galaxies in XMM2215 from this work and the circles indicate those within XMM2235 from this work, these are coloured with metallicity. All black points indicate passive galaxies from Chan et al. (2018). The black curves represent lines of constant Γ, the inner line is $\Gamma = 0.1$ and represents the boundary of the cluster virialised core, the outer line $\Gamma = 0.4$ and represents the outer boundary of the cluster. Galaxies between these two curves are defined as backsplash galaxies and those beyond $\Gamma = 0.4$ are approaching infall.

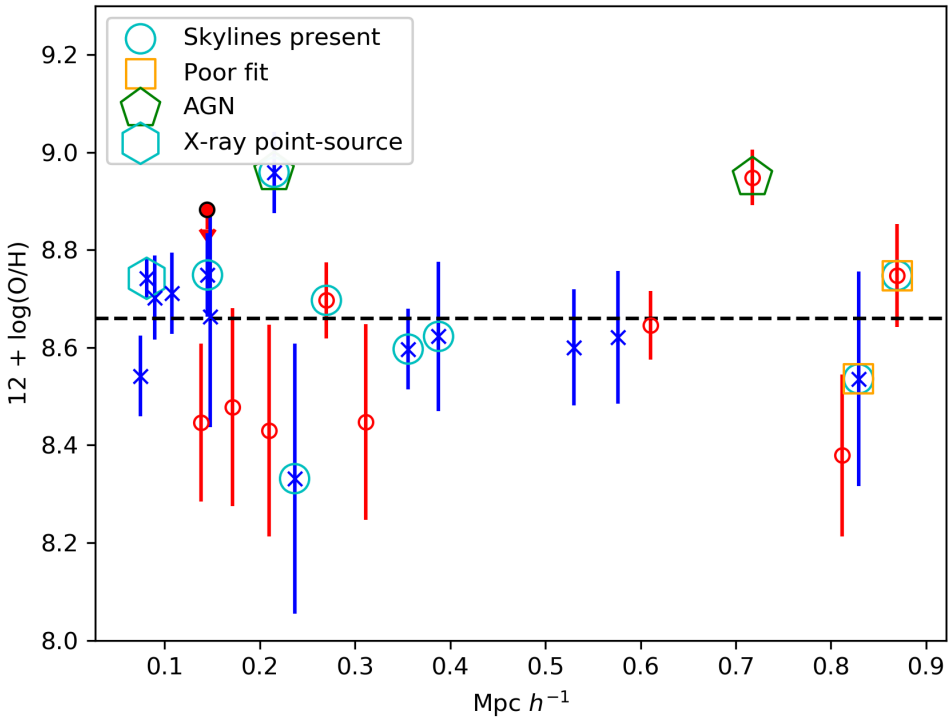

Figure 4.7: Metallicity of our cluster galaxy sample plotted against a radially averaged vector from the cluster core (Mpc h^{-1}). The blue crosses indicate those galaxies in XMM2215 from this work and the red circles indicate those within XMM2235 from this work. The black dashed line indicates solar metallicity.

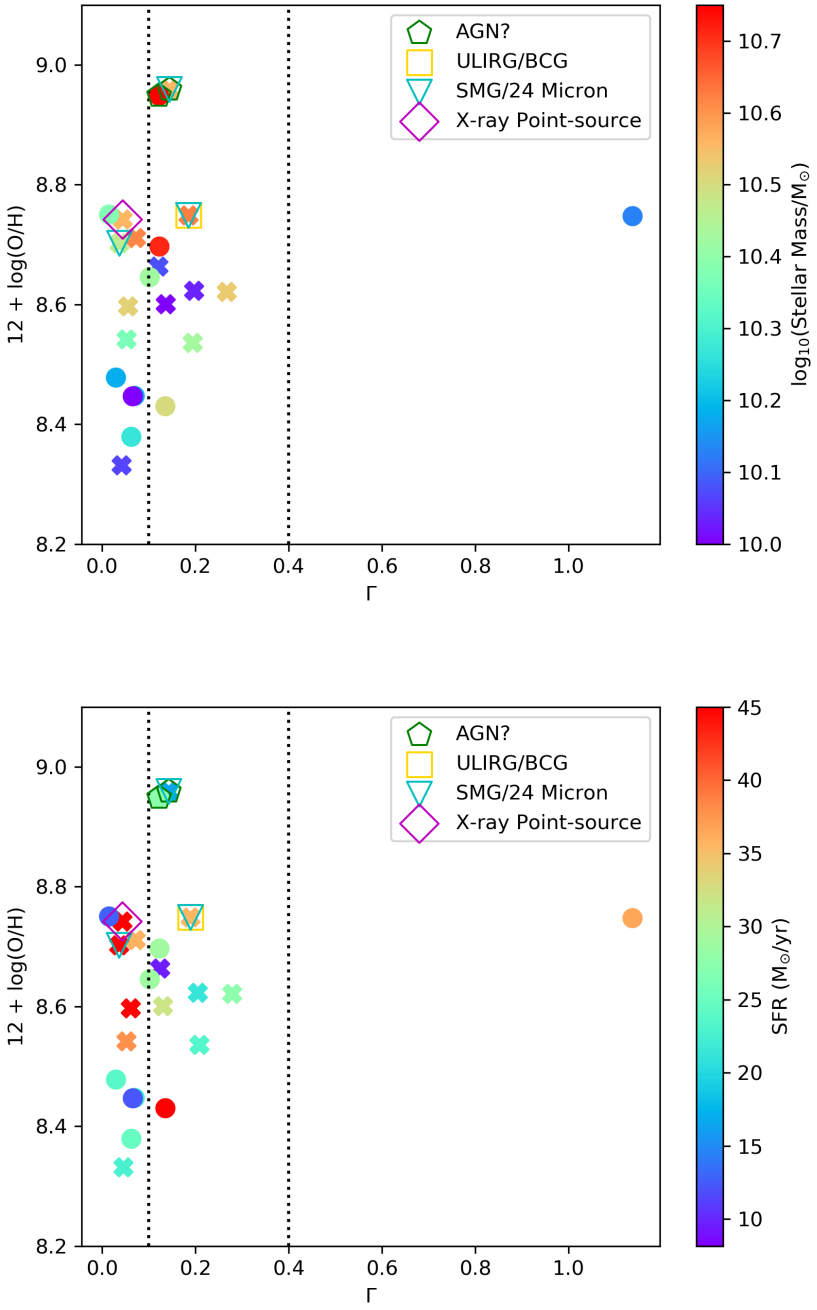

Figure 4.8: *top:* Metallicity with cluster phase-space collapsed to a single axis with stellar mass indicated by colour space. The region boundaries are indicated by dotted vertical lines, with galaxies below 0.1 being within the virialised core, the points between 0.1 and 0.4 being within the backsplash region, and any points beyond 0.4 on infall and being captured by the cluster. The crosses indicate galaxies from XMM2215 and the circles indicate galaxies from XMM2235. Highlighted points follow the same convention as in figure 4.2. *bottom:* As with the left panel of this figure with SFR being indicated by colour space.

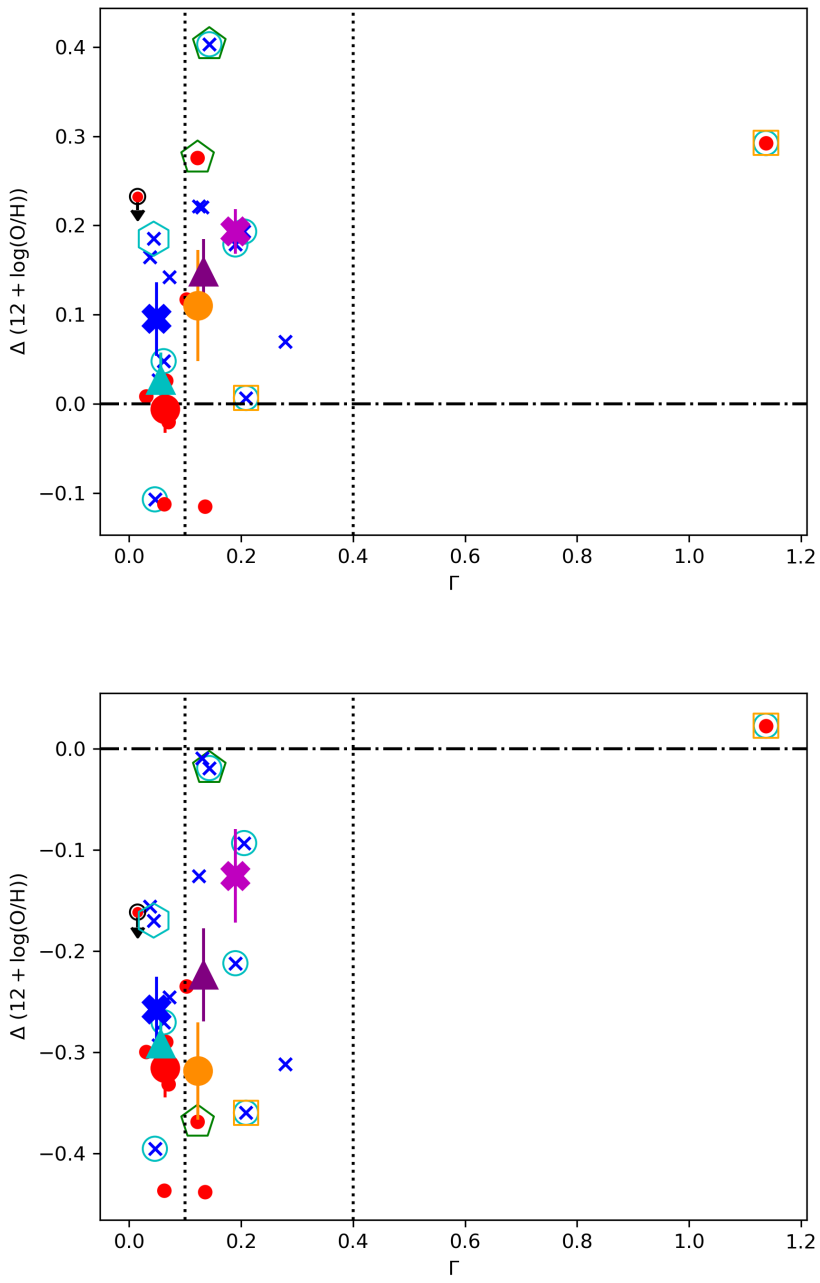

Figure 4.9: *top:* Scatter in MZR compared to the relationship from Yabe et al. (2012) with this work with cluster environment. These plots follow the convention of figure 4.8. *bottom:* Scatter in FMR compared to the relationship from Mannucci et al. (2010) within cluster phase-space. The large blue cross shows the median for the core of XMM2215 while the large magenta cross shows the median for the backsplash region of XMM2215. The large red circle shows the median for the core of XMM2235 while the large orange circle shows the median for the backsplash region of XMM2235. The large triangles indicate the medians for the combine cluster sample for the core and backsplash regions, cyan and dark purple respectively.

4.4.1 Environmental impact on MZR

The MZR for our sample as a whole lies above the relationship derived for field galaxies at the same redshift as our sample from Yabe et al. (2012) ($\Delta(\mathrm{O/H}) = 0.09 \pm 0.03$ dex). This is an indicator that the cluster environment is having an impact on this relation with galaxy evolution and chemical enrichment being advanced compared with the field. However, this result is driven by XMM2215, our younger more active cluster. Work carried out in Maier et al. (2019), using a sample of cluster galaxies within $0.5R_{200}$ of the virialised core of XMM2215 indicates, that as those galaxies are of higher metallicity than an equivalent sample of field galaxies, they are undergoing strangulation. They go on to say that this is likely due to cessation of dilution of the ISM from pristine gas after a stripping of the hot halo gas. This argument is based on a strangulation scenario presented in (Shimakawa et al. 2015) using stacked metallicity measurements of galaxies in a protocluster at $z > 2$. However, as noted by Kacprzak et al. (2015), there is a large amount of confusion and inconsistency even between comparable data sets when investigating this relationship, therefore the difference here should be treated with caution. Kacprzak et al. (2015) and Tran et al. (2015) both do not find this metallicity enhancement and find that their cluster galaxies at $z > 1.6$ are consistent with comparable field galaxy samples. We also found this when considering XMM2235, which agrees with the relationship from Yabe et al. (2012). This is interesting as XMM2235 is a more evolved galaxy cluster, but with star-forming galaxies with lower metallicity. These noted differences may be merely cluster the cluster variation or this may be due to XMM2235 forming at earlier times to XMM2215 in a lower metallicity Universe, showing that differences in the relationships establish early in the stages of formation. Comparing the difference in metallicity of our sample to that of the mass metallicity relation found in Yabe et al. (2012) in a more granular way, we found that the core of our combined cluster sample lies at $\Delta(\mathrm{O/H}) = 0.03 \pm 0.03$ dex in metallicity and the backsplash at $\Delta(\mathrm{O/H}) = 0.15 \pm 0.04$ dex. While this result may be indicative of a result ($\sigma = 2.5$), more data would be needed to test if it is significant. However, it may indicate that higher metallcity star-forming galaxies are avoiding the virialised core region. It could show that the more recent galaxies to enter the cluster have a greater deviation from the Yabe et al. (2012) relationship compared to the galaxies that reside in the core. This is at odds

with the interpretation of Maier et al. (2019) and seems counter-intuitive as quenching is presumably stronger in the core and has lasted for longer. This indicates that the galaxies recently accreted by the clusters are enhancing the overall metallicity of the cluster. However, the enhanced line-ratios, [NII]/Hα), outside the core may instead indicate shocks (Armus, Heckman & Miley 1989; Poggianti et al. 2019; Rich, Kewley & Dopita 2011), rather than metallicity such shocks would be caused by ram-pressure stripping (RPS) interactions with the ICM from their first pass of the cluster. Both clusters were initially detected in X-rays so have mature ICM to provide RPS. The enhanced metallicity of the cluster environment favours either RPS or strangulation as the dominant quenching mechanism. However, the potential evidence for shocks in the backsplash region, favours RPS.

4.4.2 Environmental impact on FMR

We note that the when examining the FMR for this sample and comparing with Mannucci et al. (2010) we see the majority of our sample lies below the relation derived for their SDSS galaxy sample, see figures 4.5 and 4.9. We fitted our own relationship and demonstrate an FMR for our sample is below and shallower in gradient than the sample used in Mannucci et al. (2010) despite their evidence to show that this relation is not variable across a range of redshifts ($z < 2.5$). However, we also note that their investigation, and much of the work carried out on the FMR, do not include cluster galaxy samples. Therefore, this may again be an indicator that the cluster environment does have an impact on this relation even if redshift does not. This result demonstrates that for a given SFR and stellar mass the metallicity is lower than that predicted by the FMR, this is also true for the field at this epoch (Cullen et al. 2014). We also note that investigation in an intra-cluster environment context indicates differences between the regions when combining the two clusters in our sample. XMM2215 shows tentative evidence that the more recent additions to the cluster in the backsplash region have a smaller deviation from the Mannucci et al. (2010) FMR compared to the more established galaxies in the virialised core. This contrasts to the picture seen in XMM2235 as there is little difference in the galaxies present in the core vs the backsplash region.

4.5 Conclusions

In this work we study the environmental dependence of the gas phase metallicity of star-forming cluster galaxies at $z \sim 1.4$. Our findings are summarised as follows:

(i) We found that our combined cluster galaxy sample shows an enhancement in metallicity for a given stellar mass when compared to the MZR relationship from a comparable redshift ($z \sim 1.4$, Yabe et al. 2012) at $\Delta(\mathrm{O/H}) = 0.09 \pm 0.03$ dex. This global result is close to that found in Maier et al. (2019) and would seem to agree with their interpretation of stripped halo gas causing strangulation.

(ii) Comparing the MZR relationship from Yabe et al. (2012) to our clusters individually we see that XMM2215 is driving this metallicity enhancement at $\Delta(\mathrm{O/H}) = 0.16 \pm 0.03$ dex compared to $\Delta(\mathrm{O/H}) = 0.01 \pm 0.03$ dex for XMM2235, perhaps indicating cluster to cluster variation but also adding to the contradictory literature (Kacprzak et al. 2015).

(iii) Assuming the points made in (i) and (ii), while there may be an environmental dependence on MZR (cluster vs field), there may also be a difference between intra-cluster regions when comparing to an MZR from field galaxy samples. This could perhaps indicate that more recently accreted galaxies are more metal rich which may contradict the interpretation of the results from Maier et al. (2019). Alternatively it could that the line-ratios do not reflect metallicity and galaxies in the backsplash region are actually undergoing shocks due to RPS. This result is not statistically significant and more data is needed to determine if it is.

(iv) When assessing comparisons of the FMR to work on field galaxies from Mannucci et al. (2010) we found a global deficit of metallcity compared to their FMR of $\Delta(\mathrm{O/H}) = -0.28 \pm 0.03$ dex.

(v) From (ii) we see that for XMM2215 there is an intra-cluster environment dependence on the deviation of our galaxy sample from the FMR derived from field galaxies in Mannucci et al. (2010). This shows that galaxies within the virialised core of XMM2215 see the greatest deviation ($\Delta(\mathrm{O/H}) = -0.26 \pm 0.03$) compared to the backsplash region ($\Delta(\mathrm{O/H}) = -0.13 \pm 0.05$). This may be due to these galaxies greater time spent within the cluster environment causing a different evolution taking place in the FMR compared to field galaxies. This may also be an indicator that the denser the environment the greater the deviation from field galaxy relationships.

Chapter 5

A Brightest Cluster Galaxy at $z \sim 1.46$

Overview

Here we investigate the role of a BCG in a galaxy cluster in more detail and assess the formation of these massive galaxies while discussing their evolution through cosmic time. We take this theoretical background and compare against the observations taken with VLT/KMOS and *HST*/WFC3 of the galaxy cluster XMM2215 at $z \sim 1.46$. These observations are of a potentially forming BCG present in this highly active galaxy cluster. The forming BCG is indicated by a starbursting, up to four component merger in a cluster that otherwise has no unambiguous BCG. We kinematically assessed two of these components alongside their morphologies coupled with the photometric properties of all four close components. We also discuss the nature of an established BCG at $z \sim 1.4$ as a potential cD type galaxy and what this means in terms of formation times of this unique galaxy type.

5.1 Brightest Cluster Galaxies

Galaxy clusters are the most massive gravitationally bound structures in the Universe and are crucial to our understanding of the evolution of the Universe. These structures also play host to the most massive galaxies in the Universe, found in most low redshift relaxed clusters. These Brightest Cluster Galaxies (BCGs) have been discussed for their role in defining the cluster centre in this work so far (see section 3.3.4 for a discussion of this in the context of two galaxy clusters from this work), but they are of great interest in their own right. These massive galaxies are the most massive concentrations of stars found anywhere in the Universe often having stellar masses of the order $10^{11}\mathrm{M}_{\odot}$. They posses extended light profiles that often overlap with the intra-cluster light (ICL) of the wider cluster (Montenegro-Taborda et al. 2023; Stott et al. 2011; Zwicky 1951). BCGs also often contain radio AGN that are powerful enough to prevent gas cooling in the cluster core (Fabian 2012). BCGs have been used as test of hierarchical merging and monolithic collapse models due to their suspected evolutionary link to their host cluster (Collins et al. 2009; De Lucia & Blaizot 2007; Dressler 1984; Ebeling et al. 2021; Lauer et al. 2014; Stott et al. 2010). In addition to these points of interest they have been used as a tool to locate galaxy clusters beyond those methods outlined in the introduction to this thesis by using the BCG as an anchor to red-sequence fitting to not only to robustly locate but also centre detected galaxy clusters (Koester et al. 2007). These galaxies are also sometimes located very close to the centre of the gravitational potential well which may cause a close evolution of these galaxies alongside their host clusters (Albert, White & Morgan 1977; Cerulo, Orellana & Covone 2019; Joo & Jee 2023; Kluge et al. 2020; Merritt 1984).

In the context of the work presented in this thesis the definition of the galaxy cluster centre is important. One possible cluster centre comes from the X-ray emission centroid arising from bremstrahlung emission of the hot intra-cluster gas. This X-ray emission has therefore been used for many discovery detections of galaxy clusters (Böhringer et al. 2004; Ebeling et al. 1998; Jansen et al. 2001; Sarazin 1986; van Weeren et al. 2019; Weisskopf et al. 2000). We often see the X-ray gas emission in clusters as clumped when more highly spatially resolved, this can be seen in figure 1.3 and could cause unreliability of using this emission as the galaxy cluster centroid. BCGs are also useful for determining the galaxy cluster centroid. We see observationally that the cores of

galaxy clusters predominantly contain massive and highly luminous galaxies. This link to the core region of galaxy clusters and their small relative offset to the X-ray emission peak makes the brightest of these galaxies a good approximation to the centroid of the cluster (Jones & Forman 1984; Montenegro-Taborda et al. 2023).

5.2 Formation and evolution

The formation mechanisms of BCGs have been a widely studied topic since they were found to be atypical compared to the rest of their cluster counterparts (Jones & Forman 1984). These galaxies do not follow the luminosity profiles expected for other cluster ellipticals or bright galaxies which suggests the evolution of these galaxies do not follow the same path as other similar populations (De Lucia & Blaizot 2007).

Multiple formation mechanisms have been investigated via numerical simulation, semi-analytical models, and direct observation. These galaxies may have accrued their stellar mass by rapid cooling of the core X-ray gas halo and subsequent gravitational collapse (Silk 1976). Clearly this method would cause a monolithic structure of stellar mass but has subsequently been unable to be confirmed by observation. Galactic cannibalism was proposed to build the mass of BCGs by dynamical friction (the drag caused by moving through a high mass/gravity system causing the loss of angular momentum) and tidal stripping (Ostriker & Tremaine 1975).

However, more recent work such as that conducted with the Millennium Simulation (Springel et al. 2005), have provided evidence to contradict these theories (De Lucia & Blaizot 2007; Patrick Henry et al. 2010; van Dokkum et al. 2001) in favour of mass accretion from repeated complicated merger events. These complicated histories make untangling the formation of BCGs difficult but an area of great interest. It is now widely accepted that galaxy clusters form through this hierarchical mechanism of successive mergers (Davis et al. 1985), reinforced by work carried out with KCS (Prichard et al. 2017) in addition to other works on merging galaxy clusters and groups (Breuer et al. 2020; Markevitch et al. 2002; Sarkar et al. 2023). As with the clusters themselves it is thought that the BCGs of galaxy clusters form in a similar hierarchical way. This suggests that the host cluster and its BCG co-evolve (De Lucia & Blaizot 2007; Dressler

1984; Ebeling et al. 2021; Lauer et al. 2014) however, how closely this is linked is still uncertain.

Work has since been carried out that has indicated this pure hierarchical merger paradigm proposed in De Lucia & Blaizot (2007) cannot explain the mass build-up of BCGs (Collins et al. 2009; Stott et al. 2010). In order to investigate and reach this conclusion Collins et al. (2009) collected a sample of X-ray emitting BCGs between redshifts $1.2 - 1.5$, indeed two of the clusters in their sample include the two galaxy clusters focused on in this work although we should note the BCG of XMM2235 is not included in the sample of this thesis as it does not exhibit Hα emission in our data that reaches a S/N threshold of ~ 5, see figure 2.6 for our targets. They then compare the stellar evolution models of De Lucia & Blaizot (2007) with the BCGs in their sample and note that they have consistently higher stellar mass than that of the models at a comparable z, this key result can be seen in figure 5.1. This leads to the conclusion that the majority of the mass build-up in forming BCGs happens very rapidly at earlier times than predicted previously, these massive galaxies then proceed to much more slowly increase stellar mass to lower redshift.

This work is expanded upon in Stott et al. (2010) where the sample size is increase from five galaxy clusters to twenty. They select BCGs not only with visual inspection but by identifying the tip of the red-sequence and selecting the brightest galaxy in K_s-band magnitude within 500 k pc of the cluster center, which is determined as the X-ray emission centroid. As noted in this thesis they also indicate that the identified BCG for XMM2215 is more ambiguous and we discuss this in greater detail in section 5.4 later in this chapter. The conclusion from Stott et al. (2010) contradicts the dry hierarchical merger theory presented with the Millennium Simulation (De Lucia & Blaizot 2007) and favours more of a build-up from the classic theory of monolithic collapse of the Intra-cluster medium (ICM; Silk 1976) to account for the short time-scale of stellar mass increase. This finding could be due to purely a selection effect as the $z > 1$ cluster sample is biased towards the most massive clusters at that epoch. In addition, the simulated BCGs seem to match observations of luminous red galaxies and the selection in Collins et al. 2009 and Stott et al. 2010 prefer more massive BCGs and so the hierarchical model may just not be apt for this more massive subset.

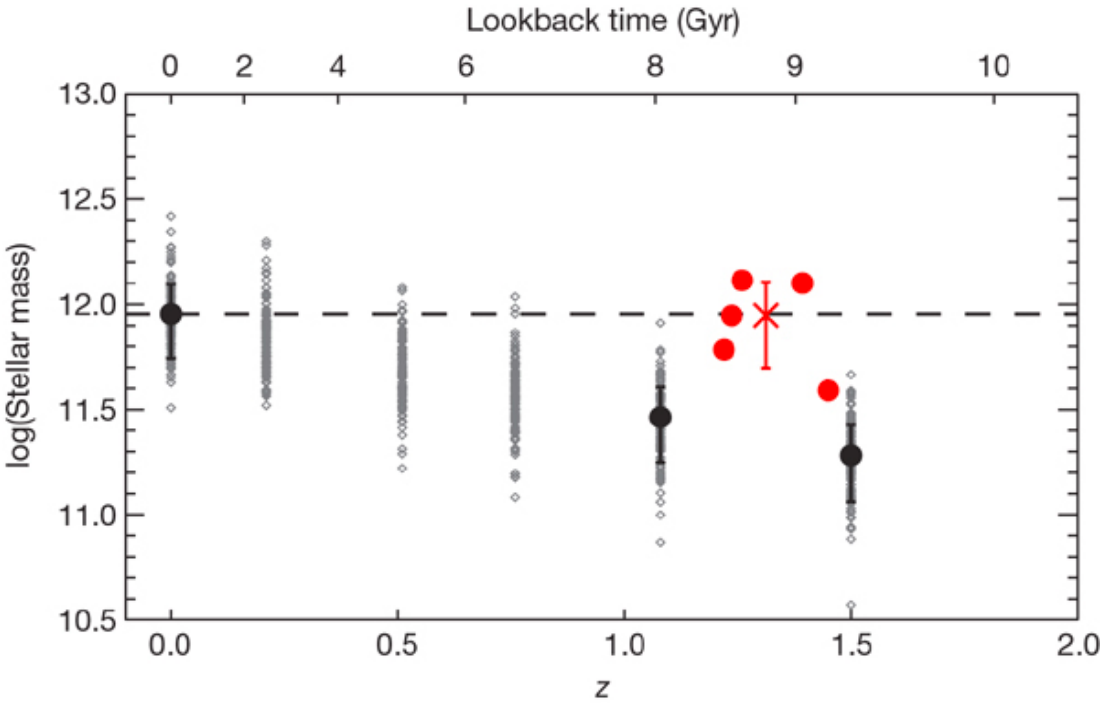

Figure 5.1: Screenshot of figure from Collins et al. (2009) where we see that high redshift BCGs have similar masses to their local counterparts. This appears to disagree with mass evolution from dry merger events. The red points are the BCG mass measurements for the sample normalised to $z = 0.04$, indicated by the black dashed line and the black points indicate the predicted BCG masses from the millennium simulation.

5.2.1 cD galaxies

As discussed briefly in the introduction to this thesis, cD galaxies are the largest galaxies in the known populations. They are a unique class of galaxy often found to be the BCG of relaxed clusters, large in terms of stellar mass and radius of material contained within them (Matthews, Morgan & Schmidt 1964; Newman et al. 2013; Oemler A. 1976; Schombert 1986). As such they typically have large Sérsic indices coupled with a large stellar mass and extended diffuse emission. This emission is often coupled with the emission of the larger ICL of the host cluster which further complicates the investigation of each. The ICL is an extended diffuse region of light from stars that are not associated with a specific cluster member. Previous work has indicated that ICL presence at $z > 1$ is much lower than that of low redshift clusters both theoretically and observationally (Contini et al. 2014; Rudick, Mihos & McBride 2011; Stott et al.

2011). However very few observational studies have included these higher redshift galaxy clusters but work in Joo & Jee (2023) using a sample of 10 galaxy clusters at $1 < z < 2$ show that a significant fraction of ICL already exists perhaps indicating that the ICL is formed alongside the growth of BCGs.

Study of cD galaxies may also help to untangle the problem of BCG stellar mass assembly over cosmic time-scales. This is due to cD galaxies being present in dense galaxy groups (Albert, White & Morgan 1977; Merritt 1984) and also during cluster mergers and during the stage of cluster virialisation (Kluge et al. 2020). It is through this range of extreme cases we can learn more about how these galaxies are co-evolving with their cluster hosts and begin to untangle the complex evolution of BCGs (Ebeling et al. 2021).

A large volume study of cD galaxies is difficult as they are not present in all $z > 1$ galaxy clusters and when they are there is only one. Therefore, as with most galaxy cluster analyses, we do not have the statistical power that we see in field galaxy studies. Work carried out on these galaxies demonstrates that they are essentially at rest with respect to the gravitational potential of their host cluster but that repeated merger events can cause displacements (De Propris et al. 2021).

As demonstrated so far in this work IFUs are a powerful tool of study. Work carried out in Johnston, Merrifield & Aragón-Salamanca (2018) demonstrates the suitability of IFUs in investigating cD galaxies. The work makes use of the Multi-Unit Spectroscopic Explorer (MUSE) instrument on the VLT, a monolithic IFU with a field of view of $1'$ and a spatial resolution of $0.2''$/pixel. As cD galaxies contain an extended emission envelope it is important to determine if these components evolved together or are the result of two galaxy cluster components coalescing. In order to assess this the components must be spectroscopically spatially resolved and separated in order to be investigated independently. This study uses observations of a single cD galaxy as a pilot to demonstrate the utility of this data and the robustness of the techniques outlined. Despite this single galaxy sample they are able to demonstrate they can recover similar conclusions to other studies of this galaxy (Arnaboldi et al. 2012; Barbosa et al. 2018, 2016; Coccato et al. 2011) and that the utility in this method is the ability to use lower quality data cubes to obtain robust results. Beyond this work IFS data can investigate these galaxies in similar ways as carried out within this thesis. By spatially resolving key emission lines of the gas content of this special type of massive galaxy we could

determine if the internal kinematics of these galaxies are special or even potentially untangle merger history.

5.2.2 Evolution

Observationally, BCGs do not appear to follow a single pattern of mass build-up from formation throughout their evolution. Following this initial rapid mass build-up, BCGs are believed to continue their evolution through a series of smaller minor merger events (Collins et al. 2009; De Lucia & Blaizot 2007; Stott et al. 2010). This assumption is made as the stellar mass increase in these galaxies cannot be purely explained by raw conversion of gas into stars (Webb et al. 2015). However, there is contradictory work to suggest a stronger evolution over cosmic time-scales (Lidman et al. 2012; Zhang et al. 2016).

The work carried out in Lidman et al. (2012) uses a sample of 160 BCGs between redshift 0.03 and 1.63. They identify their BCG sample by the brightest K_s-band magnitude cluster member, which are typically the galaxy closest to the cluster centre, with few exceptions. The final result of this work is that while the semi-analytical models from De Lucia & Blaizot (2007) predict that the stellar mass should increase by a factor of 3 between $z \sim 0.9 - 0.2$ they find that it is closer to 1.8 ± 0.3. This therefore does not agree perfectly with predictions but does still indicate an evolution over longer cosmic times not just in the short time-scale preferred in Collins et al. (2009) and Stott et al. (2010). They explain a possibility for this evolution is subtleties in the analysis that include; matching clusters to their mass equivalent at current time and definition differences in the redshift intervals used to define the "low-redshift" sample. Work in Zhang et al. (2016) attempts to address this tension through analysis of observational data alongside matching simulations using a more refined comparison between model and observations at a range of redshifts. This method produces a result of an increase in intracluster light (ICL) after $z \sim 1$ to reduce the tension in the rate of stellar mass build-up in BCGs. This increase in ICL is caused by the stellar mass accretion from repeated mergers being scattered throughout the intracluster space surrounding the BCG (Contini et al. 2014). It is possible to conclude from all of the work carried out in BCG evolution and formation that careful consideration should be made when comparing data across redshift ranges, as ideally we would trace individual BCGs

through their track of evolution. As this is not possible in observation comparisons of different BCGs across a range of redshifts must be made but these BCGs must have similar histories in order for this method to be valid.

Another way of reducing the impacts of biases in samples is to use statistically large samples to say something about the global populations of BCGs. Work carried out tracks the evolution of BCGs using large sample sizes across a range of redshifts. Many of these samples come from cosmological simulations (e.g. Bahé et al. 2017; Henden, Puchwein & Sijacki 2020; Montenegro-Taborda et al. 2023 but work has also been performed in observation as in Orellana-González et al. (2022).

Orellana-González et al. (2022) utilises a large sample of BCGs in the redshift range of $0.05 - 0.42$ of $\sim 56\,000$ galaxies from SDSS and *WISE*. Their sample consists of photometry from the optical Sloan bands for the SDSS data including the spectroscopic redshifts from SDSS Data Release 12 (DR12). The data from *WISE* includes the near-to-mid-infrared photometry across four photometric bands. Both of these datasets are put into the SED fitting routine Code Investigating GAlaxy Emission (CIGALE; Boquien et al. 2019) in order to determine unresolved properties of the sample of BCGs. Based on this data they conclude that comparing to predictive models previously published suggests that the change of star-formation mode from merger dominated to ICM-cooling dominated happens after $z \sim 0.6$. As a whole this work is able to demonstrate that star-forming BCGs are not rare but often sit below the SFMS of comparable star-forming field galaxies. Even though a statistically large sample of galaxies is used, a work of this size is still unable to define the mode of stellar mass assemblage across the lifetime of a BCG and remains an open question for current and future studies.

The differences we see in BCGs and the questions about their mass accretion histories may be answered by investigating the cooling and feedback mechanisms of the BCGs and their immediate environment. We have already drawn a link between the evolution of these galaxies and their host clusters and the link between a BCG and the ICL, it therefore stands to reason that their mass evolution would be impacted by this interplay. Work has been carried out to investigate this link on a statistically large dataset in Cerulo, Orellana & Covone (2019). They use a sample of low z BCGs ($0.05 \leq z < 0.35$) consisting of approximately $20\,000$ sources from SDSS and WISE with a halo mass range of $6 \times 10^{13}\,\mathrm{M}_{\odot} - 10^{15.5}\,\mathrm{M}_{\odot}$. Assessing the SFR of this sample of BCGs they note that only $\sim 9\,\%$ of the sample are star-forming. The number of BCGs

that are star-forming tend to greater percentages at higher redshifts but also decrease with increasing cluster and BCG mass. Upon investigating the interaction of the host cluster and BCG they find that while star-forming BCGs can be found across cool and non-cool core clusters, quiescent galaxies are dominant in non-cool core clusters, leading to the conclusion that cool clusters are able to provide mass to be used for star-formation within their BCGs.

5.2.3 An example BCG forming at $z \sim 3$

Work carried out in Kubo et al. (2021) presents the progenitor of a BCG with plausible merging counterparts which further supports the theory of hierarchical formation. This central galaxy is located in protocluster SSA22 at $z \sim 3.09$ and is a massive galaxy, their work shows that star-formation has been rapidly quenched and then suppressed. This galaxy will merge with other massive SMGs within the quenched time-scale, according to predictive simulations. Such merger candidates have been confirmed with two identified as showing possible interactions with the candidate BCG.

This discovery combines direct spectroscopic observation with Multi-Object Spectrometer For InfraRed Exploration (MOSFIRE) on the Keck I telescope in K_s- and H-band (NIR), deep K-band imaging with the Multi-Object InfraRed Camera and Spectrograph (MOIRCS) on the Subaru telescope. Using this combination of data sources and a range of spectral energy distribution (SED) modelling they were able to determine that rapid quenching occurred 0.6 Gyr prior to epoch of observation, reinforced through multiple modelling of the SFH. In order for this result to be valid, substantial feedback would be required, potentially from young massive stars and AGN. This SFH would indicate and provide further evidence that massive SMGs could be progenitors of this potential BCG. This galaxy also lies within a dense group of SMGs providing further evidence of the hierarchical model of BCG and giant elliptical galaxy formation. The authors note that they are currently unable to explain how the BCG in formation is remaining quenched over long time-scales when its environment is very conducive to further star-formation.

5.2.4 Dumbbell galaxies

As cD galaxies form a special case of a late-type BCG, so called 'Dumbbell galaxies' form a special case of the early stage of BCG formation and are especially interesting as an evolutionary indicator (Pimbblet 2008). These systems are essentially merging galaxy groups within clusters and, within this context, will likely go on to form large BCGs when relaxed. The simplest definition of these galaxies are two galaxies of similar magnitude, within a common stellar halo (Gregorini et al. 1994, 1992). Beyond these definitions dumbbell galaxies are interesting in the context of galaxy cluster formation and evolution as their presence within a cluster holds clues about its history (Bilton et al. 2019; Pimbblet 2008). An extensive amount of work has indicated that these dumbbell BCG systems, that often possess high peculiar velocities with respect to the cluster kinematic centre, are evidence of cluster merging and are a product of multiple cluster cores merging into a new gravitational potential well (Caglar & Hudaverdi 2017; Pimbblet, Roseboom & Doyle 2006; Quintana, Ramirez & Way 1996). Their presence within a large number of galaxy clusters is therefore also further evidence for a hierarchical mode of galaxy cluster and BCG formation (Bilton et al. 2019; Pimbblet 2008), the number of detections is also beyond coincidental with work carried out to remove potential observational and sample biases from detections of these galaxy systems (Gregorini et al. 1994, 1992).

Beyond the simplistic observational definition of these systems it is possible to determine their existence as mergers kinematically and by extension the potential merger history of the galaxy cluster itself. Work from Bilton et al. (2019) compares observational data with simulated merging scenarios to determine if this link can be made reliably. They find that comparing the rotational velocities of the blue and red galaxy populations across a range of r/r_{200} we see a bimodal distribution peaking within $0.5r/r_{200}$ and then again beyond this which indicates a mixing process of two cluster cores interacting. This again provides further evidence to the hierarchical model of galaxy cluster evolution. This is further evidenced by the large peculiar velocities of these dumbbell systems in the rest-frame of the cluster showing two originally independent groups of galaxies merging.

5.3 Analysis and Results

5.3.1 A cD-type BCG at $z = 1.4$

Work carried out for this thesis involved the investigation of two BCGs, one of which is more evolved located in the center of the cluster XMM2235. This BCG did not demonstrate appreciable Hα emission and indicates this galaxy is now passive and not forming stars. This galaxy is also massive ($\log_{10}(\mathrm{M/M}_{\odot}) \simeq 11.75 \pm 0.19$) where only one other galaxy demonstrates a stellar mass of this order of magnitude in the entire of the galaxy sample across the two clusters (XMM2235_IFU2) which demonstrates properties of an AGN and so its stellar mass is suspect. It should be noted that another property of the BCG of XMM2235 is that of a highly extended envelope of diffuse emission. This is another property of cD galaxies but also makes an accurate calculation of its stellar mass difficult. Fitting a single Sérsic profile using GALFIT following the same analysis outlined in chapter 3 demonstrates an $n \sim 7$ and an extreme effective radius. It is best to use a morphological fit of two Sérsic profiles when modelling such a galaxy but we are unable to do so successfully because of our spatial resolution limit and the highly diffuse nature of the associated halo/ICL. In addition, confusion with the galaxy ICL would also interfere with interpretation of our results as noted in Kluge et al. (2020). Large numbers of these galaxies can be seen in the nearby Universe but very few have been studied at higher redshifts due to observational constraints (Liu et al. 2013, 2008). However, work presented in Liu et al. (2013) shows a cD galaxy at $z \sim 1.096$ demonstrating that these galaxies can in fact form early. If the BCG of XMM2235 were indeed a cD galaxy it would provide evidence that cD galaxies can form at higher redshift, as predicted by simulations in Laporte et al. (2013), but how early these galaxies can form remains difficult to determine observationally.

5.4 Witnessing the potential formation of a BCG

Dusty star-forming galaxies at $z \sim 2$ are thought to be the progenitors of today's giant elliptical galaxies (Casey et al. 2013; Holland et al. 1999; Kubo et al. 2021). Following work presented in chapter 3 of this thesis, XMM2215 has no obvious BCG (Stott et al. 2010) but does contain a merger of 2-4 galaxies near its core, of which at least two of

the components are associated with a strong sub-mm and mid-infrared source (Hilton et al. 2010; Ma et al. 2015). We therefore speculate that this merger represents the formation of a BCG. In this study we targeted the two merging galaxies most closely associated with the sub-mm source with one of the KMOS IFUs. These galaxies were not confirmed as cluster members in previous optical spectroscopy as they were too dusty to obtain reliable spectra from [OII]. Here we used near-infrared-observed Hα to confirm that they are indeed cluster members, as can be seen in figure 3.17, where they were considered as one single object (see below). When taken as a single object it was found to have a velocity offset of $1219.8 \pm 34.3\,\mathrm{km\,s^{-1}}$ compared with the cluster velocity centroid. We can see from figure 3.16 (top panel) that XMM2215 has a wide distribution of redshifts, demonstrating its relative dynamical youth so this is perhaps unsurprising. Also, some more mature BCGs in local clusters are found to have large velocity offsets with respect to their clusters so this does not rule out our interpretation (De Propris et al. 2019).

To probe the kinematics of this multi-component system we first collapsed the KMOS H-band cube along the spectral axis, with the Hα and [NII] window removed and the skyline regions masked, to obtain a stellar continuum image. This is shown on the lower left panel of figure 5.2. This continuum map displays two peaks that we shift spatially to correspond closely to the locations of the emission peaks in the F160W imaging, as seen with the red contours. The shift was performed to align the KMOS IFU with the *HST* data. The F160W image, shown in the lower right panel of figure 5.2, indicates a merger is taking place as the galaxies appear distorted with bright "heads" at their region of closest approach and fainter "tails" trailing away.

To extract the spectra of the merging components (A and B, as indicated in figure 5.2), we placed apertures on the data cube centred on the two peaks of emission of the F160W imaging. These apertures were consistent with the width of the seeing disc ($0''.7$) and produced the 1D spectra shown in figure 5.3. Upon fitting a single Gaussian to the Hα emission line using the same methodology as in section 3.2.1, we calculated their redshifts and therefore their relative velocities. The global properties of these two galaxies can be found in table 5.1 and we note that the B component has a higher velocity relative to the cluster centre and similar stellar mass to component A. The relative velocity between the components A and B is $209.6 \pm 50.2\,\mathrm{km\,s^{-1}}$, and separation of $9.1\,\mathrm{kpc}$ which indicates that they are likely to merge (Patton et al. 2000).

Although these galaxies are clearly separated from the cluster core in velocity space, this low relative velocity could demonstrate that these galaxies are interacting with each other, if not yet merging.

The stellar masses of the merging components A and B are given in table 5.1 along with the masses of the other 2 nearby galaxies, for which we do not have spectra and therefore velocity information (C and D, see figure 5.2 upper panel). If a merger occurs the stellar masses of components A and B sum to $\log_{10}(\mathrm{M/M}_{\odot}) = 10.93$. This increases to $\log_{10}(\mathrm{M/M}_{\odot}) = 11.51$ if the current SFR $= 240\,M_{\odot}\,\mathrm{yr}^{-1}$ continues for 1 Gyr. If all four components merge, without accounting for star formation then the total mass is $\log_{10}(\mathrm{M/M}_{\odot}) = 11.12$. Finally if all four components merge and we include the additional mass from star formation then the total stellar mass is $\log_{10}(\mathrm{M/M}_{\odot}) = 11.57$. These masses of $\log_{10}(\mathrm{M/M}_{\odot}) \geq 11$ are clearly in the BCG regime, especially at this epoch. We therefore conclude that this dusty star-forming merger is a potential forming BCG. We also place these components in their relative velocity and physical positions relative to BCG_A in order to illustrate their merging potential, see figure 5.4.

Based on previous work from Pimbblet (2008) and Bilton et al. (2019) we attempted to determine if this system can be classified as a dumbbell BCG system. The simplest method is through qualitative assessment and comparing the magnitudes of the main merging components BCG_A and BCG_B, 21.478 mag and 21.481 mag respectively. Looking at the imaging of these two components it was possible to see that they likely reside within a common stellar halo and have possibly previously gravitationally interacted based on the displaced nature of their diffuse emission with respect to the location of their emission peaked cores, see figure 5.2. As the magnitudes of BCG_A and BCG_B are also very similar we could determine these two galaxies form part of the dumbbell based on these two assessments. Their peculiar velocities, quoted in table 5.1, are also very similar and have previously been shown as potential mergers in this section. Based on metrics stated in Pimbblet (2008) we could also say that, although there may be exceptions for which they note one in their sample, a dumbbell system will typically not have components in them that have peculiar velocities greater than 1.1 times the velocity dispersion of the host cluster, determined to be 777.77 km s^{-1} for XMM2215. These two galaxies are clearly outside of that range (see table 5.1) and if are to be classified as a dumbbell would reside in an exceptional group, as the single outlier from Pimbblet (2008), despite qualitatively sharing a common stellar halo.

Table 5.1: The coordinates alongside the velocity and stellar mass information for the four components of the potential BCG merger in XMM2215.

BCG Component	RA (^{o})	DEC (^{o})	v_{gal} (km s^{-1})	$\log_{10}(M_*/M_\odot)$
BCG_A (NE)	333.99870	-17.63298	1211.0 ± 34.0	10.63 ± 0.20
BCG_B (SE)	333.99862	-17.63325	1420.0 ± 50.0	10.62 ± 0.20
BCG_C (NW)	333.99941	-17.63310	$-$	10.51 ± 0.20
BCG_D (SW)	333.99925	-17.63345	$-$	10.15 ± 0.20

Despite this ambiguous result we return to the assessment of the cluster kinematics presented in figure 3.16. This distribution of redshift values for the passive and star-forming galaxies within XMM2215 would seem to indicate there may be two merging galaxy cluster components along the line of sight. This is indicated by the peak at $z = 1.452$ which gradually tails off to $z = 1.47$. There may also be a second peak at $z = 1.458$ lending more weight to this argument but we note that the number counts of galaxies in these bins are low and a larger sample would be needed to definitively make this assertion.

5.5 Conclusions

The BCG in XMM2235 was found to be a cD-type galaxy due to its extended emission envelope and high Sérsic index ($n \sim 7$). cD galaxies have been shown to exist at $z > 1$ but this would show that this unique galaxy type may well be present at redshifts higher than have currently been detected (Laporte et al. 2013; Liu et al. 2013, 2008). It is difficult to robustly define the morphological properties of this BCG due to the extended emission profile that may also include interference from developed ICL in its host galaxy cluster.

We found strong evidence from the relative velocities and imaging that a 2-4 galaxy merger is associated with a bright sub-mm and mid-IR source within the cluster. The total stellar mass of various outcomes for this system put it well within the BCG range, particularly at this epoch. The system is offset from the velocity centre of the cluster but this is not unusual for a BCG, especially in what is likely an un-relaxed cluster (De Propris et al. 2019). This is therefore a strong candidate for a BCG caught in the act of formation and adds to the growing body of evidence that sub-mm galaxies are the

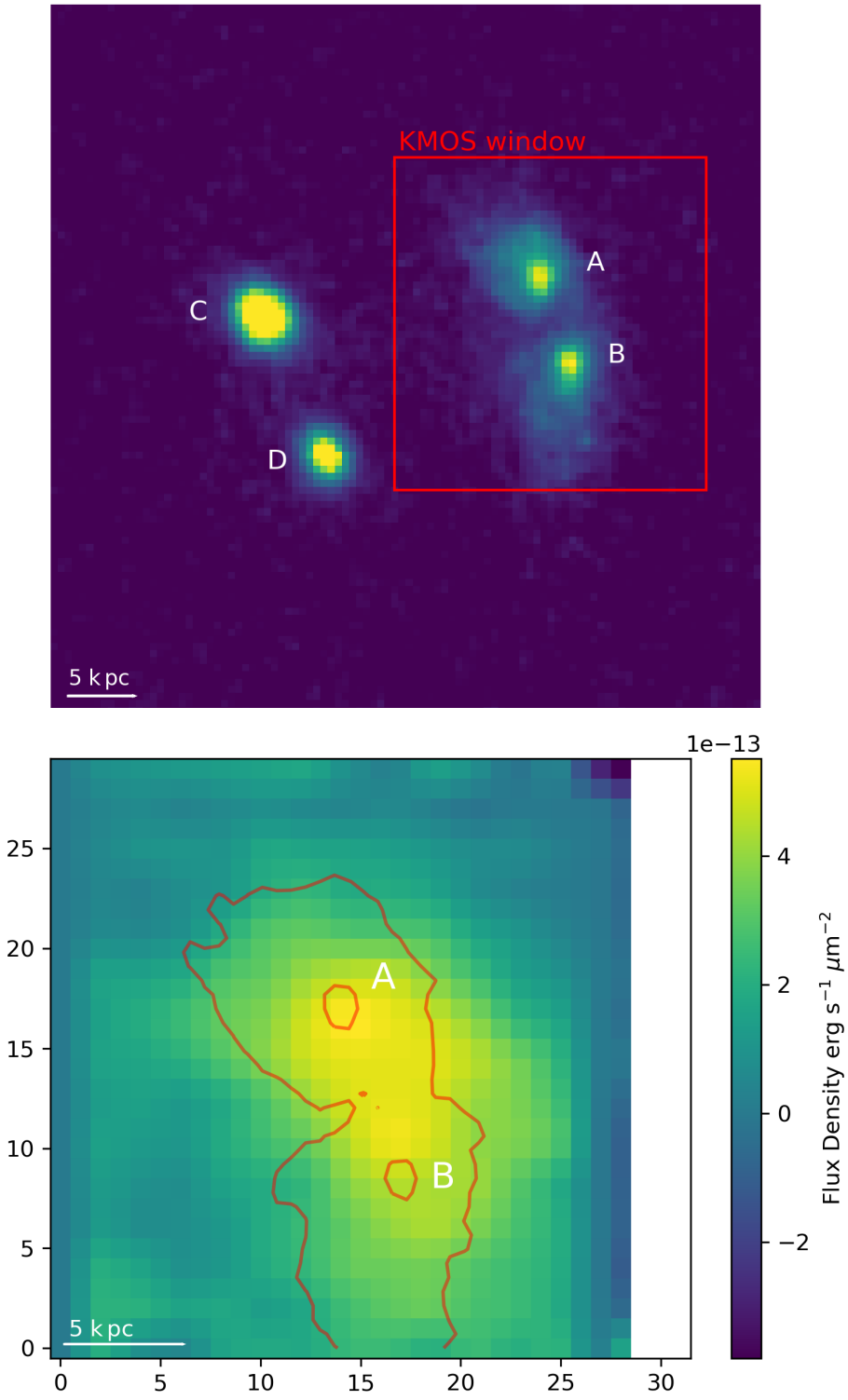

Figure 5.2: *top*: *HST*/WFC3 F160W image of four component system of a potentially forming BCG for XMM2215. *bottom*: Continuum map for XMM2215_IFU18 with imaging contours in red.

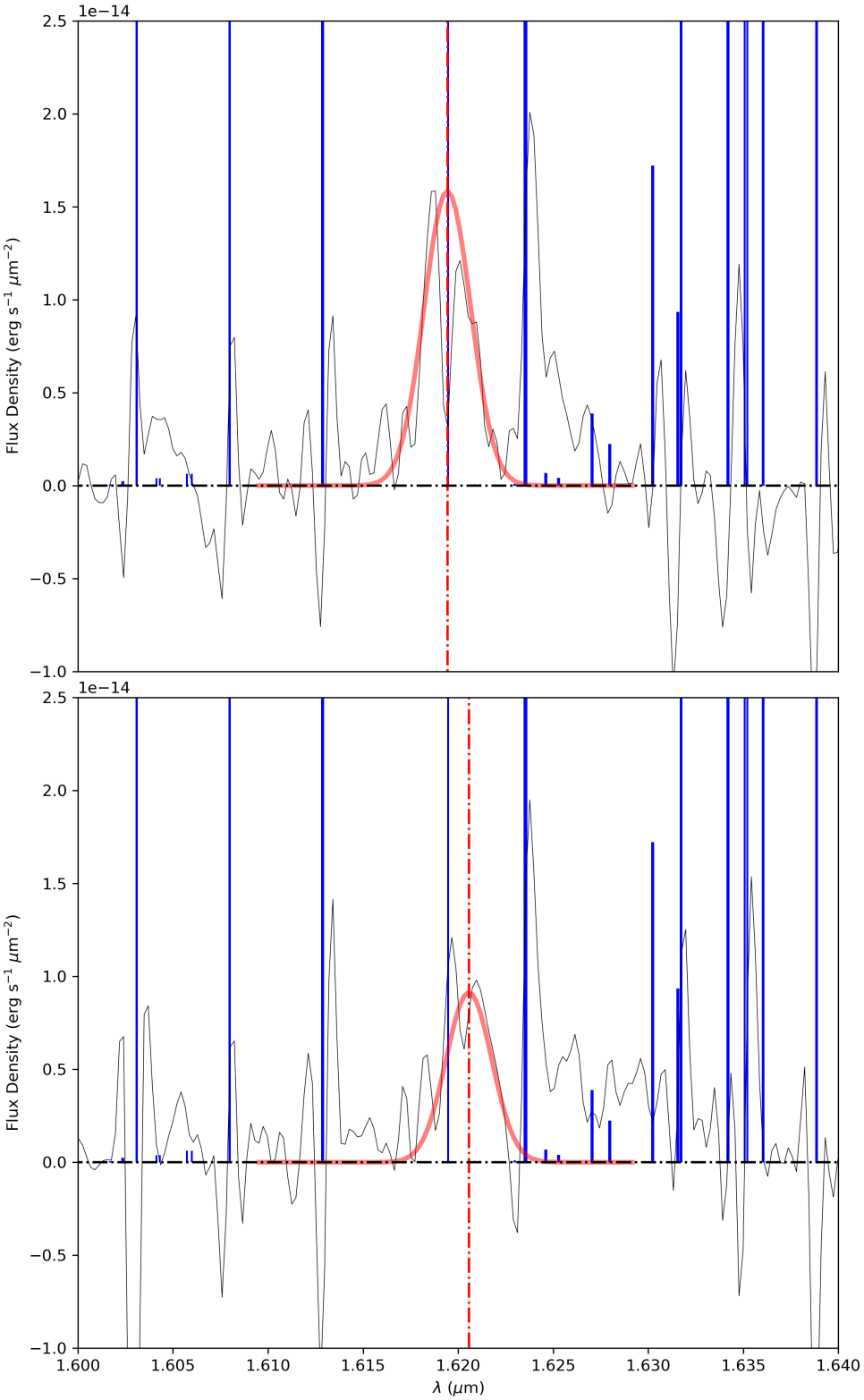

Figure 5.3: *top*: 1D spectrum of BCG component A of XMM2215 extracted and fit with a single Gaussian. *bottom*: The spectrum and fit to component B. See figure 3.1 for line description.

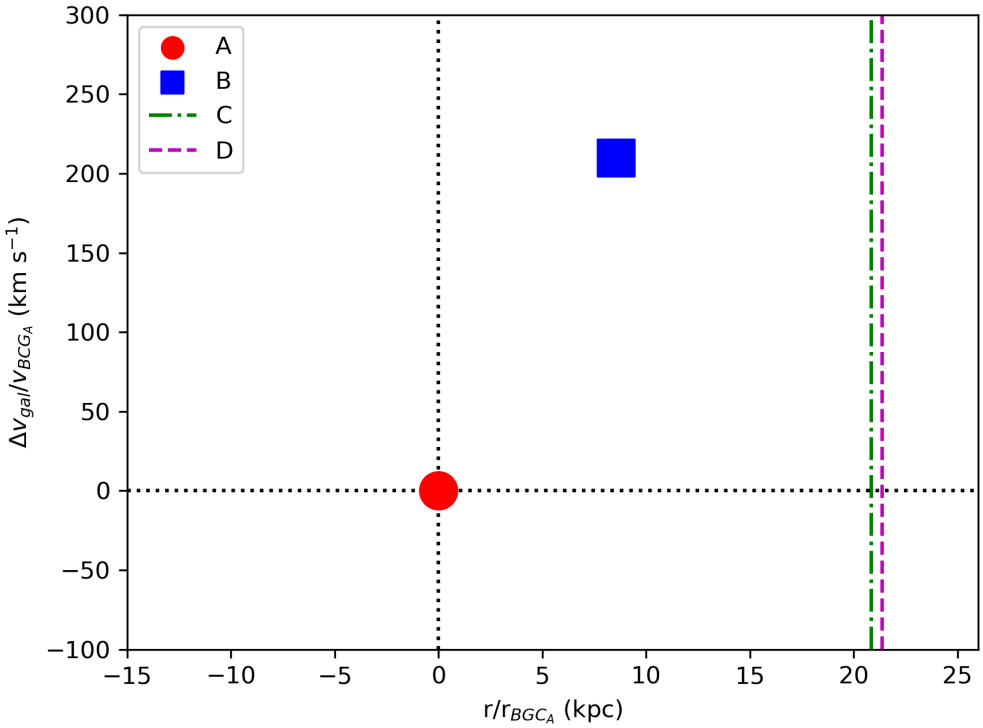

Figure 5.4: BCG components A, B, C, and D for cluster XMM2215 in the positional and kinematic context of the dominant BCG component BCG_A. Components C and D are presented as vertical lines at their relative distances from component A because no velocity data is available for these two galaxies.

progenitors of local massive ellipticals (Casey et al. 2013; Holland et al. 1999). It also gives strong support for hierarchical merging being the formation mechanism of BCGs, in agreement with De Lucia & Blaizot (2007). While this BCG may qualitatively be assessed in imaging as a potential dumbbell system, when assessing the kinematics of the two major components of this system the determination is less clear and if this were a dumbbell system it would likely be exceptional compared to current datasets. However, when assessing the kinematics of the passive and star-forming populations of XMM2215 it is possible to see that there may be two merging galaxy cluster components along the line of sight.

Chapter 6

Conclusions

We have presented work outlining the importance of the study of star-forming galaxies in overdense environments at cosmic noon and comparing them to those that are more isolated in order to quantify the impact environment has on galaxy evolution. We also presented work carried out in the course of this thesis on two subtly different galaxy clusters in order to compare the star-forming galaxy populations in both and to the field. This was achieved using a combination of NIR IFS and photometry. We have shown that these galaxies are in many ways similar to those in the field but they also show differences in their metallicity relations and in terms of the morphological impact of environment.

6.1 Spectroscopy and photometry of cluster galaxies at cosmic noon

In chapter 3 of this work we presented spatially resolved spectroscopy alongside complimentary NIR photometry of 24 galaxies in the two overdensities of XMM2215 ($z \sim 1.46$) and XMM2235 ($z \sim 1.39$). We found that these galaxies largely show no significant difference between their counterparts in the field. This is demonstrated by the location of the star-formation main-sequence of these galaxies occupying the same region of parameter space as field galaxies from CANDELS at $z \sim 1.4 - 1.5$.

When assessing for potential offset between the morphological and kinematic major axes ($|\sin(\mathrm{PA}_{im} - \mathrm{PA}_{kin})|$) and comparing this to sSFR we found that the more disturbed galaxies have a higher sSFR. This is true for both of our clusters but more so for the more active cluster XMM2215. Coupled with this we assessed the kinematics of the gas in these galaxies and found that $< v_{1.5}/\sigma >$ is lower in the cluster environment than local values but agrees well with the field galaxies at this epoch reinforcing the view that turbulent disks are likely driving the high SFR as found in previous field galaxy studies. The dispersion-dominated galaxies within this sample also have large kinematic to morphological axis offsets, providing further evidence of disturbed systems driving star-formation in these galaxy clusters.

Our analysis of the cluster galaxy sample was expanded to cluster phase-space where the intra-cluster environment can be investigated more closely. By including the passive sample of galaxies from previous work with KCS we saw that in XMM2235 the quiescent population live mostly in the core, whereas in XMM2215 they are scattered throughout phase-space. This demonstrates that XMM2235 is the more dynamically relaxed of the two clusters. We also found that galaxies in the core of XMM2215 have higher SFRs that those outside the core further alongside lying above the SFMS relative to the rest of the sample, adding to evidence that XMM2215 is a highly active cluster.

Further differences also emerged when comparing the star-formation properties of these galaxies with their morphologies and placing in the cluster regional context. This showed that galaxies in the core of XMM2235 have higher proportion of rounder galaxies in the core compared to those outside the core of the cluster. This may demonstrate that a morphological transformation precedes reduction in SFR, with morphological quenching a possible cause (Martig et al. 2009). However, our result did not indicate this is statistically significant in our sample and so more data is needed to determine its significance, if any.

We combined our sample with the passive galaxies from KCS to refine the cluster redshifts from the literature with the following updated values: XMM2235 $= 1.3930 \pm 0.0006$ and XMM2215 $= 1.4570 \pm 0.0002$. The virial mass estimator also produced cluster masses of XMM2215 is $2.51 \pm 0.15 \times 10^{14} M_{\odot}$ and for XMM2235 is $8.72 \pm 1.09 \times 10^{14} M_{\odot}$, both masses agree well with the X-ray derived values from the literature indicating the robustness of both methods (Stott et al. 2010).

6.2 The gas-phase metal content of $z \sim 1.4$ cluster galaxies

In chapter 4 of this thesis we presented a study of the environmental dependence of the gas phase metallicity of star-forming cluster galaxies focused on throughout this work. Using the same set of 24 galaxies and building on work presented in chapter 3 of this thesis we demonstrated differences between the field galaxies and star-forming cluster galaxies at this epoch. This was achieved by comparing to derived metallicity relations from field galaxy samples, namely the MZR and FMR. Global differences between these environments were shown, although some of this may be due to cluster to cluster variations. Differences were also found between intra-cluster regions demonstrating not only an environmental impact but a more granular intra-cluster impact.

We found that when taken as a single dataset our galaxy sample showed a metallicity enhancement ($\Delta(\mathrm{O/H}) = 0.09 \pm 0.03$ dex) for a given stellar mass comparing to a field galaxy MZR, derived at this redshift from Yabe et al. (2012). This result would seem to agree with the findings from Maier et al. (2019) who interpret this as being due to environment cutting off the supply of low abundance gas. However, when splitting up by cluster this instead adds to the contradictory literature indicated in Kacprzak et al. (2015). We showed that XMM2215 deviates from the Yabe et al. (2012) relation ($\Delta(\mathrm{O/H}) = 0.16 \pm 0.03$ dex) whereas XMM2235 is largely consistent ($\Delta(\mathrm{O/H}) = 0.01 \pm 0.03$ dex). This indicates there are cluster to cluster variations.

When investigating differences between the intra-cluster regions we showed that the backsplash region demonstrated a greater deviation from the Yabe et al. (2012) MZR compared to the virialised core region. The core agreed with the conclusions from work carried out on a subset of core galaxies in XMM2215 from Maier et al. (2019) but the higher metallicity in the backsplash region complicates the interpretation. This perhaps indicates that more recently captured galaxies are already more metal rich or that the line-ratios here do not actually reflect metallicity but rather the effect of shocks due to RPS. However, as these results did not show a statistical significance these scenarios indicate possible situations if these results were significant, more data is needed to determine this.

We also compared our cluster galaxy sample to an FMR derived from field galaxies in Mannucci et al. (2010) where we found a global metallicity deficit of $\Delta(\mathrm{O/H}) = -0.28 \pm 0.03$ dex. As was shown with our analysis of the MZR we saw that, at least for XMM2215, there was also an intra-cluster environment dependence on the deviation of our galaxy sample from the FMR derived in Mannucci et al. (2010). Galaxies in the core showed the greatest deviation ($\Delta(\mathrm{O/H}) = -0.26 \pm 0.03$) compared to the backsplash region ($\Delta(\mathrm{O/H}) = -0.13 \pm 0.05$). As these core galaxies spent a greater time in the cluster environment a different evolution in the FMR may be taking place compared to that of field galaxies. These changes may also simply indicate that a denser environment causes a greater deviation from a field galaxy FMR.

6.3 The formation and evolution of Brightest cluster galaxies

Expanding on the analysis presented in chapter 3 of this thesis we isolated and assessed a potentially forming BCG in the active galaxy cluster XMM2215. This cluster otherwise has no obvious BCG. We used the relative velocity information of the component galaxies alongside imaging of this 2-4 galaxy merger. This, coupled with association with a bright sub-mm and mid-IR source within the cluster, provided evidence that this is likely a system that will eventually become a massive BCG. By combining the total stellar mass outcomes of various combinations of this system showed it well within the BCG range ($> 10^{11}\mathrm{M}_{\odot}$), particularly at this epoch. The merging components are offset from the velocity centre of XMM2215, but as this is likely an un-relaxed cluster (see figure 3.16) this is not unusual (De Propris et al. 2019), especially considering a BCG in a state of formation. This strong candidate for a forming BCG adds to the increasing volume of evidence that sub-mm galaxies are the progenitors of local massive ellipticals (Casey et al. 2013; Holland et al. 1999). Upon further investigation of the components of this merging BCG we found that it was not likely a dumbbell cluster and there was no evidence of sub-cluster merging.

This serendipitous discovery stood alongside the BCG from XMM2235 which did not display star-formation properties with no Hα emission detected in our analysis.

The BCG in XMM2235 is a characteristic massive BCG with a diffuse elongated cD-like emission, which is rare at these higher redshifts. This may be analogous to the evolutionary end point for the multiple galaxy merger located in XMM2215.

6.4 Future work

Whilst this thesis used the available data in a variety of ways to improve our understanding of cluster galaxies at cosmic noon, there is still more that could be achieved with this existing data before moving on to newer facilities or larger datasets. One such method would be to expand the analysis of metallicity in presented in chapter 4 into a spatially resolved regime. While S/N would impede a line-ratio analysis performed in the same way as the mapping of Hα in chapter 3 of this thesis, it may be possible to improve this by taking several annuli around the define galaxy centroid of the cube summing the flux and fitting the line ratios as in figure 3.1. This will determine if there is evidence for inverted metallicity gradients either indicating efficient fuelling of the centre by low abundance gas or quenching from the outside in. Alternatively, this may be caused by enhancements in outer line-ratios due to shocks on the leading edge of the galaxy which may be an indication it is undergoing RPS. Continued use of KMOS to expand the datasets using techniques outlined in this thesis would also be an excellent option to explore as this would provide clear like for like comparison within larger datasets. Greater use of the spatially resolved Hα emission to determine spatially resolved SFR across individual galaxies within the data could also prove interesting in determining likely quenching scenarios. At the very least this could tell us if these galaxies are quenching from outside in or the opposite by finding an SFR gradient.

Using the current generation of NIR facilities we have investigated the effect the denser cluster environment has on galaxies compared to those that are more isolated in the field. We have demonstrated that we are already pushing the limits of those facilities in terms of spatial resolution and atmospheric contamination in the case of ground based facilities in NIR. This restriction is greatly improved with the recent launch and commissioning of the NIR facilities aboard *JWST*. This removes the atmospheric constraints when observing in NIR bands such as H-band. NIRSpec IFU mode also shows a slight improvement in FOV but has twice the spatial resolution of KMOS

allowing native observations at the spatial sampling in this work without the need of super-sampling. This instrument would be of particular use in direct observations of BCGs within galaxy clusters, particularly those like the one located in XMM2215 to better resolve the kinematics of the individual components. It could also be used to target galaxies in the cores of galaxy clusters to better determine if the kinematics of the galaxies located in the core are representative of sub-cluster merging. Additionally to further investigate the properties of the forming BCG of XMM2215 the Atacama Large Millimetre/submillimetre Array (ALMA; Wootten & Thompson 2009) which would enable us to spatially resolve the cold gas present in the components of the BCG system and provide a more complete picture of the kinematics of these galaxies alongside the ionised gas component of Hα. However, *JWST*/NIRSpec in IFU mode will not be of ground breaking significance to cluster galaxy observations at the cosmic noon purely from the point of view of time to complete observation. As this IFU mode is not multiplexed it would take quite some time to complete observations equivalent to those in this work.

One of the main issues with work on cluster galaxies at the cosmic noon is the low volume of data. This was one of the main drivers behind KCS however, the number of galaxies used in this work is still very small compared to equivalent samples of field galaxies (see Stott et al. 2016). This is a great benefit of multiplexing spectroscopic instrumentation such as KMOS used for this work but the low availability of such instrumentation has impeded progress. As discussed in this work the situation is beginning to change with the increase in massively multiplexing spectroscopic facilities, although not all of these will be capable of probing the star-formation properties of galaxies at the cosmic noon which often requires NIR observations. When considering observations from multiplexing NIR IFUs there are few current options, although the proposed multi-mode spectroscopic instrument MOSAIC for the ELT would be a great improvement on spatial resolution in IFU mode and would make multiple simultaneous observations possible with its proposed multiplexing. Continued use of KMOS to expand the datasets using techniques outlined in this thesis would also be an excellent option to explore as this would provide clear like for like comparison within larger datasets. Greater use of the spatially resolved Hα emission to determine spatially resolved SFR across individual galaxies within the data could also prove interesting

in determining likely quenching scenarios. At the very least this could tell us if these galaxies are quenching from outside in or the opposite by finding an SFR gradient.

The current best options for proposed expansion of the dataset would be a massively multiplexed MOS, such as the upcoming Multi Object Optical and Near-infrared Spectrograph (MOONS) for the VLT and the current MOS mode for the *JWST*/NIRSpec instrument. While spatial data would be lost the large data volumes would really help to determine if some of the potential scenarios reached in this thesis are more statistically significant and if many galaxies in different clusters at the cosmic noon exhibit the same properties. The best use of MOONS and NIRSpec would be to target a range of star-forming and passive galaxy populations within galaxy clusters at the cosmic noon to provide more complete datasets for cluster to cluster comparison at this redshift range in an attempt to reduce the impact of cluster to cluster variation in the differences seen between cluster datasets.

Appendix A

Appendices

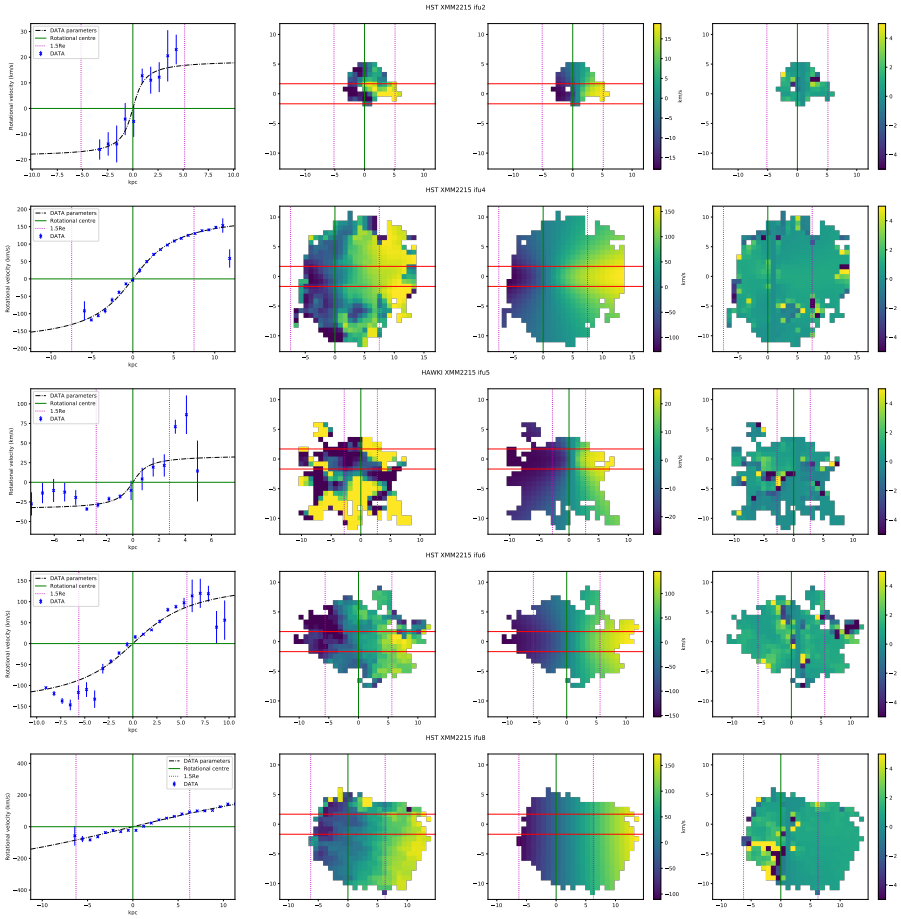

Figure A.1: From left to right the panels are: 1D rotation curve; 2D observed velocity map; model velocity map; and the model velocity map divided by the data for cluster XMM2215. The colour gradients for the observed map and model maps are the same scale and represent the rotational velocity. The red lines indicate the artificial slit used to extract the 1D rotational velocity curve.

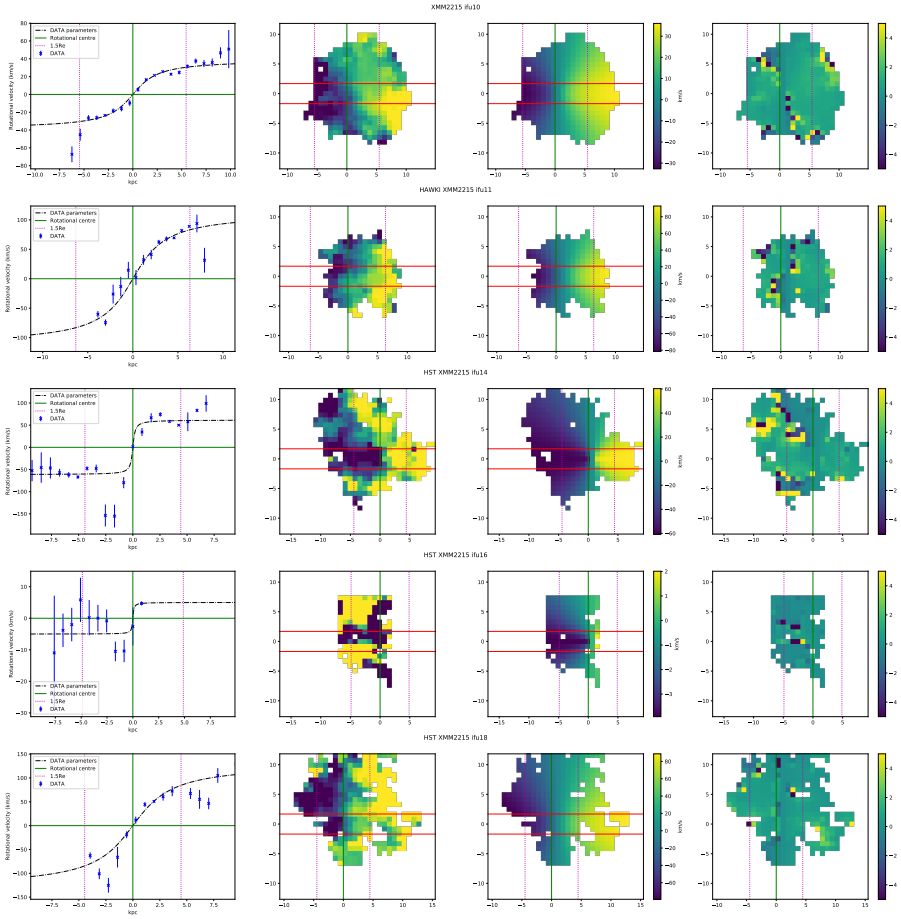

Figure A.2: From left to right the panels are: 1D rotation curve; 2D observed velocity map; model velocity map; and the model velocity map divided by the data for cluster XMM2215. The colour gradients for the observed map and model maps are the same scale and represent the rotational velocity. The red lines indicate the artificial slit used to extract the 1D rotational velocity curve.

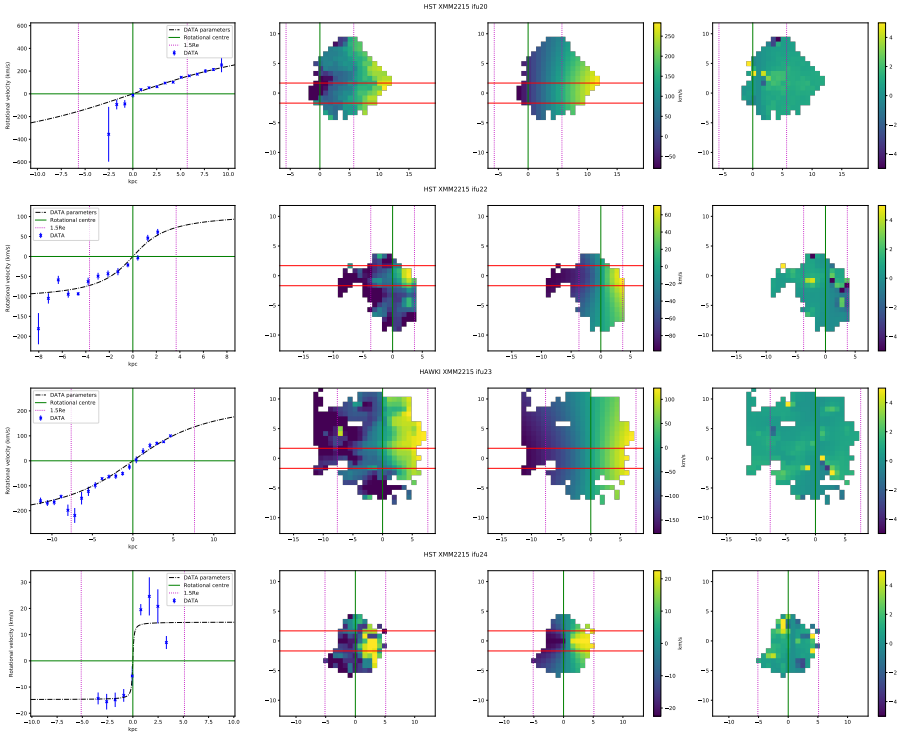

Figure A.3: From left to right the panels are: 1D rotation curve; 2D observed velocity map; model velocity map; and the model velocity map divided by the data for cluster XMM2215. The colour gradients for the observed map and model maps are the same scale and represent the rotational velocity. The red lines indicate the artificial slit used to extract the 1D rotational velocity curve.

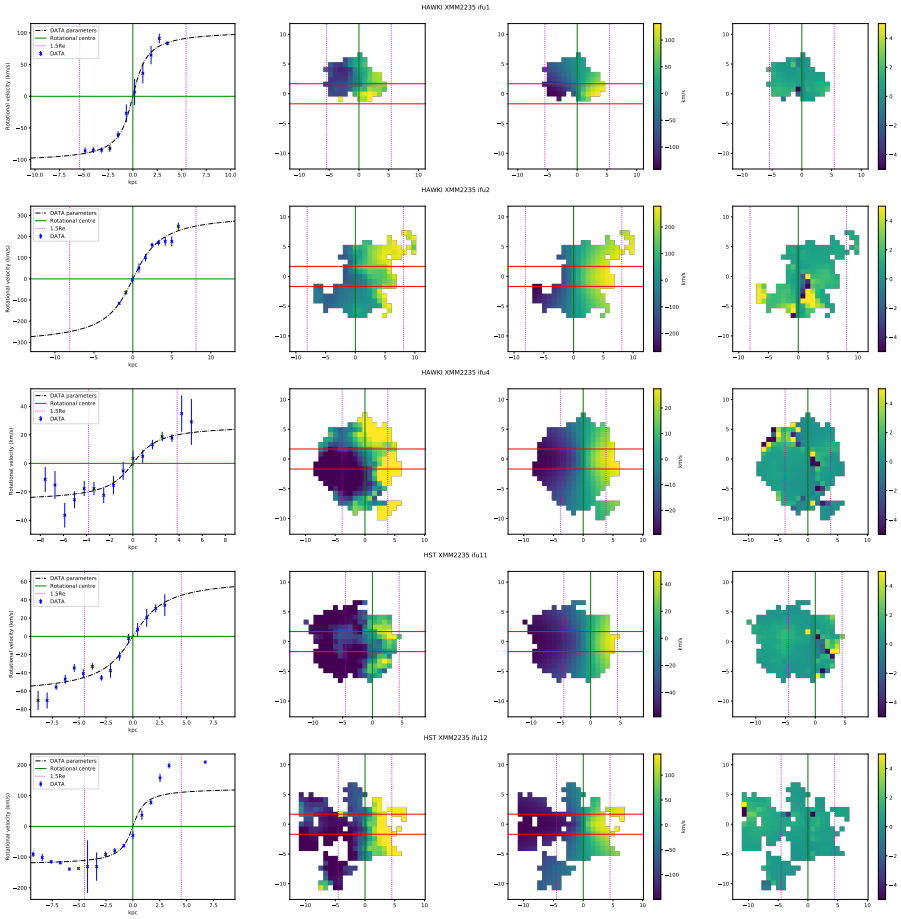

Figure A.4: From left to right the panels are: 1D rotation curve; 2D observed velocity map; model velocity map; and the model velocity map divided by the data for cluster XMM2235. The colour gradients for the observed map and model maps are the same scale and represent the rotational velocity. The red lines indicate the artificial slit used to extract the 1D rotational velocity curve.

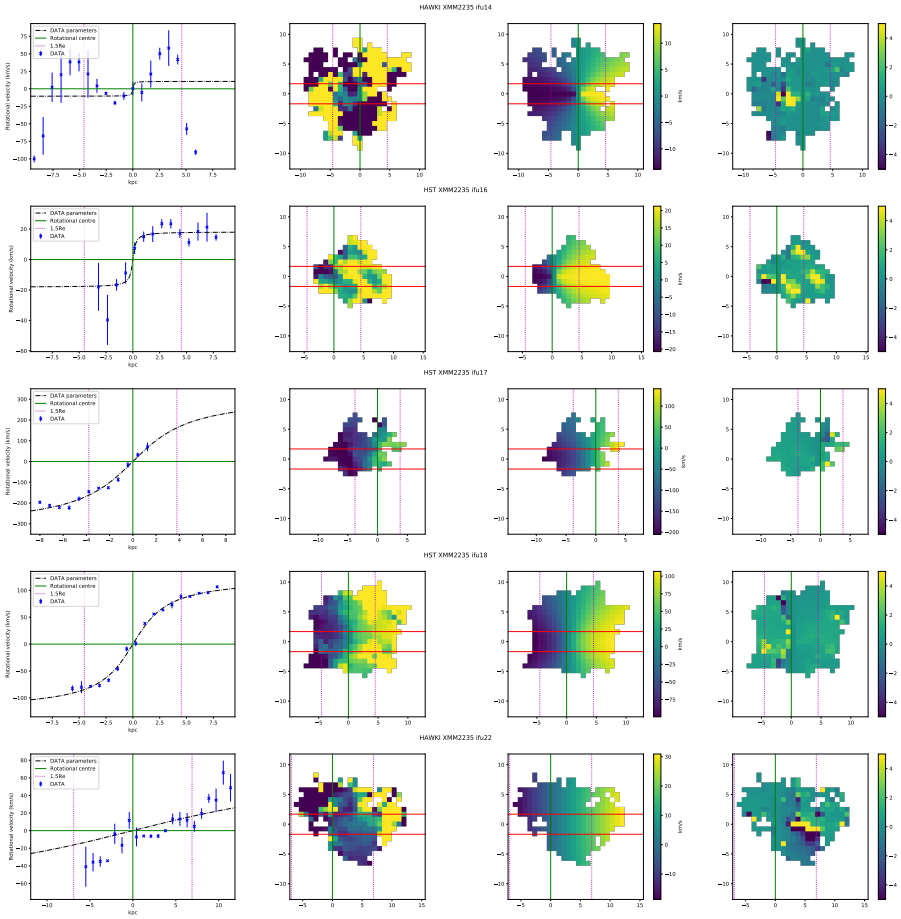

Figure A.5: From left to right the panels are: 1D rotation curve; 2D observed velocity map; model velocity map; and the model velocity map divided by the data for cluster XMM2235. The colour gradients for the observed map and model maps are the same scale and represent the rotational velocity. The red lines indicate the artificial slit used to extract the 1D rotational velocity curve.

References

Abell G. O., 1958, The Astrophysical Journal Supplement, 3, 211

Albert C. E., White R. A., Morgan W. W., 1977, The Astrophysical Journal, 211, 309

Alloin D., Collin-Souffrin S., Joly M., Vigroux L., 1979, Astronomy & Astrophysics, 78, 200

Armus L., Heckman T. M., Miley G. K., 1989, The Astrophysical Journal, 347, 727

Arnaboldi M., Ventimiglia G., Iodice E., Gerhard O., Coccato L., 2012, Astronomy & Astrophysics, 545, A37

Bahé Y. M. et al., 2017, Monthly Notices of the Royal Astronomical Society, 470, 4186

Baldwin J. A., Phillips M. M., Terlevich R., 1981, Publications of the Astronomical Society of the Pacific, 93, 5

Barbosa C. E., Arnaboldi M., Coccato L., Gerhard O., Mendes de Oliveira C., Hilker M., Richtler T., 2018, Astronomy & Astrophysics, 609, A78

Barbosa C. E., Arnaboldi M., Coccato L., Hilker M., Mendes de Oliveira C., Richtler T., 2016, Astronomy & Astrophysics, 589, A139

Barro G. et al., 2019, The Astrophysical Journal Supplement Series, 243, 22

Beifiori A. et al., 2017, The Astrophysical Journal, 846, 120

Bekki K., 1998, The Astrophysical Journal, 502, L133

Bell E. F. et al., 2004, The Astrophysical Journal, 600, L11

Bertin E., Arnouts S., 1996, Astronomy and Astrophysics Supplement Series, 117, 393

Bilton L. E., Hunt M., Pimbblet K. A., Roediger E., 2019, Monthly Notices of the Royal Astronomical Society, 490, 5017

Bleem L. E. et al., 2015, The Astrophysical Journal Supplement, 216, 27

Bloom J. V. et al., 2017, Monthly Notices of the Royal Astronomical Society, 465, 123

Böhringer H. et al., 2004, Astronomy & Astrophysics, 425, 367

Boquien M., Burgarella D., Roehlly Y., Buat V., Ciesla L., Corre D., Inoue A. K., Salas H., 2019, Astronomy & Astrophysics, 622, A103

Breuer J. P., Werner N., Mernier F., Mroczkowski T., Simionescu A., Clarke T. E., ZuHone J. A., Di Mascolo L., 2020, Monthly Notices of the Royal Astronomical Society, 495, 5014

Bryant J. J. et al., 2015, Monthly Notices of the Royal Astronomical Society, 447, 2857

Bundy K. et al., 2015, The Astrophysical Journal, 798, 7

Caglar T., Hudaverdi M., 2017, Monthly Notices of the Royal Astronomical Society, 472, 2633

Casado J., Ascasibar Y., Gavilan M., Terlevich R., Terlevich E., Hoyos C., Diaz A. I., 2015, Monthly Notices of the Royal Astronomical Society, 451, 888

Casey C. M. et al., 2013, Monthly Notices of the Royal Astronomical Society, 436, 1919

Cerulo P., Orellana G. A., Covone G., 2019, Monthly Notices of the Royal Astronomical Society, 487, 3759

Chabrier G., 2003, Publications of the Astronomical Society of the Pacific, 115, 763

Chan J. C. C. et al., 2018, The Astrophysical Journal, 856, 8

Chary R., Elbaz D., 2001, The Astrophysical Journal, 556, 562

Chester C., Roberts M. S., 1964, The Astronomical Journal, 69, 635

Cid Fernandes R., Stasińska G., Mateus A., Vale Asari N., 2011, Monthly Notices of the Royal Astronomical Society, 413, 1687

Coccato L., Gerhard O., Arnaboldi M., Ventimiglia G., 2011, Astronomy & Astrophysics, 533, A138

Cohen J. G., 1976, The Astrophysical Journal, 203, 587

Collins C. A. et al., 2009, Nature, 458, 603

Contini E., De Lucia G., Villalobos Á., Borgani S., 2014, Monthly Notices of the Royal Astronomical Society, 437, 3787

Cortese L. et al., 2019, Monthly Notices of the Royal Astronomical Society, 485, 2656

Courtes G., 1982, in Astrophysics and Space Science Library, Vol. 92, IAU Colloq. 67: Instrumentation for Astronomy with Large Optical Telescopes, Humphries C., ed., p. 123

Cowie A. S., 1996, Nature, 379, 678

Croom S. M. et al., 2012, Monthly Notices of the Royal Astronomical Society, 421, 872

Cullen F., Cirasuolo M., McLure R. J., Dunlop J. S., Bowler R. A. A., 2014, Monthly Notices of the Royal Astronomical Society, 440, 2300

Curti M., Mannucci F., Cresci G., Maiolino R., 2020, Monthly Notices of the Royal Astronomical Society, 491, 944

Dalcanton J. J., 2007, The Astrophysical Journal, 658, 941

Dale D. A., Helou G., 2002, The Astrophysical Journal, 576, 159

Dalton G. et al., 2012, in Society of Photo-Optical Instrumentation Engineers (SPIE) Conference Series, Vol. 8446, Ground-based and Airborne Instrumentation for Astronomy IV, McLean I. S., Ramsay S. K., Takami H., eds., p. 84460P

Dalton G. B. et al., 2006, in Society of Photo-Optical Instrumentation Engineers (SPIE) Conference Series, Vol. 6269, Society of Photo-Optical Instrumentation Engineers (SPIE) Conference Series, McLean I. S., Iye M., eds., p. 62690X

Davies R. I. et al., 2013, Astronomy & Astrophysics, 558, A56

Davis A. J., Khochfar S., Dalla Vecchia C., 2014, Monthly Notices of the Royal Astronomical Society, 443, 985

Davis M., Efstathiou G., Frenk C. S., White S. D. M., 1985, The Astrophysical Journal, 292, 371

de Jong R. S. et al., 2012, in Society of Photo-Optical Instrumentation Engineers (SPIE) Conference Series, Vol. 8446, Ground-based and Airborne Instrumentation for Astronomy IV, McLean I. S., Ramsay S. K., Takami H., eds., p. 84460T

De Lucia G., Blaizot J., 2007, Monthly Notices of the Royal Astronomical Society, 375, 2

De Propris R., Ali S., Bremer M. N., Phillipps S., 2019, Proceedings of the International Astronomical Union, 15, 264

De Propris R. et al., 2021, Monthly Notices of the Royal Astronomical Society, 500, 310

de Vaucouleurs G., 1961, The Astrophysical Journal Supplement, 5, 233

Delaye L. et al., 2014, Monthly Notices of the Royal Astronomical Society, 441, 203

Denicoló G., Terlevich R., Terlevich E., 2002, Monthly Notices of the Royal Astronomical Society, 330, 69

Dressler A., 1980, The Astrophysical Journal, 236, 351

Dressler A., 1984, Annual Review of Astronomy and Astrophysics, 22, 185

Dressler A., Smail I., Poggianti B. M., Butcher H., Couch W. J., Ellis R. S., Oemler, Jr. A., 1999, The Astrophysical Journal Supplement Series, 122, 51

Ebeling H., Edge A. C., Bohringer H., Allen S. W., Crawford C. S., Fabian A. C., Voges W., Huchra J. P., 1998, Monthly Notices of the Royal Astronomical Society, 301, 881

Ebeling H., Richard J., Smail I., Edge A. C., Koekemoer A. M., Zalesky L., 2021, Monthly Notices of the Royal Astronomical Society, 508, 3663

Einstein A., 1916, Annalen der Physik, 354, 769

Ellison S. L., Simard L., Cowan N. B., Baldry I. K., Patton D. R., McConnachie A. W., 2009, Monthly Notices of the Royal Astronomical Society, 396, 1257

Emerson J., McPherson A., Sutherland W., 2006, The Messenger, 126, 41

Epinat B., Amram P., Balkowski C., Marcelin M., 2010, Monthly Notices of the Royal Astronomical Society, 401, 2113

Erb D. K., Steidel C. C., Shapley A. E., Pettini M., Reddy N. A., Adelberger K. L., 2006, The Astrophysical Journal, 647, 128

Fabian A., 2012, Annual Review of Astronomy and Astrophysics, 50, 455

Förster Schreiber N. M. et al., 2009, The Astrophysical Journal, 706, 1364

Förster Schreiber N. M., Wuyts S., 2020, Annual Review of Astronomy and Astrophysics, 58, 661

Gao Y. et al., 2018, The Astrophysical Journal, 869, 15

Gavazzi G., Fumagalli M., Cucciati O., Boselli A., 2010, Astronomy & Astrophysics, 517, A73

Gladders M. D., Yee H. K. C., 2005, The Astrophysical Journal Supplement, 157, 1

Governato F. et al., 2010, Nature, 463, 203

Gregorini L., de Ruiter H. R., Parma P., Sadler E. M., Vettolani G., Ekers R. D., 1994, Astronomy and Astrophysics Supplement Series, 106, 1

Gregorini L., Vettolani G., de Ruiter H. R., Parma P., 1992, Astronomy and Astrophysics Supplement Series, 95, 1

Grützbauch R., Bauer A. E., Jørgensen I., Varela J., 2012, Monthly Notices of the Royal Astronomical Society, 423, 3652

Gunn J. E., Gott, J. Richard I., 1972, The Astrophysical Journal, 176, 1

Harrison C. M. et al., 2017, Monthly Notices of the Royal Astronomical Society, 467, 1965

Hayashi M., Kodama T., Koyama Y., Tanaka I., Shimasaku K., Okamura S., 2010, Monthly Notices of the Royal Astronomical Society, 402, 1980

Henden N. A., Puchwein E., Sijacki D., 2020, Monthly Notices of the Royal Astronomical Society, 498, 2114

Hertzsprung E., 1908, Astronomische Nachrichten, 179, 373

Hertzsprung E., 1913, Astronomische Nachrichten, 196, 201

Hilton M. et al., 2010, The Astrophysical Journal, 718, 133

Holland W. S. et al., 1999, Monthly Notices of the Royal Astronomical Society, 303, 659

Hubble E. P., 1929, The Astrophysical Journal, 69, 103

Humphries C. M., Purkins T. E., 1980, Endeavour, 4, 132

Icke V., 1985, Astronomy & Astrophysics, 144, 115

Jakobsen P. et al., 2022, Astronomy & Astrophysics, 661, A80

Jansen F. et al., 2001, Astronomy & Astrophysics, 365, L1

Jin S. et al., 2023, Monthly Notices of the Royal Astronomical Society

Johnston E. J., Merrifield M., Aragón-Salamanca A., 2018, Monthly Notices of the Royal Astronomical Society, 478, 4255

Jones C., Forman W., 1984, The Astrophysical Journal, 276, 38

Joo H., Jee M. J., 2023, Nature, 613, 37

Kacprzak G. G. et al., 2015, The Astrophysical Journal, 802, L26

Kauffmann G., Haehnelt M., 2000, Monthly Notices of the Royal Astronomical Society, 311, 576

Kennicutt, R. C. J., 1983, The Astrophysical Journal, 272, 54

Kennicutt R. C., 1998, Annual Review of Astronomy and Astrophysics, 36, 189

Kepler J., Galilei G., Pena J., 1611, Ioannis Kepleri ... Dioptrice seu Demonstratio eorum quae visui : praemissae epistolae Galilaei de iis, quae post editionem nuncii & visibilibus propter conspicilla non ita pridem inventa accidunt siderii ope perspicilli, nova & admiranda in coelo deprehensa sunt; item examen praefationis Ioannis Penae ... in optica Euclidis, de usu optices in philosophia

Kewley L. J., Dopita M. A., 2002, The Astrophysical Journal Supplement Series, 142, 35

Kewley L. J., Ellison S. L., 2008, The Astrophysical Journal, 681, 1183

Kluge M. et al., 2020, The Astrophysical Journal Supplement, 247, 43

Koester B. P. et al., 2007, The Astrophysical Journal, 660, 221

Kroupa P., 2001, Monthly Notices of the Royal Astronomical Society, 322, 231

Kubo M. et al., 2021, The Astrophysical Journal, 919, 6

Kulas K. R. et al., 2013, The Astrophysical Journal, 774, 130

Lani C. et al., 2013, Monthly Notices of the Royal Astronomical Society, 435, 207

Laporte C. F. P., White S. D. M., Naab T., Gao L., 2013, Monthly Notices of the Royal Astronomical Society, 435, 901

Larson R. B., Tinsley B. M., Caldwell C. N., 1980, The Astrophysical Journal, 237, 692

Lauer T. R., Postman M., Strauss M. A., Graves G. J., Chisari N. E., 2014, The Astrophysical Journal, 797, 82

Leavitt H. S., 1908, Project PHAEDRA: Preserving Harvard's Early Data and Research in Astronomy (https://library.cfa.harvard.edu/project-phaedra). Harvard College Observatory observations, 27, 952

Lerchster M. et al., 2011, Monthly Notices of the Royal Astronomical Society, 411, 2667

Lesser M., 2015, Publications of the Astronomical Society of the Pacific, 127, 1097

Lidman C. et al., 2008, Astronomy & Astrophysics, 489, 981

Lidman C. et al., 2012, Monthly Notices of the Royal Astronomical Society, 427, 550

Lilly S. J., Carollo C. M., Pipino A., Renzini A., Peng Y., 2013, The Astrophysical Journal, 772, 119

Liu F. S. et al., 2013, The Astrophysical Journal, 769, 147

Liu F. S., Xia X. Y., Mao S., Wu H., Deng Z. G., 2008, Monthly Notices of the Royal Astronomical Society, 385, 23

Ma C.-J. et al., 2015, The Astrophysical Journal, 806, 257

Madau P., Dickinson M., 2014, Annual Review of Astronomy and Astrophysics, 52, 415

Magrini L., Sommariva V., Cresci G., Sani E., Galametz A., Mannucci F., Petropoulou V., Fumana M., 2012, Monthly Notices of the Royal Astronomical Society, 426, 1195

Maier C., Hayashi M., Ziegler B. L., Kodama T., 2019, Astronomy & Astrophysics, 626, A14

Maiolino R. et al., 2008, Astronomy & Astrophysics, 488, 463

Mannucci F., Cresci G., Maiolino R., Marconi A., Gnerucci A., 2010, Monthly Notices of the Royal Astronomical Society, 408, 2115

Markevitch M., Gonzalez A. H., David L., Vikhlinin A., Murray S., Forman W., Jones C., Tucker W., 2002, The Astrophysical Journal, 567, L27

Martig M., Bournaud F., Teyssier R., Dekel A., 2009, The Astrophysical Journal, 707, 250

Martin D. C. et al., 2005, The Astrophysical Journal, 619, L1

Martini P., 2001, The Astronomical Journal, 121, 598

Mashchenko S., Wadsley J., Couchman H. M. P., 2008, Science, 319, 174

Matthews T. A., Morgan W. W., Schmidt M., 1964, The Astrophysical Journal, 140, 35

Medling A. M. et al., 2018, Monthly Notices of the Royal Astronomical Society, 475, 5194

Mehrtens N. et al., 2012, Monthly Notices of the Royal Astronomical Society, 423, 1024

Merritt D., 1984, The Astrophysical Journal, 276, 26

Messier C., 1781, Catalogue des Nébuleuses et des Amas d'Étoiles (Catalog of Nebulae and Star Clusters). Connoissance des Temps ou des Mouvements Célestes, for 1784, p. 227-267

Montenegro-Taborda D., Rodriguez-Gomez V., Pillepich A., Avila-Reese V., Sales L. V., Rodríguez-Puebla A., Hernquist L., 2023, 000

Moore B., Katz N., Lake G., Dressler A., Oemler A., 1996, Nature, 379, 613

Moore B., Lake G., Katz N., 1998, The Astrophysical Journal, 495, 139

Nascimento R. S., Ribeiro A. L. B., Trevisan M., Carrasco E. R., Plana H., Dupke R., 2016, Monthly Notices of the Royal Astronomical Society, 460, 2193

Newman A. B., Treu T., Ellis R. S., Sand D. J., 2013, The Astrophysical Journal, 765, 25

Newville M., Stensitzki T., Allen D. B., Ingargiola A., 2014, LMFIT: Non-Linear Least-Square Minimization and Curve-Fitting for Python

Noble A. G., Webb T. M. A., Muzzin A., Wilson G., Yee H. K. C., van der Burg R. F. J., 2013, The Astrophysical Journal, 768, 118

Oemler A. J., 1976, The Astrophysical Journal, 209, 693

Oliva E. et al., 2015, Astronomy & Astrophysics, 581, A47

Orellana-González G., Cerulo P., Covone G., Cheng C., Leiton R., Demarco R., Gendron-Marsolais M. L., 2022, Monthly Notices of the Royal Astronomical Society, 512, 2758

Osterbrock D. E., Shuder J. M., 1982, The Astrophysical Journal Supplement Series, 49, 149

Ostriker J. P., Tremaine S. D., 1975, The Astrophysical Journal, 202, L113

Patrick Henry J. et al., 2010, The Astrophysical Journal, 725, 615

Patton D. R., Carlberg R. G., Marzke R. O., Pritchet C. J., da Costa L. N., Pellegrini P. S., 2000, The Astrophysical Journal, 536, 153

Peng C. Y., Ho L. C., Impey C. D., Rix H.-W., 2010a, The Astronomical Journal, 139, 2097

Peng Y.-j. et al., 2010b, The Astrophysical Journal, 721, 193

Pettini M., Pagel B. E. J., 2004, Monthly Notices of the Royal Astronomical Society, 348, L59

Pimbblet K. A., 2008, Publications of the Astronomical Society of Australia, 25, 176–183

Pimbblet K. A., Roseboom I. G., Doyle M. T., 2006, Monthly Notices of the Royal Astronomical Society, 368, 651

Poggianti B. M. et al., 2019, The Astrophysical Journal, 887, 155

Price-Whelan A. M. et al., 2018, The Astronomical Journal, 156, 123

Prichard L. J. et al., 2017, The Astrophysical Journal, 850, 203

Querejeta M. et al., 2015, Astronomy & Astrophysics, 579, L2

Quilis V., Moore B., Bower R., 2000, Science, 288, 1617

Quintana H., Ramirez A., Way M. J., 1996, The Astronomical Journal, 112, 36

Rich J. A., Kewley L. J., Dopita M. A., 2011, The Astrophysical Journal, 734, 87

Ristea A. et al., 2022, Monthly Notices of the Royal Astronomical Society, 517, 2677

Robitaille T. P. et al., 2013, Astronomy & Astrophysics, 558, A33

Rosati P., Della Ceca R., Norman C., Giacconi R., 1998, The Astrophysical Journal, 492, L21

Rousselot P., Lidman C., Cuby J. G., Moreels G., Monnet G., 2000, Astronomy & Astrophysics, 354, 1134

Rudick C. S., Mihos J. C., McBride C. K., 2011, The Astrophysical Journal, 732, 48

Rykoff E. S. et al., 2014, The Astrophysical Journal, 785, 104

Salpeter E. E., 1955, The Astrophysical Journal, 121, 161

Sarazin C. L., 1986, Reviews of Modern Physics, 58, 1

Sarkar A. et al., 2023, The Astrophysical Journal, 944, 132

Schaefer A. L. et al., 2017, Monthly Notices of the Royal Astronomical Society, 464, 121

Schawinski K. et al., 2014, Monthly Notices of the Royal Astronomical Society, 440, 889

Schneider P., 1996, Monthly Notices of the Royal Astronomical Society, 283, 837

Schombert J., 1986, The Astrophysical Journal Supplement, 60, 603

Sharples R. et al., 2013, The Messenger, 151, 21

Shen S., Mo H. J., White S. D. M., Blanton M. R., Kauffmann G., Voges W., Brinkmann J., Csabai I., 2003, Monthly Notices of the Royal Astronomical Society, 343, 978

Shimakawa R., Kodama T., Tadaki K.-i., Hayashi M., Koyama Y., Tanaka I., 2015, Monthly Notices of the Royal Astronomical Society, 448, 666

Silk J., 1976, The Astrophysical Journal, 208, 646

Smith B. A., 1976, in Charge-Coupled Device Technology and Applications, pp. 135–138

Sobral D., Best P. N., Matsuda Y., Smail I., Geach J. E., Cirasuolo M., 2012, Monthly Notices of the Royal Astronomical Society, 420, 1926

Speagle J. S., Steinhardt C. L., Capak P. L., Silverman J. D., 2014, The Astrophysical Journal Supplement Series, 214, 15

Springel V. et al., 2005, Nature, 435, 629

Stanford S. A. et al., 2006, The Astrophysical Journal, 646, L13

Stasińska G., Cid Fernandes R., Mateus A., Sodré L., Asari N. V., 2006, Monthly Notices of the Royal Astronomical Society, 371, 972

Stephenson H. M. O. et al., 2024, Monthly Notices of the Royal Astronomical Society, 527, 7891

Stott J. P. et al., 2020, Monthly Notices of the Royal Astronomical Society, 497, 3083

Stott J. P., Collins C. A., Burke C., Hamilton-Morris V., Smith G. P., 2011, Monthly Notices of the Royal Astronomical Society, 414, 445

Stott J. P. et al., 2010, The Astrophysical Journal, 718, 23

Stott J. P. et al., 2016, Monthly Notices of the Royal Astronomical Society, 457, 1888

Strazzullo V. et al., 2013, The Astrophysical Journal, 772, 118

Strazzullo V. et al., 2010, Astronomy & Astrophysics, 524, A17

Sunyaev R., Zeldovich Y. B., 1972, Astronomy & Astrophysics, 20, 189

Swinbank A. M. et al., 2013, Monthly Notices of the Royal Astronomical Society, 438, 1267

Swinbank A. M., Smail I., Sobral D., Theuns T., Best P. N., Geach J. E., 2012, The Astrophysical Journal, 760, 130

Thatte N. et al., 2010, in Society of Photo-Optical Instrumentation Engineers (SPIE) Conference Series, Vol. 7735, Ground-based and Airborne Instrumentation for Astronomy III, McLean I. S., Ramsay S. K., Takami H., eds., p. 77352I

Tiley A. L. et al., 2021, Monthly Notices of the Royal Astronomical Society, 506, 323

Tiley A. L. et al., 2020, Monthly Notices of the Royal Astronomical Society, 496, 649

Tran K.-V. H. et al., 2015, The Astrophysical Journal, 811, 28

Tran K.-V. H. et al., 2010, The Astrophysical Journal, 719, L126

Tully R. B., Fisher J. R., 1977, Astronomy & Astrophysics, 500, 105

Valentino F. et al., 2015, The Astrophysical Journal, 801, 132

van der Wel A. et al., 2014, The Astrophysical Journal, 788, 28

van Dokkum P. G., Stanford S. A., Holden B. P., Eisenhardt P. R., Dickinson M., Elston R., 2001, The Astrophysical Journal, 552, L101

van Weeren R. J., de Gasperin F., Akamatsu H., Brüggen M., Feretti L., Kang H., Stroe A., Zandanel F., 2019, Space Science Reviews, 215, 16

Vaughan S. P. et al., 2020, Monthly Notices of the Royal Astronomical Society, 496, 3841

Visvanathan N., Sandage A., 1977, The Astrophysical Journal, 216, 214

Wang X. et al., 2022, The Astrophysical Journal, 926, 70

Webb T. M. A. et al., 2015, The Astrophysical Journal, 814, 96

Wegner M., Muschielok B., 2008, p. 70190T

Weisskopf M. C., Tananbaum H. D., Van Speybroeck L. P., O'Dell S. L., 2000, in Society of Photo-Optical Instrumentation Engineers (SPIE) Conference Series, Vol. 4012, X-Ray Optics, Instruments, and Missions III, Truemper J. E., Aschenbach B., eds., pp. 2–16

Wisnioski E. et al., 2015, The Astrophysical Journal, 799, 209

Wootten A., Thompson A. R., 2009, IEEE Proceedings, 97, 1463

Yabe K. et al., 2012, Publications of the Astronomical Society of Japan, 64, 60

York D. G. et al., 2000, The Astronomical Journal, 120, 1579

Zhang Y. et al., 2016, The Astrophysical Journal, 816, 98

Zhou Y., Chen Y., Shi Y., Gu Q., Wang J., Bizyaev D., 2023, arXiv e-prints, arXiv:2303.00384

Zwicky F., 1937, The Astrophysical Journal, 86, 217

Zwicky F., 1951, Publications of the Astronomical Society of the Pacific, 63, 61

Zwicky F., Humason M. L., 1961, The Astrophysical Journal, 133, 794